Universidade de Lisboa
Faculdade de Ciências
Departamento de Física

Studying AGN galaxy hosts in the framework of Gaia mission

Ana Sofia Paulino Afonso

Dissertação
Mestrado em Física
Astrofísica e Cosmologia

2014

Universidade de Lisboa
Faculdade de Ciências
Departamento de Física

Studying AGN galaxy hosts in the framework of Gaia mission

Ana Sofia Paulino Afonso

Dissertação
Mestrado em Física
Astrofísica e Cosmologia

Orientadores: Professor Doutor António Joaquim Rosa Amorim Barbosa
Doutora Sonia Antón Castillo

2014

Tudo o que faço ou medito
Fica sempre na metade.
Querendo, quero o infinito.
Fazendo, nada é verdade.

Que nojo de mim me fica
Ao olhar para o que faço!
Minha alma é lúcida e rica,
E eu sou uma mar de sargaço-

Um mar onde bóiam lentos
Fragmentos de um mar de além...
Vontades ou pensamentos?
Não o sei e sei-o bem.

- Fernando Pessoa, in "Cancioneiro"

This page intentionally contains only this sentence.

To my cats, Ebony and Fermi, and my dog, Nika, the best (closet) researchers I have ever met in my life.

To everyone who shares with me this 'lost' planet in the vastness of space-time, especially my parents, Isabel and Fernando, and my boyfriend, Bruno.

This page intentionally contains only this sentence.

RESUMO

A missão astrométrica Gaia da Agência Espacial Europeia (ESA) (Perryman et al., 2001; Mignard, 2010) foi lançada a 19 de dezembro de 2013 e colocada em órbita em torno do Sol num ponto designado por L2 que se situa a 1.5 milhões de quilómetros da Terra. Com o intuito de construir o mais detalhado mapa tridimensional da nossa galáxia, e no seguimento da primeira missão de mapeamento de estrelas lançado pela ESA - Hipparcos (1989), o Gaia irá medir com extrema precisão a posição, a distância, a velocidade, o espectro e o brilho de mil milhões de estrelas da nossa galáxia.

No âmbito da definição de um conjunto de fontes de referência que serão utilizadas para fazer a conexão entre o presente sistema de referência celeste, o ICRF (*International Celestial Reference Frame*), e o futuro GCRF (*Gaia Celestial Reference Frame*), é fundamental estudar os objetos que serão potencialmente utilizados para o efeito e verificar se são viáveis como referências astrométricas. Para tal, é necessário verificar se possuem centros de luz bem definidos e estáveis que não são afetados nem por variações temporais nem pela potencial deteção de emissão proveniente da galáxia hospedeira do objeto.

Num tópico também relacionado com esta missão, proponho-me a caracterizar um conjunto de galáxias elípticas e passivas (*Optically Passive Elliptical Radio Galaxies* - OPERGs) que possuem núcleos ativos (*Active Galactic Nuclei* - AGN) na sua região central sendo fortes emissores no rádio. Estas galáxias não têm emissão extra no ótico que se sobreponha de forma evidente à emissão estelar e, portanto, constituem uma excelente amostra de objetos para o estudo das galáxias hospedeiras de AGNs.

Tirando partido do enorme potencial das já existentes imagens astronómicas na banda do ótico, nomeadamente aquelas inseridas no projeto SDSS-DR9 (*Sloan Digital Sky Survey: Data Release 9*, York et al. 2000; Ahn et al. 2012), eu usei o *software* público GALFIT (Peng et al., 2002, 2010) para quantificar a informação sobre a estrutura dos objetos por comparação com modelos analíticos descritos na literatura relacionada com a astronomia extra-galáctica e que são amplamente usados como é o caso do perfil de Sérsic (1968).

Para estudar o problema relacionado com a definição do futuro GCRF, foquei-me numa amostra que deriva da segunda realização do ICRF (ICRF2 - Fey et al. 2004, 2009) em conjunto com uma lista de objetos que permitirão a extensão deste sistema de referência, propostos por Bourda et al. (2011). De um total de 400 fontes originais (295 provenientes do ICRF2 e 105 do catálogo de Bourda et al. 2011) existem 198 com imagens disponíveis na base de dados do SDSS-DR9. Dessas 198, 16 são excluídas da amostra final em estudo por serem ou demasiado fracas ou por

serem tão brilhantes que saturaram o CCD não permitindo uma análise correta da sua estrutura. Das restantes 182 fontes, 134 não apresentam indícios de possuírem qualquer galáxia hospedeira detetável no limite do SDSS e 16 possuem uma deteção confirmada de emissão extensa em torno do *Quasi-Stellar Object* (QSO). Os outros 32 objetos indicam uma possível deteção da galáxia hospedeira, no entanto a informação atual não permite caracterizar com fiabilidade a estrutura dessa emissão extensa. No que toca ao nível de resíduos encontrados após subtração do melhor modelo, verifico que todos estes objetos têm menos de 15% de luz residual. Duas das fontes estão localizadas na Stripe 82, i.e. numa faixa do céu que foi esmiuçada pelo menos 10 vezes pelo SDSS permitindo uma maior combinação de profundidade e resolução (Annis et al., 2011), levando-me a proceder à comparação dos resultados utilizando estes dados com os obtidos através do SDSS-DR9. Não foram encontradas diferenças quanto ao tipo de perfil a ajustar. Uma tentativa de usar os dados do *Hubble Space Telescope* (HST) em 25 dos 400 objetos originais não deu resultados científicos fiáveis devido à impossibilidade de construção de uma *Point Spread Function* (PSF) capaz de ajustar de forma aceitável a emissão pontual desses objetos.

Relativamente ao estudo morfológico das OPERGs, todas elas possuem imagens disponíveis no SDSS e dividem-se, quanto à sua estrutura morfológica, nas seguintes classes: 15 galáxias ajustadas com um único perfil de Sérsic; 10 galáxias ajustadas com uma combinação de dois perfis de Sérsic; 2 galáxias ajustadas com uma combinação de um perfil de Sérsic com um perfil central do tipo gaussiano; e um galáxia ajustada unicamente com uma emissão pontual (PSF). Tomando em consideração a luz residual obtida após a subtração do melhor modelo à imagem original, foram identificados aspetos que podem perturbar a determinação do centroide (tais como faixas de poeira, jatos, assimetrias e perturbações causadas por interações entre galáxias). No final, 16 das 28 galáxias observadas possuem um nível baixo de perturbações permitindo assim um maior grau de precisão na medição das coordenadas centrais da emissão. Tais medições de coordenadas foram efetuadas no âmbito de um projeto paralelo que pretende encontrar objetos com centroides no ótico e no rádio desfasados. Nesse sentido, apresento os valores dos baricentros de luz dos modelos obtidos para todos os objetos da amostra para que possam ser comparados com futuros trabalhos levados a cabo na região espetral do rádio. Neste caso, também se procedeu à análise de dados obtidos com o HST, para os quais tive acesso a 4 das 28 galáxias estudadas. Em 3 dos 4 casos, as galáxias apresentavam características morfológicas (como discos de poeira e jatos de matéria) que impediam um bom ajuste dos seus perfis de brilho e, portanto, nenhuma análise quantitativa foi efetuada. A quarta fonte foi analisada em 2 filtros distintos, F555W e F814W, sendo o seu perfil consistente com o derivado do SDSS. Quanto ao seu baricentro de luz, este é consistente entre os dois casos, dentro dos limites de resolução das imagens.

A partir da informação morfológica obtida com os dados do SDSS, eu usei o GIBIS (*Gaia Instrument and Basic Simulator*) com a finalidade de simular a maneira como estes objetos serão observados com os telescópios do Gaia. Nesse sentido, desenvolvi uma simulação em condições ideais para testar a recuperação de parâmetros estruturais das galáxias a partir de dados simulados do Gaia. Os resultados, baseados numa amostra de 500 galáxias com um disco extenso mais um bojo central, mostram que será possível obter os parâmetros relacionados com o bojo e o disco com elevado grau de precisão, em particular os relacionados com o bojo. Testei também o uso de diferentes combinações de colunas do CCD do Gaia para obter informações sobre os objetos e concluo que usar uma combinação entre AF2 e SM1 trará melhores resultados na caracterização geral da galáxia em termos de tamanho do disco. Para o caso do raio do bojo, parece ser mais indicado usar unicamente os dados obtidos com a coluna AF2. Já para o caso das intensidades das duas componentes, usar simplesmente a coluna SM1 é o que melhor ajusta estes parâmetros. No entanto, as médias obtidas podem estar influenciadas pelo não avultado número de galáxias simuladas. Para uma subamostra de 9 galáxias (5 bojo+disco e 4 puras elípticas), usei o meu código para recuperar os parâmetros estruturais com base em simulações efetuadas com o GIBIS.

Os resultados indicam que é possível recuperar os parâmetros das duas componentes em apenas alguns casos. Acontece que para valores de intensidades parece existir uma subestimação do valor real enquanto que para os raios a tendência é para sobrestimar. Quanto ao rácio entre eixos este não é bem recuperado sendo subestimado para praticamente todas as componentes. O motivo pelo qual estes resultados aparecem não é clarificado no âmbito desta tese embora possa estar ligado ao tamanho destas galáxias que são maiores em tamanho que as janelas do Gaia.

Palavras-chave: Gaia/ESA - Astrometria - Galáxias - Morfologia - Simulações

This page intentionally contains only this sentence.

ABSTRACT

Gaia, a mission from ESA and launched last December, aims to produce the best 3D map of the Galaxy. It is a five year, all-sky astrometric mission that will observe billions of objects, mostly of them galactic sources. But a fraction of the detected objects will be galaxies, among them, those that harbour an active nucleus in their centre (AGN).

The AGNs will be paramount for the alignment between the actual *International Celestial Reference Frame* (ICRF) and the future *Gaia Celestial Reference Frame* (GCRF), in particular those objects that define the ICRF, i.e. some of the strongest radio emitting AGNs. The ICRF defining sources have the most accurate and stable radio coordinates. The same coordinates stability and accuracy is needed at the optical regime, in order to ensure the best alignment between the two reference frames. Gaia will be able to obtain an astrometry accuracy at the microarcsecond level, so the challenge is to understand if there is any putative source of uncertainty of the optical centroid inherent to the objects. Indeed, considering the Gaia characteristics it is very likely that in a fraction of the AGNs, the host galaxy (extended component) might be detected, which might perturb the photometric centre determination.

The aim of this dissertation is to investigate the optical counterparts of the ICRF objects in order to check their astrometric suitability, and on the other hand to assert the Gaia detectability of a sample of passive elliptical galaxies by taking advantage of the SDSS images, the galaxy/point source fitting algorithm GALFIT and the GIBIS.

I conclude that the majority ($\sim$74%) of the analysed ICRF2+ sources are indeed point-like and $\sim$9% has a confirmed host detection. It will be possible to detect and quantify the bulge structure of elliptical galaxies as seen by Gaia data.

Keywords: Gaia/ESA - Astrometry - Galaxies - Morphology - Simulations

This page intentionally contains only this sentence.

CONTENTS

LIST OF FIGURES

LIST OF TABLES

This page intentionally contains only this sentence.

PREFACE

From our home on the Earth, we look out into the distances are strive to imagine the sort of world into which we are born. (...) But with increasing distance our knowledge fades, and fades rapidly, until at the last dim horizon we search among ghostly errors of observations for landmarks that are scarcely more substantial. The search will continue. The urge is older than history. It is not satisfied and it will not be suppressed.

- Edwin Hubble, The Law of Red Shifts, 1953

The emergence of the study of celestial bodies outside of our own galaxy can be pinpointed to the middle of the 18^{th}. On that epoch, Thomas Wright, hypothesized about the possibility of some of the nebulae that were observed in the skies might be actually outside of our own Milky Way. Some years past that time, Immanuel Kant came up with the "*island universes*" terminology to refer to these possibly distant objects. Almost a century later, François Arago revived the hypothesis of nebulae outside our own (Arago, 1854) thus creating momentum for the idea to take roots in the scientific community. However, some of those nebulae, first compiled by Messier (1784) with a complete different purpose, were actually part of the Milky Way (such as planetary nebulae or globular clusters). A compilation of new observations had to be made to spread some light on this controversial topic. William Herschel and Lord Rosse both contributed greatly by observing several thousand sources and by being able to distinguish point sources within the extended nebulae giving support to the idea of the existence of distant extragalactic sources. Slipher (1913) observed the spectra of some of those nebulae and found that some of them had their lines deviated from their laboratory position towards redder wavelengths leading to the measurement of their recessive motion relative to the Milky Way at a greater speed than that needed to escape from our galaxy.

This problem was finally solved in the 1920s. In the beginning of that decade, Curtis (1920) presented several evidences on why the Andromeda "*nebula*" M31 is a galaxy itself, like ours. Öpik (1922) estimated its distance from us that puts it at 450 kilo-parsec away. Still around two times smaller than its current measurements, but far enough to be exterior to the Milky Way. Taking advantage of the large aperture of the Mount Wilson Telescope, Edwin Hubble observed a number of Cepheid stars (whose characteristic variable brightness allows one to compute their absolute magnitude) and, using the distance modulus, confirmed the large distance of these objects while still underestimating their actual value by a factor of $\sim$3 due to calibration offsets. Based on the images of the galaxies he also devised a scheme for classifying them according to their overall shape - the Hubble (1926) sequence - and stated that the Universe is currently expanding (Hubble, 1929), the foundations of modern cosmology.

As more and more images and spectra were obtained, new mysteries started to puzzle astronomers. Seyfert (1943) uncovered the presence of strong emission lines superimposed on a regular-like spectrum arising from the centre of a sample of six galaxies. Some were narrow, and some were broader but both were strong enough to compel a search for this newly found evidences. Woltjer (1959) denoted that the required central mass (< 100 pc) to support such an intense light emission should be of about 10^8 $M_\odot$. Thus, the first idea proposed by Hoyle & Fowler (1963) was that a very massive star-like object resided in the centre of those galaxies which would produce the emission lines from the accretion of surrounding gas through a rotating disc. A year later, the hypothesis of the core of the active galactic nuclei (AGN) was actually a black hole and not a super massive star came to existence (Salpeter, 1964; Zel'dovich & Novikov, 1964).

This notion of a super massive central black hole which led to an active galactic nuclei and is also present in the centre of our own galaxy (Lynden-Bell & Rees, 1971) was a strong theory that explained several facets of the observed facts. It explains the existence of large amounts of energy emitted through the accretion of matter, the subsequent release of gravitational energy and also the limited size of the regions responsible for that emission with its subjacent short time scales of variability detected in AGNs. A new field arose to study all the related physical phenomena that are responsible for the observed emission in a very broad range of the electromagnetic spectrum and all the processes involved in the formation, evolution and distribution of this kind of objects in the Universe.

After years of dedicated research, we are now closer to understanding these fascinating objects with impressive energy liberation from the central super massive black holes which are intriguing objects on their own. Apart from their core body, the accretion disc, the warm dust torus and all the surrounding gas take part in the global picture of what an AGN is. These, in turn, affect the formation and subsequent evolution of the galaxies that we observe leaving their imprint in the structure of the Universe at large scales. But, as it is always the case in science, we are still far from fully understanding this particular "*specimens*" of our Universe and more hours of observations and years of research are required to acquire a little bit more of comprehension of what is around us.

In this dissertation, several AGN will be studied in detail with the aim of understanding their morphology and its impact in future studies with the forthcoming Gaia mission. The prime interest lies in quantifying the structure of the underlying host galaxies that harbour AGN in their centre. The main observational tool for this research is the photometry obtained in the optical domain by the *Sloan Digital Sky Survey* Data Release 9 and, when possible, the archive of the *Hubble Space Telescope*.

CHAPTER 1

INTRODUCTION

"Some people believe that without history, our lives amount to nothing. At some point, we all have to choose. Do we fall back on what we know? Or, do we step forward, to something new? It is hard not to be haunted by our past. Our history is what shapes us, what guides us. Our history resurfaces. Time, after time, after time. So we have to remember. Sometimes, the most important history, is the history we are making today."

- Time After Time; Grey's Anatomy

Contents

This dissertation investigates a sample of extragalactic objects in the optical band, in the framework of the Gaia (ESA) mission. The specific samples under analysis in the context of this project are:

- a set of the *International Celestial Reference Frame* (ICRF) sources that will enable the connection between the ICRF and the *Gaia Celestial Reference Frame*, GCRF. These are mainly blazars that show a very compact optical morphology, mostly being emission related with the powerful AGN. The sample comprises the ICRF2 defining sources together with a proposed extension by Bourda et al. (2010);
- a set of optically passive AGNs living in elliptical galaxies that show little or no extra activity in the optical regime, i.e. a kind of counterpart of the previous set of objects.

The global aim of this dissertation is to model the 2-dimensional surface brightness profiles of the objects using the most common software for this kind of analysis - GALFIT (Peng et al., 2002, 2010) - in order to characterize any detectable host galaxy for the case of the compact objects and to assess the Gaia detectability of the AGN galaxy hosts through the *Gaia Instrument and Basic Image Simulator* (GIBIS, Babusiaux 2005; Babusiaux et al. 2011) based on the elliptical

galaxies sample. The following chapters are arranged as follows: in this first chapter I present an introduction to the field of AGN research. It is meant to contextualize the reader on this topic and to highlight some of the aspects of this field that will be useful for the comprehension of this dissertation. It also serves to delineate the motivation that supports this work. Thorough analysis and descriptions of this class of objects may be found in the books by Robson (1996), Peterson (1997), Osterbrock & Ferland (2006), Krolik (1999) and Beckmann & Shrader (2012). In the discussion here presented, I will emphasize the Gaia applications to the extragalactic field, which may also be found with greater detail in Andrei et al. (2012a), Mignard (2012), Krone-Martins et al. (2013) and de Souza et al. (2014).

In Chapter 2, I describe with some degree of detail the Sloan Digital Sky Survey (York et al., 2000; Ahn et al., 2012), which is the survey from which the images to be analysed are retrieved thus being the basis of the entire project. Chapter 3 includes a brief discussion on how GALFIT works and how the required files were prepared and all the data were collected, in particular by using SExtractor (Bertin & Arnouts, 1996) so that I could successfully conclude the 2D analysis. Post-processing tasks are also described in detail, including the creation of the 1D surface brightness profiles using the capabilities of IRAF (Tody, 1986, 1993). In Chapter 4, I introduce the reader to the description of the algorithm for the construction of images of galaxies as seen by Gaia, which includes the definition of the Radon transform, to be used in simulations to assess the efficiency in recovering structural parameters of galaxies. All the results obtained from the previous chapters are then presented and analysed further in Chapter 5 so that one can extract the maximum amount of information from the available data. I discuss all the results in light of the current knowledge and summarize all the main outcomes from my work in Chapter 6. Finally, in Chapter 7 I draw attention to the main conclusions that can be taken from this project and suggest future following up studies.

1.1. ACTIVE GALACTIC NUCLEI

The name "*active galactic nucleus*" (AGN) was coined due to the observational fact that galaxies often possess an unusually high concentration of energy liberation in their central regions. This energy is not explained by the normal energy output that one would expect from stars. In addition to that, they also emit in a broad range of the electromagnetic spectrum: from radio to γ-rays. In the next subsections I will detail briefly the characteristics of this kind of objects.

1.1.1. AGN TYPES

The first evidence for the existence of an AGN was the detection of strong emission lines in the spectrum of galaxies that exceeded by far any previous class of discovered objects. But as more and more spectra were compiled, astronomers started to note that not all active galaxies possessed the same features. The emergence of such cases lead to the establishment of several types of AGN according to their main properties.

Seyfert galaxies, named after Seyfert (1943) who presented a small sample in an article about this class of objects. These are regular spiral galaxies with strong nuclear emission. Khachikian & Weedman (1974) divided this further class into two subclasses according to the broadening of its spectral lines. Seyfert type 2 galaxies have narrower ($\sigma \lesssim 1000$ km s^{-1}) forbidden and permitted emission lines than those that appear in Seyfert type 1 galaxies ($\sigma \sim 1000 - 5000$ km s^{-1}). It is observed that there are more Seyfert type 2 galaxies than Seyfert type 1 and that all Seyfert galaxies comprise around 3% to 5% of all galaxies (Maiolino & Rieke, 1995; Maia et al., 2003).

Radio galaxies, as discovered by Brown & Hazard (1959) and Edge et al. (1959), are AGNs that emit strongly at radio wavelengths. The radio emission may not be concentrated only in

the central region of the galaxy, but extends to great distances (up to hundreds of kpc and even reaching Mpc scales) via jets emanating from the nucleus. Usually in pairs, the jets consist of a collimated beam of relativistic particles moving through a magnetic field leading to synchrotron radiation emission. Whenever the jet material interacts with the intergalactic medium, it usually forms a lobe.

By looking at the optical spectra of these radio sources they might be also classified as **Broad Line Radio Galaxies (BLRGs)** and **Narrow Line Radio Galaxies (NLRGs)** in the same manner as one distinguishes the two different kinds of Seyferts. Another distinction based on their radio morphology has also been proposed by Fanaroff & Riley (1974): **FR-I** objects which have their lobes separated by less than half of the host galaxy and **FR-II** objects for which the separation is larger. They are commonly associated with weak and strong radio power, respectively.

As a powerful example of radio galaxies there are **quasars** ("*quasi stellar radio sources*"), the most energetic objects in the Universe which possess a star-like appearance in the optical domain. They first puzzled astronomers with their odd-looking spectral lines which were recognized by Schmidt (1963) as a redshifted UV spectrum that placed these objects at great distances from us. Similar to quasars there are the "*quasi-stellar objects*" (**QSOs**) which are radio-quiet, but high-luminosity AGN some with a star-like appearance in their optical images. These two types of objects are often simply referred as **quasars**. The star-like appearance is due to the high-luminosity of the central region combined with the great distance at which these objects are. Thus, the underlying host galaxy is in generally hard to detect in the images.

There is the **blazar** class (e.g. Urry & Padovani, 1995) that stands for BL Lacertae (**BL Lac**, named after its first detected object which was thought to be a variable star (Schmitt, 1968)); Optically Violent Variable sources (**OVVs**, McGimsey et al. 1975) and Flat Spectrum Radio Quasars (**FSRQ**, Andrew & Kraus 1970). They possess the common property of having highly variable luminosity on time scales as short as some hours, some emitting highly polarized photons.

1.1.2. THE PHYSICAL PICTURE OF AGN

The myriad of classes presented in the previous subsection has one thing in common: a big amount of energy is released from a very small volume in space. In the brightest quasars, their luminosity can reach values of 10^{41} W, which is 10^{15} brighter than the energy output from the Sun. The current paradigm states that such among of energy must come from the release of gravitational energy from mass accretion by a super massive and compact object, like a super massive black hole based on ideas proposed by Salpeter (1964), Zel'dovich & Novikov (1964) and Lynden-Bell (1969).

The idea behind the unification of the various classes of AGN is based on the fact that all the observed differences might be explained by a small set of parameters (Antonucci, 1993; Urry & Padovani, 1995), namely the luminosity, the relative orientation of the AGN with respect to the line of sight and the presence (or not) of radio jets.

By combining the physical model with the observed types of AGN, one is able to dissect the AGN into its various components, each of which is responsible for different observed features. The main components are summarized below:

- A **super massive black hole** with masses ranging from 10^6 up to 10^{10} $M_\odot$ which resides at the core of the AGN and has a typical size of $R_S \ll 10^{-3}$ pc;

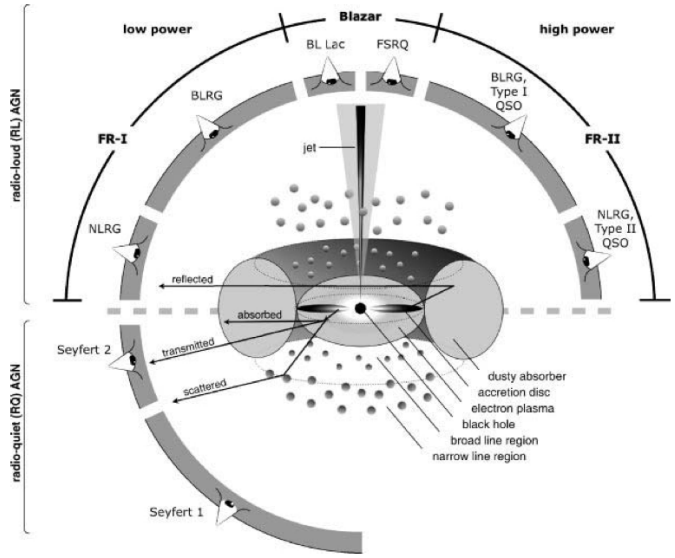

Figure 1.1. The current picture of the unified model of AGNs. Considering the line of sight of the observer with respect to the AGN orientation, the observer sees different classes of AGNs. For radio-quiet objects the orientation effect leads to the observed Seyfert classes. For radio-loud objects there is the combination of morphology+orientation effects to account for the different observed classes. Graphic courtesy of Marie-Luise Menzel for the book Beckmann & Shrader (2012, Chapter 4).

.

- An **accretion disc** of size ~ 0.1 pc composed by optically thick and hot plasma ($\sim 10^4 - 10^6$ K) which is the main driver of the energy release by the AGN and surrounds the central black hole;
- A **broad line region**, with sub-parsec scales, which accommodates clouds of high density gas that orbit the black hole at extremely high velocities. The gas is excited by the radiation that comes from the accretion disc and emits permitted and broad emission lines of ionized elements;
- This central part of the AGN is enclosed by a **dusty molecular torus** with several parsecs in size. Its inner boundary is defined by the sublimation temperature of the dust, which is around 1500 K;
- At even larger distances, from 10 to 1000 parsecs, it is located the **narrow line region** which is composed of lower density gas clouds that are mostly located upwards and downwards the torus. The photons coming from the radiation field of the central region of the AGN ionize the atoms of the clouds producing permitted and forbidden lines with narrow widths;
- Finally, collimated **jets** originating from the AGN core and perpendicularly to the accretion disc extend out to several kpc and up to Mpc scales. The interaction of the jets with the surrounding medium leads to the production of **lobes**.

Since different regions are harbouring different physical phenomena that produce photons in different ranges of energies, it is expected that looking through different directions yield different observations of the same object. As seen from figure 1.1., the orientation of the line of sight with respect to the AGN modifies its observational properties thus changing the object classification.

1.1.3. THE SPECTRAL ENERGY DISTRIBUTION OF AGN

As stated before, the emission of the AGN covers the entire electromagnetic spectrum and its typical energy distribution along the spectral range is summarized in figure 1.2.. Below I will

describe the physical processes underlying the continuum emission in each wavelength range focusing on the radio and optical regimes.

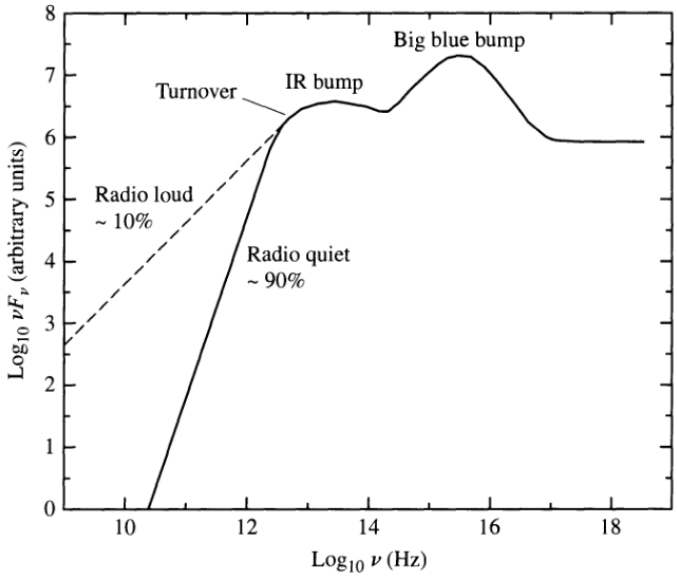

Figure 1.2. Schematic distribution of the spectral energy of a typical radio quiet and radio loud AGN source. From Carroll & Ostlie (2007, chapter 28).

Starting with the radio regime, the main physical process among radio-loud objects is *synchrotron radiation*. This radiation is characterized by photons emitted from accelerating relativistic electrons moving along spiral paths around the lines of the magnetic field. In terms of morphology there is the extended emission associated with the jets and the lobes (the regions of interaction of the jet material with the surrounding environment) of the AGN. There is also the compact component, often named core emission, which is thought to be related with the region where the jet forms and where it is believed to be optically thin. It is the combination of the multiple synchrotron emission of electrons at different speeds that produces the observed shape of the SED in the radio regimes. It consists of a simple power law, $F_\nu \propto \nu^{-\alpha}$, where α is the spectral index and varies according to the region one is considering. By comparing the flux of the continuum from the radio to the optical one derives the useful quantity (Beckmann & Shrader, 2012)

$$R^* = \frac{f_{\text{radio}}}{f_{\text{B}}}, \tag{1.1}$$

which is used to define the separation between radio quiet ($R^* < 10$) and radio loud ($R^* > 10$) galaxies. It is found that nearly all AGN ($\sim 90\%$) are radio quiet.

In the infra-red regime there can be thermal and non-thermal origins for this emission. For radio-loud objects, namely blazars, the synchrotron radiation may dominate in this regime, and in other AGNs dominates the dust emission.

One striking feature of the optical regime is the **big blue bump** in the continuum emission thought to be of thermal origin and which extends into the ultraviolet range. This bump is thought to be the black body radiation emanating from the hot gas in the accretion disc around the central black hole. There is another small blue bump, often unnoticed, that is considered to be to a blended emission of iron lines and the Balmer continuum. Jets might also contribute to the optical emission in certain configurations. Apart from the continuum features the presence of strong narrow or broad emission lines also marks the optical spectrum of AGNs.

As an extension to the optical regime, the UV range of the AGN SED is dominated by the thermal emission, strong lines (emission and absorption) related to the central hot gas of the accretion disc.

The X-ray spectrum reflects two different physical regimes. The first, at lower energies ($\lesssim$ 1 keV), is generated by inverse Compton scattering of photons emitted from the thermal emission of the accretion disc by the electrons of the hot gas that surrounds the central region of the AGN. The second, referred as the "*reflection hump*", between 10 and 30 keV (George & Fabian, 1991) which comprises photo-absorption, iron fluorescence and Compton scattering of relatively cold gas very near the central black hole.

1.1.4. AGN GALAXY HOSTS

All AGNs reside in galaxies. Even the most elusive and compact hosts have been revealed in deeper studies of a number of objects. Nevertheless, in the case of the quasars, is really hard to detect the hosts with current instruments, either because they are too compact, too faint or simply because the contrast between the central powerful AGN and the extended emission from the galaxy is huge (Bahcall et al., 1997). And, since they reside inside galaxies there is a lot of discussion around the influence of the host galaxy in the AGN and vice versa. Comprehensive reviews on this topic may be found, for example, in Veilleux (2008), Cattaneo et al. (2009), Fabian (2010) and Kormendy & Ho (2013).

The open topics under scrutiny in this particular field are aiming to uncover any relations that might exist between the properties of the AGN and of its host galaxy. It appears that there is a relation between the Hubble type of the galaxy and the amount of matter that is accreted by the black hole (e.g. Ledlow & Owen, 1995; Falomo et al., 2014). And, there are some relations that have been proposed that relate the host mass, or the mass of the bulge of the host with the mass of the black hole (e.g. Gebhardt et al., 2000; Häring & Rix, 2004). The tendency found is that more massive black holes are encountered in the heart of the most massive galaxies, which in turn tend to be ellipticals rather than spirals. There is also an attempted connection between the star formation of hosts and the power of the AGN which in turn relates to the feedback (the impact of the AGN on the star formation of the host galaxy) problem, which is not yet fully understood (Santini et al., 2012, and references therein).

Other related subjects concern the growth of the mass of the central black hole (see Kormendy & Ho, 2013, for a detailed discussion). Whether it happens via mergers of smaller ones or instead via a continuous secular growth by mass accretion of matter of the host galaxy it is still open to debate. Both seem to play their part, but far too much is still to be found in future research.

1.2. OPTICALLY PASSIVE ELLIPTICAL RADIO GALAXIES

Elliptical galaxies tend to be passive in the sense that they produced little or no amount of new stars in their recent past (1-2 Gyr, e.g. Sparke & Gallagher, 2007, chapter 6). Therefore, their bulk of emission comes from older stars, and less massive stars which have not yet succumbed to their fate. These kinds of stars are cooler that the young and massive stars thus presenting redder colours.

Radio-loud AGNs are mostly found in elliptical galaxies (Taylor et al., 1996). Among the low luminosity radio-loud objects there are some that show little evidence for extra activity in the optical regime, even though possessing strong emission at the radio regime (e.g. Antón et al., 2004; Antón & Browne, 2005). These particular type of AGN tend to live in red elliptical galaxies

and have therefore been named as *Optically Passive Elliptical Radio Galaxies* (OPERGs). The fact that in the optical domain the nuclear emission is diluted in the stellar component makes them good targets for the analysis of their hosts.

In what regards their SED some of these objects have similar properties to BL Lacs in some regions of the electromagnetic spectrum when not taking into account the optical and near-infrared emission, which are dominated by stellar emission. They present a smooth transition from radio to sub-millimetre regimes (Antón et al., 2004) and sometimes a core-jet radio morphology (Antón et al., 2004; Bondi et al., 2004). In many aspects they are indistinguishable from BL Lac objects in the longest wavelength regimes, and has been proposed that OPERGs are blazars with a low frequencies peak in the non-thermal component or intrinsically weak AGN (Bondi et al., 2004).

1.3. THE INTERNATIONAL CELESTIAL REFERENCE FRAME

Ideally, a celestial reference frame should be established by the same objects observed at all wavelengths (Walter & Sovers, 2000). This would make easier to establish cross-identifications between sources detected from the radio to γ-rays wavelengths. In practice, such construction is not easy to achieve since there are not in the Universe many objects that fulfil all the requirements to constitute a good reference source: being bright, compact and without proper motion (Taris et al., 2013). Being powerful, emitting in several wavebands and apparently very compact, quasars are among the best candidates to provide a link between reference frames in the optical and radio domains. The fact that they are at big distances from us also minimizes the problems of proper motions that would imply a limitation in the definition of the reference frame. However, at optical wavelengths, they might not be bright enough to be detected or even if brighter enough they might not possess compact morphology in their radio emission (Orosz & Frey, 2013; Taris et al., 2013).

Nowadays, the best precision that astronomers can achieve in the measurement of absolute positions happens at radio frequencies (Charlot & Bourda, 2012) and the *International Celestial Reference Frame* (ICRF) is based on observations of distant sources (namely blazars) using Very-Long-Baseline Interferometry (VLBI) radio telescopes. The first version of the ICRF (Ma et al., 1997; Ma & Feissel, 1998) was defined by the positions of 212 compact radio sources. However, the compilation of additional data and new observations of additional sources with time lead to the 2$^{\text{nd}}$ realization of the ICRF, which is now composed of 295 defining sources[1] and is referred as ICRF2 (Fey et al., 2004, 2009).

Objects with core radio morphology, absent proper motions, apparent optical point-like nature are assumed to have a high degree of accuracy and stability of their coordinates and for that reason they can help on the alignment between the ICRF andjm reference frames of similar accuracy like the Gaia mission (Bourda et al., 2008), (Bourda et al., 2010), (Bourda et al., 2011), (Mignard, 2012), (Charlot & Bourda, 2012), (Andrei et al., 2012a), (Andrei et al., 2012b) and (Taris et al., 2013). The high astrometric accuracy of Gaia will make possible to establish a reference frame in the optical domain.

While it is not yet possible to get the astrometric measurements of Gaia, we can study the suitability of the candidates for the alignment between the two reference frames based on existing and public data such as the *Sloan Digital Sky Survey* (SDSS) which is the largest sky survey that we can access. There are several works devoted to the issues related with offsets between the radio and optical centroids (e.g. Orosz & Frey, 2013, and references therein). Here, we

[1] A defining source is a source which has high-astrometric-quality over the entire period of observations available and because of that, it can be used to define the main axes.

concentrate in the impact that the AGN host galaxy may have for the astrometric accuracy at the optical band. In that sense, a census of the available images of the already radio accurate reference sources to inspect their morphological structure is necessary to verify the detectability of the host galaxies.

1.4. ASTROMETRY: FROM HIPPARCHUS TO GAIA ERA

Astrometry is as old as men. It refers to the study of the geometrical relations between objects in the sky and their motions and it has been fundamental in the progress of astronomy until the 19^{th} century. Nowadays it remains a basic element fundamental for any astronomical related research.

The first geometrical relation that one often uses is the parallax. This effect occurs as a natural consequence of the motion of the Earth revolving around the Sun. The idea is to compare the position of a nearby object observed with a separation of six months which is roughly the time that Earth takes to move between opposite positions in relation to the Sun. As seen in figure 1.3., this will produce a separation between the two apparent positions of a nearby source. The parallax is then defined as half the angular separation of a source's position observed at opposite Earth locations with respect to the Sun. By using the measured parallax it is straightforward to use the trigonometric relations to compute the distance from the Earth to the source as

$$\sin(\pi) = \frac{1\text{AU}}{d}, \quad \text{which for } \pi \approx 0 \text{ becomes } \quad \pi \approx \frac{1\text{AU}}{d}. \tag{1.2}$$

This measurement is even used to define a commonly used unit in astronomy: the parsec, which is, by definition, the distance that a source has to be to produce an observed parallax of one second of arc. Despite simple, this technique is limited by the resolving power of current telescopes as much of the angles that one has to measure are extremely small.

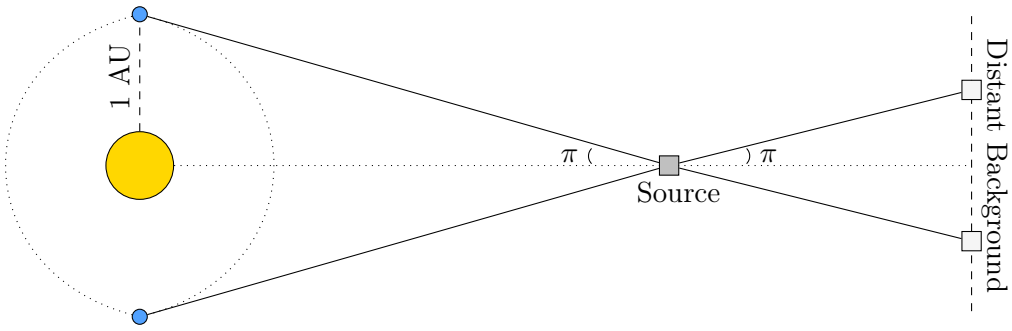

Figure 1.3. Parallax definition from the opposite positions of the Earth (blue circle) relative to the Sun (yellow circle) and the apparent position of the source (grey rectangle) superposed in the background (light grey rectangles). The angle π is the parallax of the source.

Apart from measuring distances, astrometry also serves to determine the motion of objects in the space relative to each other. This motion can be further separated into two components, the radial velocity, which is measured along the line of sight and the proper motion, which is the transverse movement across the sky. The first is easily measured from observing the Doppler shifts in the spectral lines of the source by contrast the second is much more difficult to determine as it requires careful observations of the object with respect to many others over an extended period of time, usually years.

Obtaining distance and motions of objects is crucial to our comprehension of how the Universe works. Using the distance we can determine the luminosity and size of the object one is

considering, using the motions we can infer its trajectory in both time directions: future and past.

It was in the dawn of mankind, many centuries ago that men started to look to the heavens. They realized that objects moved in a particular and regular way across the sky thus rendering it useful to determine directions and time on the Earth surface. The urge to plan their life hastened the need for precision astrometry so that one could, for instance, maximize the output from a plantation by planting and harvesting at the right moments.

In ancient Greece, around 100 B.C., with no help from any instrument, Hipparchus compiled the first catalogue of sources with specified brightness and positions as accurate as one degree, which is roughly two times the diameter of the full moon. This first catalogue marked the birth of astrometry. After that, it has seen little progress until the 16^{th} century when Tycho Brahe revolutionized the field, establishing a new accuracy limit in $\sim$1 minute of arc (60 times better that Hipparchus). He designed, built and then calibrated a variety of measuring instruments like the sextant or the mural quadrant, which greatly changed the way observations were done. It was Tycho's measurements that allowed Kepler to later establish that the planets moved in elliptical orbits around the Sun.

With the invention of the telescope in the early years of the 17^{th} century new doors opened to achieve better precision and measure even smaller angles. Combined with a mechanical support that allowed to precisely move the telescope (the filar micrometer invented later in that century) it allowed scientists to break the barrier of one minute of arc imposed by the limitation of our eyes. The improvement of other techniques such as the possibility to engrave observations allowed for the detection of the stellar aberration in 1725 and the detection of the motion of sources in the sky by Edmund Halley. This evolution of the technology leads to the first measurements of the parallax in the 1830s laying grounds to the idea that those bright sources that we observed were actually at finite distance from us and had mankind rethink our place in the Universe. The limits were pushed further down to ~ 0.1 arc seconds, which is the limit of Earth observations imposed by atmospheric effects.

It was only in the end of the last century that the first space based telescope dedicated to astrometry, Hipparcos, was launched by ESA in 1989, and allowed an improvement of 100 times more precision than previous studies and compiled a list of $\sim$120000 objects with precisions of one milliarcsecond. Following this success, ESA has planned a new mission, Gaia, to increase even further our measurements in precision (see figure 1.4.) and in number of observed sources. This mission is described with greater detail in the following subsection.

1.4.1. GAIA GALAXY-MAPPING SATELLITE

Gaia, whose name originated as an acronym of *Global Astrometric Interferometer for Astrophysics* (despite not having an interferometer in its final design, the name has been maintained), is a successor to ESA's Hipparcos mission and it was launched in December 2013. It is stationed at the L2 Lagrangian point of the Sun-Earth system, 1.5 million km from the Earth in the direction away from the Sun. As an ESA space-based mission, planned during the 90s, it has as its main goal performing astrometric measures of galactic sources in order that we can reconstruct 3-dimensional maps of our vicinity with an unprecedented precision of ~ 7 μas for sources up to $G = 12$[2] and ~ 25 μas for fainter objects up to $G = 15$ and a maximum precision of 30 mas for the faintest objects detected with $G \approx 20$. It will provide a major improvement on parallax measured distances of roughly ten million stars in a 2.5 kpc radius with 1% precision. In addition, Gaia is expected to discover large numbers of other celestial bodies such as comets, asteroids,

[2]G band magnitude corresponds to the total integrated flux measured between 3300Å and 11000Å.

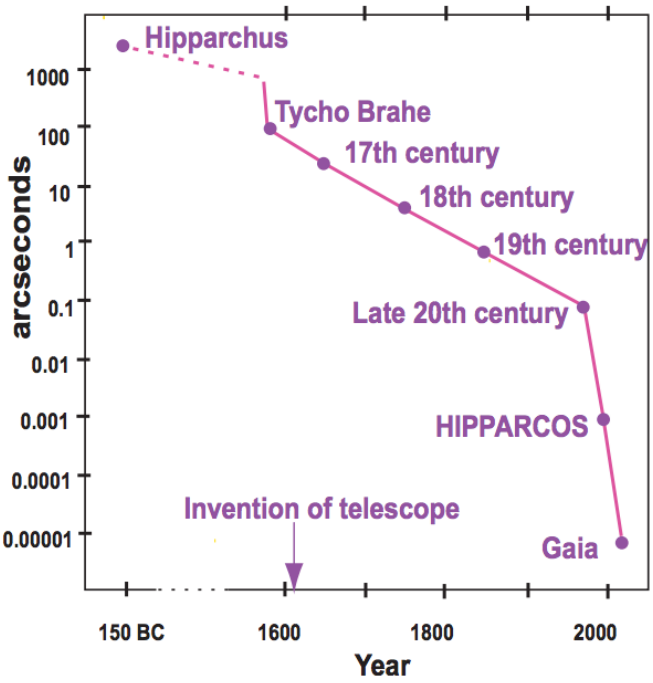

Figure 1.4. The evolution of the accuracy in astrometry measurements throughout time. Adapted from *The Little Book of Gaia: History of Astrometry*: `http://www.esa.int/Education/Little_Books_of_Gaia`.

exoplanets, brown dwarfs, variable stars and supernovae. Nonetheless, despite its main goal of measuring distances within the Milky Way, its sensitivity will allow the detection and observation of extragalactic objects of extended nature and point-like sources such as quasi-stellar objects (QSOs). This measurements will then allow a direct establishment of an extragalactic celestial reference frame (*Gaia Celestial Reference Frame* - GCRF) derived in the optical range.

The Gaia strategy to obtain precise astrometric measurements consists on measuring angles between distinct objects, which is made possible by multiple observations of the same targets in different orientations (different great circles passing through a given object). To complete its objective, Gaia is composed of two identical telescopes with rectangular mirrors which observe almost opposite regions of the sky (106.5° apart) with a continuous precession movement allowing for a complete census of the celestial sphere. The satellite completes a great circle every six hours and has a 63-days cycle of the precession movement. Each of the telescopes has a mosaic of 106 CCDs of 4500 × 1966 pixel each. Each pixel has the particularity of being rectangular covering a region in the sky of 59×177 mas (see figure 1.5.).

This mosaic of CCDs has different sets of columns each corresponding to a specific science objective. Those columns are highlighted in different colours in figure 1.5.. The first two columns are named as Sky-Mappers (SM) and each of them is responsible for the detection of sources from light coming from a specific telescope, i.e., the first column serves to detect sources coming from one telescope and the second column to detect sources observed from the other telescope. The other CCD columns receive the light coming from both telescopes. As Gaia is constantly moving across the sky, the sources detected in the first two columns will be followed across the nine columns that compose the Astrometric Field (AF). The first eight columns have seven rows of CCDs and the last one has only six rows. This configuration will allow the instrument to follow and record the position of each source as they move from one column to another. After going through the Astrometric Field, the light of each source passes through a blue photometer,

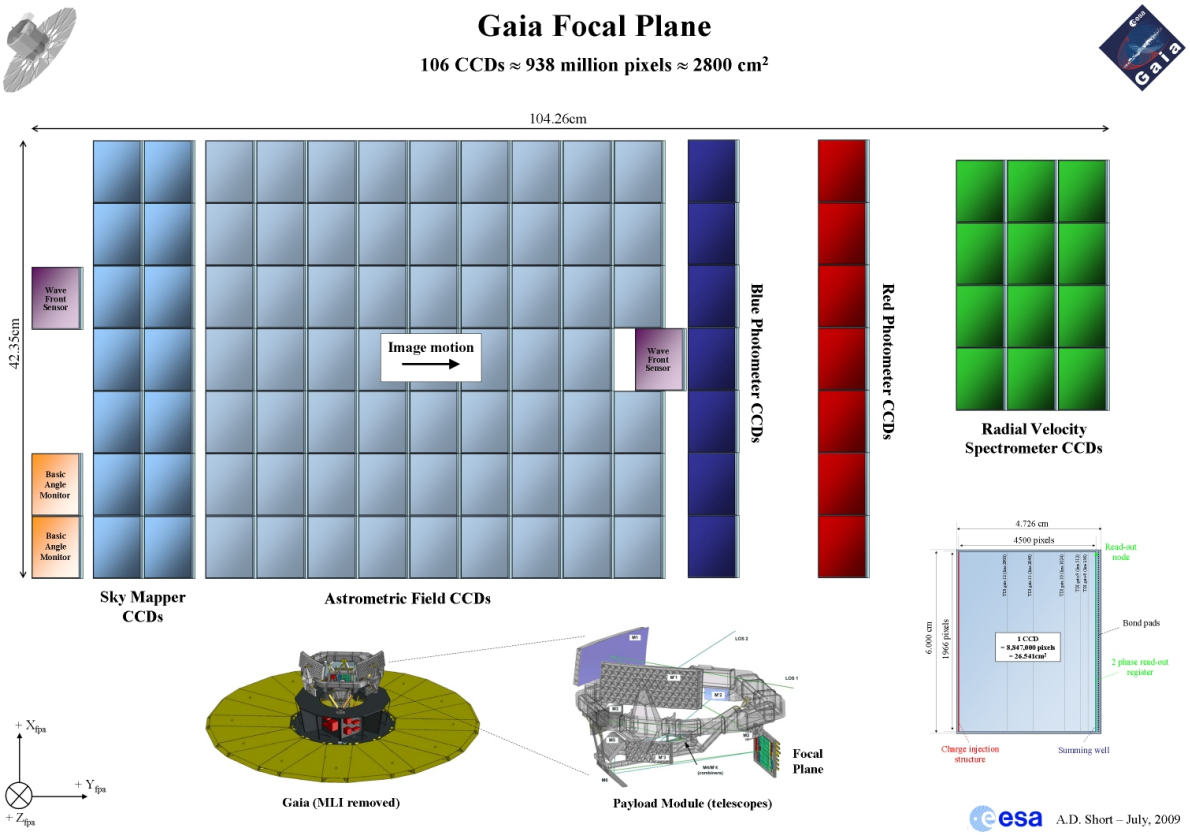

Figure 1.5. Scheme of the CCD mosaic on board of Gaia. Credit: Alexander Short - ESA.

measuring light from 3300 to 6800 Å, and then by a red photometer measuring the light from 6400 to 10000 Å. This is done in order to obtain magnitudes in different regions of the optical spectrum which will be used to characterize some physical properties of the observed objects. The final set of CCDs is part of the Radial Velocity Spectrometer instrument which will be used to measure Doppler shifts in the Ca II triplet lines by observing in the narrow band of 8470 to 8740 Å. These columns only examine the sources of first four rows of the Astrometric Field. Such measurements will allow for the measurement of the velocity of the observed stars along the line of sight.

Due to the huge amount of pixel information stored in theses mosaics, the transmission of the full observed data to Earth stations is technically impossible. In order to circumvent this issue, there is an on-board processing unit, which is responsible for the selection of the data to be transmitted. To do so, if a source is detected in the SM columns the movement of the source is followed in the AF columns by assigning a subset of pixels to the object to be stored in memory. Then, according to the source magnitude and its position on the CCD mosaic, the observed values are binned into the final data values which will be then transmitted to Earth. The window sizes as a function of CCD columns and source magnitude are displayed in table 1.1..

In this way, the data that reaches a ground station and will be subsequently analysed corresponds to a window around object composed of samples each of which is a sum along the binning directions of the observed window. For example, a $G = 15$ magnitude object will be transmitted from AF2 as a set of 18 values where each value corresponds to the sum of the 12 pixel along the perpendicular direction of the CCD movement (see figure 1.6. for a schematic representation). For most cases ($G > 13$) in the Astrometric Fields only 1-dimensional data will be transmitted to Earth. Thus, in order to be able to analyse the extended emission of extragalactic sources it

will be necessary to reconstruct the 2D signal from the set of available data via a well-known mathematical process which uses the Radon transform of the signal and is, for instance, widely used in Computerized Tomography scans.

CCD column	G mag	Window Size (read, in pixel)	Binning factor	Window size (in sample, transmitted)
SM	G<13	80×12	2×2	40×6
	G>13	80×12	4×4	20×3
AF 1	G<13	18×12	1×2	18×6
	13<G<16	12×12	1×12	12×1
	G>16	6×12	1×12	6×1
AF 2,5,8	G>16	18×12	1×1	18×12
	13<G<16	18×12	1×12	18×1
	G>16	12×12	1×12	12×1
AF 3,4,6,7,9	G>16	18×12	1×1	18×12
	13<G<16	12×12	1×12	12×1
	G>16	6×12	1×12	6×1

Table 1.1. Window sizes of Gaia imaging processing data as a function of CCD column and source G band magnitude. Translated from Krone-Martins (2011, chapter 2).

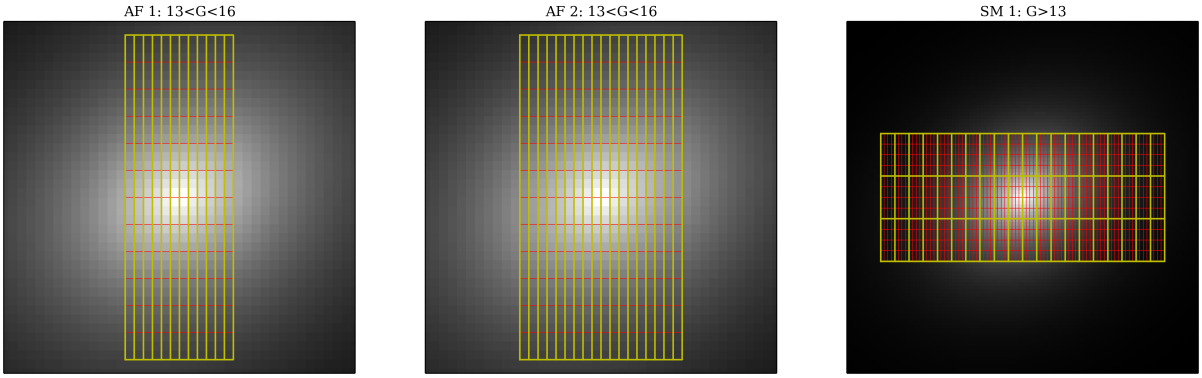

Figure 1.6. Window over position of different CCD columns on top of simulated images of idealized galaxies with Sérsic profiles. The yellow lines represent the samples to be transmitted to Earth while the red lines represent the pixel limits of the CCD. For the AF columns, the image is zoomed to better understand the window configuration.

CHAPTER 2

DATA & SAMPLE

"[T]he key to making progress is to recognize how to take that very first step. Then you start your journey. You hope for the best and you stick with it, day in and day out. Even if you are tired, even if you want to walk away. You do not."

- Man On The Moon; Grey's Anatomy

Contents

As said in the previous Chapter, two sets of objects are under study in this dissertation: the ICRF objects which are believed to be mainly point-like sources in the optical regime and a sample of nearby optically passive elliptical radio galaxies. Given the objective of investigating the presence of any extended component that might perturb the astrometric evaluation of the object's position, it is important to refer the parent sample and describe the real sample under scrutiny. The mentioned samples are not the same due to SDSS limitations in terms of covered regions. Details on each of the defined samples and on the SDSS survey used to carried out this project are explained in detail in the sections that follow.

2.1. DATA FROM SLOAN DIGITAL SKY SURVEY

The *Sloan Digital Sky Survey* (SDSS, York et al. 2000) is one of the greatest survey projects of modern astronomy. Its huge efforts are aimed to map around 25% of the sky and determine the position and apparent magnitude of more than ten billion objects. It also comprises a spectroscopic follow up that serves to measure up to a million redshifts of local galaxies and distant bright quasars. With its fourteen years of operations, divided in three phases (SDSS-I, 2000-2005; SDSS-II, 2005-2008; SDSS-III, 2008-2014), it is the most extensive survey ever taken and its wealth of data allows scientists around the world to significantly advance in the understanding of extragalactic astronomy and unravelling the steps that take place in the evolution of galaxies. In this section, I briefly describe the survey and I point out your attention for the SDSS astrometry and photometry quality to my study.

2.1.1. THE SURVEY

A dedicated 2.5-meter wide-angle optical telescope at Apache Point Observatory in New Mexico, United States of America, consists of an imaging survey of π steradians of the northern Galactic cap and also of a smaller area ($\sim$225 deg^2) but much deeper images toward the southern Galactic cap. It takes images using a photometric system of five contiguous photometric bands - u, g, r, i and z - centred at 3540, 4770, 6230, 7630 and 9130 Å and with 95% completeness in typical seeing down to magnitudes of 22.0, 22.2, 21.3 and 20.5 mag, respectively. The filter system, described by Fukugita et al. (1996), covers the entire optical range from the near ultraviolet, where the limitation comes from the atmospheric absorption cut-off below $\sim$ 3000 Å, to the redder limits imposed by the characteristics of the silicon that looses its sensitivity to photons with wavelengths larger than $\sim$ 11000 Å. The transmission curves of the CCD in the SDSS's five filters is shown in Figure 2.1. as a function of observed wavelength.

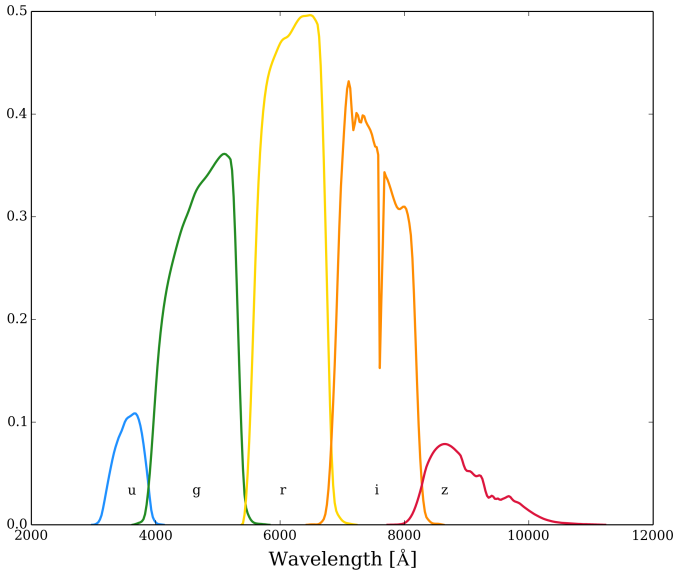

Figure 2.1. Transmission curves of the SDSS ugriz filter system plotted from the available tables at `https://www.sdss3.org/instruments/camera.php#Filters`.

To take the images, the telescope uses a drift scanning technique which consists of keeping the telescope pointed to a fixed region of in the sky and then takes advantage of the Earth's rotation to map contiguous strips of the celestial sphere. As opposed to tracked telescopes, this technique allows for a more precise astrometric measurements over the wide field of view of the telescope as it is not affected by errors in the tracking movement of those systems that surely affect the position determination. However, this means that small distortions in the images are produced due to movement of the sources in the CCD focal plane. To minimize such distortions, the exposure times and reading times of the CCD must be kept to small values sacrificing thus the deepness of the survey.

The telescope is equipped with a 120-mega pixel camera composed of thirty CCD chips with 2048×2048 pixels which are arranged in five rows of six chips where each row has its own filter to simultaneously image the observed region in the five photometric bands. This camera can observe 1.5 square degrees of sky in a single observation, which is about eight times larger than the area of the full moon. It also has two spectrographs which are fed by optical fibers covering a circular region of 3" in diameter which are placed in the centre of the sources one wants to observe to measure the spectra (and thus redshifts/distances) of 1000 galaxies and quasars in a single snapshot (the original set-up of SDSS-I and SDSS-II allowed for a maximum of 640 targets

per pointing). It is interesting to note that the two key discoveries/technologies that are crucial to the functioning of SDSS, optical fibers and CCDs, were both awarded the 2009 Nobel Prize in Physics.

After obtaining the observations, a specific set of software pipelines processes the raw data obtained from the telescope to produce quality science images which are then ready for scientific exploitation. These pipelines also produce lists of observed sources and some of their related parameters, such as whether they seem point-like (like quasars or stars) or extended (as a galaxy usually is) and their apparent magnitude. The imaging data is processed with an automatic software pipeline called PHOTO (Lupton et al. 2002, 2001) and the morphological information derived from the images allows for robust star–galaxy separation to ~ 21.5 mag (Lupton et al. 2001; Yasuda et al. 2001).

2.1.2. ASTROMETRIC/PHOTOMETRIC QUALITY

To obtain reliable results from any image analysis done in astronomy, the quality of the main quantities must be assured. Those quantities are related with three techniques that are paramounts in any survey: photometry, astrometry and spectroscopy. Since the work carried out under this project is mainly related to image analysis, I will skip the discussion of the spectra quality assessment.

Astrometry is a useful technique that allows scientists to guide themselves through the sky. It is used to determine the true coordinates of sources, in any coordinate system that you may use or define (one ubiquitously used is the equatorial system where each position in the sky is defined by a set of two coordinates - right ascension and declination), departing from their physical position (usually in Cartesian coordinates - x and y) in the CCD. The idea that supports all astrometric solvers is simply to match a catalogue of reference sources, for which you now *a priori* the true sky coordinates, to a catalogue of detected sources in the images. In the case of SDSS, its astrometric calibration is described in great detail in Pier et al. (2003). I just want to highlight that the astrometric accuracy of the original SDSS set-up performs better than $\sim 45 - 75$ mas (depending on the reference source catalogue) which is below the minimum required accuracy of 180 mas so that the positioning of the optical fibers to obtain the spectra of sources could be executed successfully.

However, a number of issues prevented the accurate calibration of Data Releases - DR8 and DR7 - due to systematic offsets found in some measurements. These were pinpointed and a new ameliorated pipeline was designed to incorporate solutions in the DR9 release that would remove the identified errors (Ahn et al., 2012). These corrections improved the accuracy of the measured positions and allowed for a better determination of the centroid offsets of multi-wavelength comparisons like those presented in Orosz & Frey (2013). Thus, it is fully justified that one uses the DR9 data to pursue the work.

As for the photometry, it is the technique related to the quantification of the amount of light that reaches the telescope from a given source, its brightness. Then, astronomers use a logarithmic scale to assign to each object an observed magnitude, which is simply defined as

$$m = -2.5 \log_{10}(B) + C, \tag{2.1}$$

where B is the measured source brightness and C is a calibration constant. The calibration is done using reference sources for which we have known values of m. The flux of any object is measured normally in fixed size apertures centred on the source centroid. While this may work for stars and quasars, for galaxies, due to their extended shape and often irregular surface

brightness profiles, there are other methods to do so. One consists of fitting analytical models to the galaxy image and then minimizing the residuals to obtain the best fit parameters which include the object flux/magnitude. The other computes the flux within a locally computed aperture based on the Petrosian radius. This quantity, r_p, is computed as the radius for which the average surface brightness enclosed in an annulus ($r_{p,in} < r > r_{p,in}$) is equal to η times the mean surface brightness measured inside the aperture with radius r_p (Blanton et al., 2001).

$$\eta = \frac{2\pi \int_{r_{p,in}}^{r_{p,out}} \frac{I(r)rdr}{\pi r^2(1.25^2-0.8^2)}}{2\pi \int_0^{r_p} \frac{I(r)rdr}{\pi r^2}}, \quad \text{with} \quad \eta = 0.2,\ r_{p,in} = 0.8r_p,\ r_{p,out} = 1.25r_p \tag{2.2}$$

where $I(r)$ is the azimuthally averaged surface brightness profile. The Petrosian flux is then defined as the total flux within a radius of $2r_p$.

$$F_P = 2\pi \int_0^{2r_P} I(r)dr. \tag{2.3}$$

The Petrosian magnitudes are the best measure of the total light for bright galaxies, but fail to be a good measure for faint objects. The reason behind this is that for fainter objects the effect of the seeing on Petrosian magnitude is not negligible. As the size of the galaxy becomes similar to the seeing disc, the Petrosian flux is approximate to the fraction measured within a typical point spread function (PSF), which is about 95%. Nonetheless, since I will be performing my own modelling of the galaxy surface brightness profiles I opt to choose the best magnitudes derived from the SDSS photometric data which depend on the object in question.

2.2. SAMPLE DESCRIPTION

2.2.1. ICRF2+

I took the ICRF2 catalogue that is a set of 295 extragalactic sources distributed over the entire sky and selected on the basis of positional stability and the lack of extensive intrinsic source structure. The precision of the source coordinates is better than one mas. A complementary sample of 105 optically-bright extragalactic radio sources (Bourda et al., 2011) was compiled by cross-correlating optical and radio catalogues and in order to upgrade the defining sources in the current reference frame. The precision is around $< 200\mu$as. This leads to a total of 400 sources which will be used as the parent catalogue of this project and hereafter will be referred as ICRF2+.

From the original parent catalogue, a cross-match with the available SDSS DR9 imaging data was performed to select the sample on which the analysis will be conducted. This resulted on a total of 198 sources: 123 from ICRF2 and 75 from Bourda et al. (2011). The sky distribution of the sources with and without SDSS DR9 imaging data may be found in figure 2.2.. There is HST data for 23 ICRF2 objects and 2 Bourda et al. (2011) objects (see table 7.1. in the appendix). Of these 25 sources, there are 17 which have available both SDSS and HST imaging data.

2.2.2. OPERGs

The OPERGs under study in this dissertation are part of a bigger project that aims at finding "*offset*" galaxies, in terms of their optical and radio photometric centres. For that reason, besides the morphological analysis, it is also presented the results concerning the determination of the optical centroid.

The sample is comprised by galaxies with fluxes at radio band $F_{1.4\text{GHz}} > 90$mJy (FIRST data), that show compact radio morphology in VLA maps. Apparently, they are relaxed systems with

no features like dust lanes and signs of interactions, based on a visual inspection of their SDSS images, but which will be checked by the present study. There is no evidence for an optically active nucleus based on the SDSS spectra. The final sample is composed of 28 objects with the aforementioned characteristics and their general information (name, coordinates, redshift and additional surveys where they were detected) is summarized in table 7.2. and their sky distribution can be seen in figure 2.2..

All galaxies of the sample have therefore SDSS imaging data as it was a pre-requisite to inspect visually their overall shape and four of them have available HST imaging data on the required range of filters (see table 7.2. for more information on this).

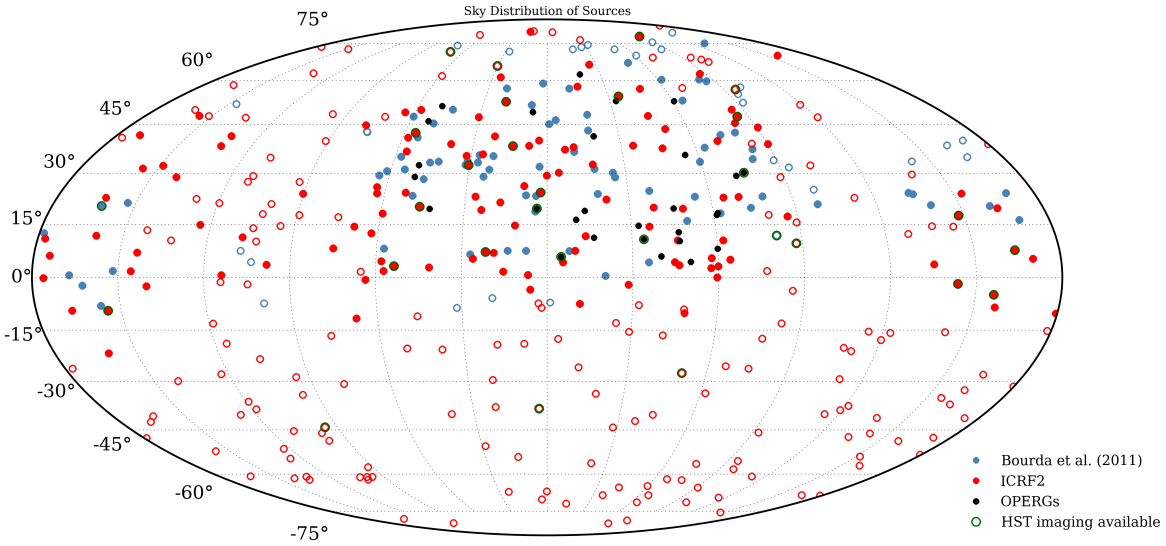

Figure 2.2. Sky distribution of the ICRF2+ sources and the OPERGs sample. Filled circles indicate those for which SDSS DR9 imaging data is available. Open green circles indicate those who have HST imaging available.

This page intentionally contains only this sentence.

CHAPTER 3

MORPHOLOGY THROUGH SURFACE PHOTOMETRY

"They take pictures of mountain climbers at the top of a mountain. They are smiling, ecstatic, triumphant. They do not take pictures along the way 'cos who wants to remember the rest of it. We push ourselves because we have to, not because we like it. The relentless climb, the pain and anguish of taking it to the next level. Nobody takes pictures of that. Nobody wants to remember. We just want to remember the view from the top. The breathtaking moment at the edge of the world. That is what keeps us climbing. And it is worth the pain. That is the crazy part. It is worth anything."

- Push, Grey's Anatomy

Contents

In order to proceed in the study of the selected objects several tasks were performed to ensure that all the required information was available. All the optical band images were taken from SDSS DR9 sky server [1] from which I downloaded the r-band corrected frames (calibrated and sky-subtracted images), the tables containing all the information related to the observation (such as the dark current, the gain of the CCD and the airmass at the time of observation) from the *photoField* files. The information pertaining to the photometric calibration and the point spread function (PSF) fit for each field were retrieved from the *psField* files. In addition, I matched my objects against the Stripe 82 database [2] and found that two out of the 198 objects were present. Similar data because Stripe 82 data is stored as the SDSS DR7 file system, as stated above was also retrieved for these objects.

3.1. SOURCE EXTRACTION WITH *SEXTRACTOR*

Since GALFIT requires an initial set of parameters, it is necessary to provide it with realistic guesses so that the fitting procedure can find the model that best fits the data faster and with

[1] `http://skyserver.sdss3.org/dr9/en/`
[2] `http://cas.sdss.org/stripe82/en/`

reliable values. So, to construct the set of the initial parameters for each galaxy to be modelled, I used the public available source extraction software SExtractor Bertin & Arnouts (1996), version 2.8.6. The parameters obtained for each source in the square region of the original tile on which GALFIT would run are X_IMAGE and Y_IMAGE (the position of the object), MAG_AUTO (the object magnitude), FLUX_RADIUS (the radius enclosing 50% of the total flux, i.e., the effective radius), A_IMAGE (the semi-major axis, a), KRON_RADIUS (the radius enclosing approximately 90% of the total light), ELLIPTICITY (the object ellipticity, $e = 1 - b/a$), THETA_IMAGE (the angle between the semi-major axis and a vertical line), CLASS_STAR (a parameter used to distinguish stars from galaxies). As an estimate for the Sérsic index I used the ratio between the effective radius and the Kron radius (see section 8.5.3 of the manual stored in `http://mensa.ast.uct.ac.za/~holwerda/SE/Manual.html` recommended by the author of SExtractor.)

$$n \approx \frac{r_K}{r_e}. \tag{3.1}$$

One can also have access to the segmentation map images which contained all the pixels that were assigned to detect sources in the image by running SExtractor. This can be useful for establishing the number of extra detected sources in the region image.

3.2. 2D MODELLING WITH *GALFIT*

GALFIT Peng et al. (2002, 2010) is a public available algorithm designed to perform a detailed 2-dimensional decomposition of galaxies using parametrized models from the literature. For the purpose of this work, the most recent version of the code, v3.0.5, was used. In the next paragraphs I describe the basics behind the process of fitting models to galaxy images.

The first step to perform the generation of 2-dimensional models consists on creating a model galaxy based on the set of shape parameters necessary: $x_c, I(r), y_c, q, \theta$. To do so, first we have to compute the distance to the galaxy centre based on the ellipse equation (normalized to the major axis)

$$\frac{x^2}{a^2} + \frac{y^2}{b^2} = \frac{r^2}{a^2}, \tag{3.2}$$

where a and b are the major and minor axis respectively. However, in order to reproduce an ellipse not centred at the origin and with the axis of the ellipse rotated in respected to the coordinate system we have to perform two transformations: a translation between the coordinate system origin and the galaxy centre and a rotation around the centre of the galaxy of the given angle θ. That is performed by the set of equations:

$$x_{rt} = (x - x_c)\cos(\theta) - (y - y_c)\sin(\theta) \tag{3.3}$$

and

$$y_{rt} = (x - x_c)\sin(\theta) + (y - y_c)\cos(\theta). \tag{3.4}$$

Now, the distance to the center of the galaxy in this new coordinate system (in elliptical form) is simply

$$r = \sqrt{x_{rt}^2 + \frac{y_{rt}^2}{q^2}}, \tag{3.5}$$

where $q = b/a$. Using this definition of r in the desired surface brightness profile we can generate a 2D model of the galaxy from the set of parameters given. This model may be further improved by applying other coordinate transformations such as the inclusion of spiral patterns or the deformation of the ellipse shape into a more boxy or diamond shape (Peng et al., 2010). One can even combine any number of different profiles to fit complex galaxy shapes or multiple galactic components.

Besides the well-known Sérsic (1968) model which will be described later on, there are other models that describe the way light is distributed in astronomical sources. For instance, Gaussian models are normally used in modelling the point spread function of the images. The Moffat (1969) is also used for the same purposed, but is better suited to space based images PSFs. The modified Nuker profile (Lauer et al., 1995) is normally used to fit the central regions of bright elliptical galaxies. The modified Ferrer profile (Binney et al., 1987) is often used for galactic bars or lenses and finally the empirical King profile (Elson, 1999) for fitting profiles of globular clusters.

To choose the best model for the observed galaxy GALFIT uses the value of χ^2_ν (reduced χ^2) defined as

$$\chi^2_\nu = \frac{1}{N_{dof}} \sum_{x=1}^{n_x} \sum_{y=1}^{n_y} \frac{galaxy(x,y) - model(x,y)}{\sigma(x,y)} \tag{3.6}$$

where

$$model(x,y) = \sum_{\nu=1}^{n_m} f_\nu(x, y, \alpha_1, ..., \alpha_n), \tag{3.7}$$

which has as many components of parameters $\alpha_1, ..., \alpha_n$ as one wishes. N_{dof} is the number of degrees of freedom of the proposed model and $\sigma(x,y)$ is the error image that associates each image pixel to its *rms* error. Note that masked pixel values do not enter in the calculations above. After setting up the required model GALFIT proceeds as follows: it generates a model based on the first guess of parameters on top of an empty canvas of the same size of the region one wants to explore. Then, it convolves the model with the user provided PSF (whenever available) using a convolution box size defined by the user in the parameter file. After, that it replaces the convolved section of the model in the original model image. Next, it computes the value of χ^2_ν by subtracting the model image to the original data. This minimization is repeated iteratively until convergence is attained. The process is done via a Levenberg-Marquardt algorithm (Press et al., 1992) improved with a downhill gradient method to fasten the way convergence is reached by optimizing the selection of the next set of parameters to be tested. Convergence is reached when the difference between N consecutive values of the χ^2 is smaller than a defined tolerance. For GALFIT, $N = 5$ and the tolerance is 5×10^{-4}.

3.2.1. GALFIT FILES

From the myriad of the available surface brightness models GALFIT provides only two were selected to perform this study: the PSF profile which adjusts the given PSF to the magnitude that better fits the object and the Sérsic (1968) profile, which is characterized by the functional form

$$I(r) = I_e \exp[-\kappa(r/r_e)^{1/n} + \kappa], \tag{3.8}$$

where the Sérsic index n describes the shape of the light profile, r_e is the effective radius of the profile, I_e is the surface brightness at radius $r = r_e$ and κ is a parameter coupled to n (see for example Ciotti & Bertin 1999) such that half of the total flux is enclosed within r_e. An index of

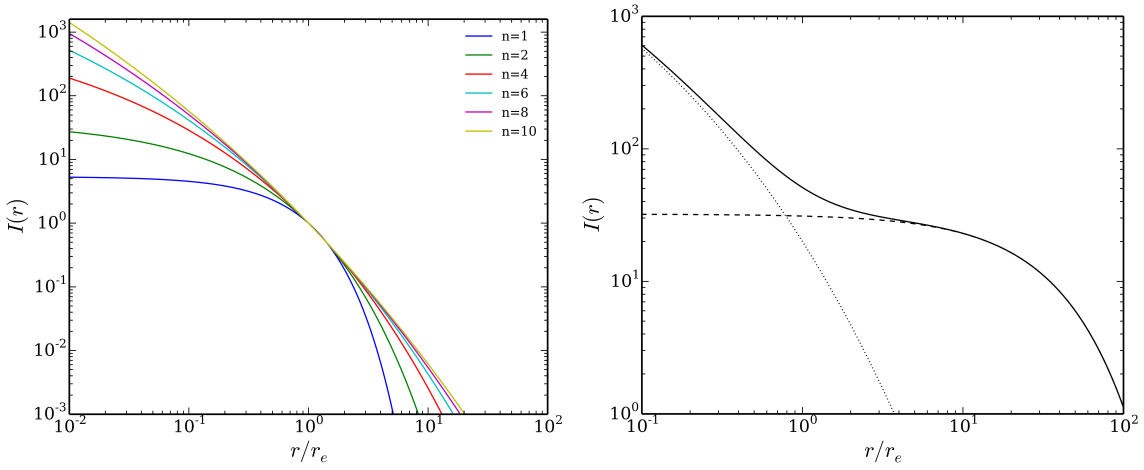

Figure 3.1. Surface brightness profiles proposed by Sérsic for different values of n (left). On the right we have a composed model (solid line) which is a sum of an exponential disc profile, $n = 1$ (dashed line), with a de Vaucouleurs profile, $n = 4$ (dotted line).

$n = 1$ corresponds to a typical pure disc galaxy, whereas $n = 4$ corresponds to the de Vaucouleurs profile associated to elliptical galaxies. On 2D images, each Sérsic model has potentially seven free parameters: the position of the centre, given by x_c and y_c, the total magnitude of the model, m_{tot}, the effective radius, r_e, the Sérsic index, n, the axis ratio of the ellipse, b/a and the position angle, θ_{PA}, which refers to the angle between the major axis of the ellipse and the vertical axis and has the sole purpose of rotating the model to match the galaxy's image. It is also common to use more than one of these profiles to model separate components of galaxies, namely using multiple Sérsic profiles to model separately the extended disc and the more concentrated central bulge. On figure 3.1. we have an illustration of these kinds of profiles in the two described cases: single Sérsic with a given value of n and a composite model using two distinct Sérsic profiles with specific values of n.

The PSF model is normally used to fit a bright point source emission characteristic of AGN objects and the Sérsic profile serves to characterize the properties of the extended galaxy emission. Even though the host galaxy may have inherently more than one component (e.g. Antón et al., 2008), there have been simulations that show that a single Sérsic profile serves the purpose of AGN+host image decomposition in HST images (Kim et al., 2008). The image on which I ran GALFIT was a square region of the original image centred on the object of interest with a size, which is proportional to the galaxy I wanted to fit in order to accommodate a reasonable amount of sky area (at least 50% of the total region) so that GALFIT can fit the sky emission with a realistic value. Whenever this was not possible (object too close to the edge of the frame), the section was shifted to attain the same size while still containing the object. For compatibility, I also performed a change of the image units from *nanomaggies* per second (the default unit of the SDSS DR9 frames) to counts, as recommended by Peng et al. (2010). The conversion values used were the exposition time, t_{exp}, and the *nanomaggies* per count factor, F_{npc} which is expressed on the image header as the *NMGYPERCOUNT* keyword.[3]
Following a dimensional analysis it is straightforward to see that:

$$I\ [\text{counts}] = \frac{t_{\text{exp}}\ [\text{s}]}{F_{npc}\ [\text{nanomaggies counts}^{-1}]} \times I\ [\text{nanomaggies s}^{-1}]. \tag{3.9}$$

[3] `https://www.sdss3.org/dr9/algorithms/fluxcal.php#counts2mag`

The magnitude zero point, required to obtain accurate measurements of the object magnitude uses the F_{npc} factor through the equation:

$$m_{\rm ZP} = 22.5 - 2.5 \log_{10} (F_{npc}) \,. \tag{3.10}$$

This relation comes from the fact that 1 *nanomaggie* corresponds to 22.5 mag (see `http://data.sdss3.org/datamodel/glossary.html#nanomaggies`).

The sky values also important to properly take into account possible faint features of the objects was taken to have a mean value of 0 counts since the original frames are already sky subtracted. However, in order to allow for small variations of the sky, GALFIT was allowed to adjust the sky as a free parameter as well. The plate scale of the SDSS is 0.396 arcsec/pixel (York et al., 2000). As a final global parameter I chose the convolution box to be of the same size as the input image.

3.2.1.1. PSF FILES

The input PSF I used to perform convolution with a given model so that it can be compared to the original image was that provided from the SDSS pipeline and stored in the *psField* tables. To reconstruct the PSF image from the table I followed the instructions given on the SDSS DR9 website: `http://www.sdss3.org/dr9/algorithms/read_psf.php`. Using the given tables one can compute the PSF as a function of the position in the CCD and I used a PSF centre matching the object centre in each case. For each given PSF I checked the *status* and *psp_status* values of the header and no bad flags were encountered for all the 198 images. Further details on the algorithm, based on a Karhunen-Loève transform, used in the PSF estimation can be consulted in Lupton et al. (2001).

For a sub sample of galaxies it was also used a PSF built with the IRAF[4](Tody, 1986, 1993) DAOPHOT package run in semi interactive mode and using stars from the original tile image on which the galaxy was placed to check whether the retrieved results were strongly PSF dependent or not. Testing the sub sample of models using different PSF for running GALFIT (the one provided by the SDSS pipeline and the one built with the IRAF/DAOPHOT package) I find that even though there might be a visual improvement of the residuals and some changes in the recovered parameters the difference is never strong enough to cause an object to move from one class to another. This means that in any of the tested cases, using a different PSF would not allow one to fit an additional/different component thus reassuring me that the PSF differences are small and if no host galaxy emission is detected that is not because of the used PSF. So, I am confident that the results of this report are robust against PSF variability.

When considering the HST image analysis, synthetic PSFs were computed using the TinyTim (Krist et al., 2011)[5] software as there are no non-saturated isolated stars on the small fields of the images capable of providing an empirical PSF.

3.2.1.2. MASK FILES

Whenever necessary (mainly due to the presence of saturated sources nearby) a pixel mask was applied, preventing GALFIT to take into account bad pixels when estimating the residuals after model subtraction. The mask files are simple text files with two columns, the x and y position of the bad pixels. In order to construct a mask for an extended region of the image I used combined capabilities of *ds9* [6] tools to draw the regions to be masked directly on top of the image with

[4] `http://iraf.noao.edu/`
[5] `http://www.stsci.edu/hst/observatory/focus/TinyTim`
[6] `http://hea-www.harvard.edu/RD/ds9/site/Home.html`

two simple programs (*ds9poly* and *fillpoly*) written by Chien Peng and kindly provided in the GALFIT website.

3.2.2. RUNNING GALFIT

After preparing all the files, I ran GALFIT for all the images firstly using a single model and then, whenever the residuals image of the best parameter model was not satisfactory, i.e. there were enough residuals to justify the presence of a second component. For these cases, I ran GALFIT a second time adding a Sérsic component to a single PSF/Sérsic model depending on the case.

There were also cases where the convergence of the model was not achieved for a single run. In these cases, some parameters were fixed, namely the effective radius and/or the Sérsic index, to allow the definition of the remaining free parameters and I would then run GALFIT with all the free parameters using as the initial guess the best parameters from the first run. In this way, GALFIT would be able to accurately describe the observed light distribution in difficult cases after some iterations.

3.3. SURFACE BRIGHTNESS PROFILES AND FLUX CONTOURS

The surface brightness profiles are the 1D representation of the 2D images used to model a given galaxy (see figure 3.1.). For the purpose of this dissertation they were computed via the IRAF *ellipse* routine (stsdas - analysis - isophote package). The process of ellipse is based on the extraction of the average value of the brightness of a galaxy of several elliptical isophotes at increasing distances from its centre. For each isophotes, it is necessary to compute their shape parameters: centre, axis ratio and image orientation. The simplest way is to consider that all isophotes have the same shape for the entire galaxy. In such a case, one considers an annulus with semi-major axis a whose centre coincides with that of the object. The ellipse orientation is that of the outer regions of the galaxy since they are the ones that define the overall shape of the object. Then, one selects all the pixel values within that region of a pre-defined width, sums them and divides it by the area of the ring (approximated by the number of pixels pertaining to that region)

$$I(r_i) = \sum_j G(r_j), \quad \text{if} \quad r_i - \Delta r < r_j < r_i + \Delta r, \tag{3.11}$$

where r_j is the distance of the pixel to the centre. The value that defines the width of the annulus is defined by Δr. This value should not be so large that one would average regions with large differences in brightness and not so small that it would encompass too little number of pixels thus increasing the influence of the noise on the measurements. This process has been optimized by Busko (1996) following the method proposed by Jedrzejewski (1987) and incorporated in IRAF to be widely used by the community.

The general procedure I followed was to run *ellipse* for the image section around the object and then individually for each of the models from GALFIT. The model images are obtained by running GALFIT with the option "-o3" using the output file with the final parameters. The conversion of flux units to mag arcsec^{-2} is performed via the evaluation of the Flux per unit area per unit time:

$$SB = \frac{I}{A}, \quad A = (s[\text{arcsec/pixel}] \times 1\ [\text{pixel}])^2 \tag{3.12}$$

where s is the plate scale of the SDSS. And, then by converting fluxes to magnitudes through the equation 6 of Peng et al. (2010)

$$m = -2.5 \log_{10} \left(\frac{I}{t_{\rm exp}} \right) + m_{\rm ZP}, \tag{3.13}$$

which finally results in the computation of the surface brightness profile in units of mag arcsec^{-2}

$$\mu(r) = -2.5 \log_{10} \left(\frac{I(r)}{s^2 t_{\rm exp}} \right) + m_{\rm ZP}. \tag{3.14}$$

The reported error bars of the measured fluxes were computed as a sum of two sources of uncertainties. The intrinsic variation of the flux (1σ) within a given isophote, which is provided by the *ellipse* routine, $\Delta I_{\rm ell}$, and the noise induced error here computed via an approximation to the signal to noise ratio using the statistical properties of the Poisson distribution that is characteristic of imaging data:

$$\Delta I_{SN} = \frac{1}{S/N} \quad \text{where} \quad \frac{S}{N} \approx \frac{I}{\sqrt{I + \sigma_{\rm sky}}}, \tag{3.15}$$

where $\sigma_{\rm sky}$ is the standard deviation of the background. The σ value is calculated approximately using the object subtracted image, as outputted by SExtractor, of the entire field image. The value obtained is consistent with the internally computed value by GALFIT for each image. The total uncertainty on the flux measurement will then be just the sum of the two sources of uncertainties $\Delta I = \Delta I_{\rm ell} + \Delta I_{SN}$. Then, since the uncertainties are provided in units of flux and not in units of mag arcsec^{-2} we have to propagate the uncertainties using

$$\Delta\mu = \left| \frac{\partial \mu}{\partial I} \right| \Delta I = \left| -\frac{2.5}{\ln(10)} \frac{1/(s^2 t_{\rm exp})}{I/(s^2 t_{\rm exp})} \right| \Delta I = \frac{2.5}{\ln 10} \times \left(\frac{\Delta I}{I} \right). \tag{3.16}$$

The total uncertainty is then given by

$$\Delta\mu = \frac{2.5}{\ln 10} \times \left(\frac{\Delta I_{\rm ell} + \Delta I_{SN}}{I} \right). \tag{3.17}$$

Additionally, a threshold was also marked as the surface brightness at which the background noise dominates at 1σ level. In other terms is just a transposition of the $\sigma_{\rm sky}$ value of the field onto its corresponding surface brightness limit through (see equation 8 of Kelvin et al. 2012)

$$\mu_{\rm thresh} = m_{\rm ZP} - 2.5 \log_{10}(\sigma). \tag{3.18}$$

The isophotal contours were obtained with the IRAF *contour* routine (plot package). The contours were plotted for the central region of the GALFIT fitted region and five levels are plotted. To exclude the contamination of the low-level contours from the sky level noise, a minimum threshold (around three times the standard deviation above the sky) for the contour levels was forced in the routine.

This page intentionally contains only this sentence.

CHAPTER 4

GAIA INSTRUMENT AND BASIC IMAGE SIMULATOR

"There is this person, in my head. She is brilliant. Capable. She (...) can run a code without freaking out. (...) She is me, only so much better. And I am afraid I will never become this person in my head, because something keeps getting in my way."

- The Becoming; Grey's Anatomy

Contents

The specific characteristics of the Gaia mission described in Chapter 1 are unique and will affect the way image data will be retrieved. To assess the impact of mission observations, one can in principle devise a set of simulation procedures that allow scientists to explore the wealth of targets that will be observed. Huge efforts have been made to make this happen with the creation of the Gaia simulator (or GaiaSimu library) (Robin & Reylé, 2011; Robin et al., 2012) which includes the *Gaia Instrument and Basic Image Simulator* (GIBIS, Babusiaux, 2005; Babusiaux et al., 2011). GIBIS is planned to simulate all the different sky configurations that Gaia will observe. Due to the particularities of this mission, if one wishes to study extended objects in more detail, it is necessary to process the data further in order to obtain meaningful quantities. Reconstruction methods are among the additional steps required and have been evolving, but still produce artefacts in the recovered image (Dollet et al., 2005; Harrison, 2011, and references therein). More recently, these efforts have been pushed harder to use the reconstructed images as a step to characterize the observed objects (Krone-Martins, 2011; Krone-Martins et al., 2013; de Souza et al., 2014). In this Chapter I will describe the foundations of the methods of image reconstruction associated with the Gaia mission. Then, I will present my own method designed for the specific task of retrieving structural parameters (as in GALFIT case) from Gaia simulated data.

4.1. IMAGE RECONSTRUCTION

One option to be considered in order to reconstruct 2D images from multiple observations along different directions compiled in 1D data is to use a mathematical tool developed by Radon (1917) which was named after him as the Radon transform. This operation is defined as the line integral of all possible straight lines L of a given bi-dimensional and continuous function.

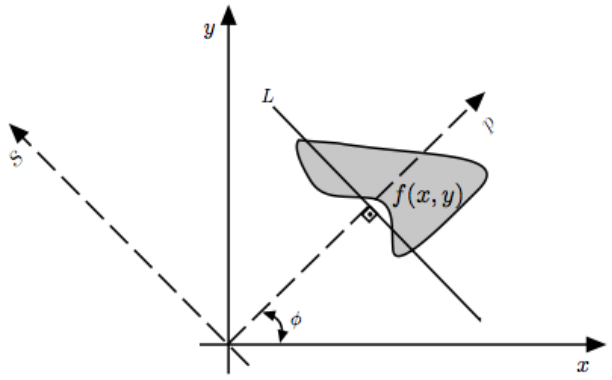

Figure 4.1. Scheme of the Radon transform. From Krone-Martins (2011).

From figure 4.1. it is possible to understand what are the variables involved in the computation of this particular mathematical transform. In Radon space, with coordinates (p, θ) we have that for each set of values the corresponding line integral of $f(x, y)$ over L which is defined as the straight line perpendicular to the direction defined by the angle θ at a distance p from the point of reference. On the SP reference system, we can write the relations between the two set of coordinates using the rotation matrix around the z-axis of an angle ϕ:

$$\begin{pmatrix} x \\ y \end{pmatrix} = \begin{pmatrix} \cos\phi & -\sin\phi \\ \sin\phi & \cos\phi \end{pmatrix} \begin{pmatrix} p \\ s \end{pmatrix} \Rightarrow \begin{cases} x = p\cos\phi - s\sin\phi \\ y = p\sin\phi + s\cos\phi \end{cases} \tag{4.1}$$

which allows us to write the functional form of the Radon transform of $f(x, y)$ as the equation (I) of Radon (1917)

$$\breve{f}(p, \phi) = \int_{-\infty}^{+\infty} f(p\cos\phi - s\sin\phi, p\sin\phi + s\cos\phi)ds. \tag{4.2}$$

Whenever possible to obtain the analytical form of $\breve{f}$ we have then access to its value in whatever pair of (p, ϕ) that we might choose enabling us to sample every point of the Radon transform of the original function. Nevertheless, as in most cases it is not possible to obtain such an expression, we only have access to the value of the mathematical transform in a finite set of coordinates in Radon space. We call the graphical representation of the set of coordinates available a senogram. In practice, the construction of a senogram is processed as follows.

Consider a matrix A, with M×N dimensions, which is the mathematical representation of a given image, in that sense, M and N are the number of rows and columns of the image. Imagine also a second matrix S, with P×R dimensions. Now, P is the number of desired angle projections that one is aiming to obtain and R is the smallest integer number greater that $\sqrt{\mathrm{M}^2 + \mathrm{N}^2}$. In this scenario, the senogram of the image A is the matrix S where in each line s we have the one-dimensional collapse (sum over all the elements along the horizontal direction) of the image A rotated by the angle θ. To do that, an intermediate matrix T is necessary to be constructed. This has the size t that encompasses the rotated image (from simple trigonometric relations, $t = \mathrm{M}\cos\theta + \mathrm{N}\sin\theta$) and is represented schematically in figure 4.2.. The matrix T is nothing more than the concretization of a rotated figure on a square, horizontal grid which will be zero in all points where there is no overlap with the image, and the corresponding interpolated value for the pixels that do overlap. Then, each element (p, θ) of S is given by

$$S_{p,\theta} = \sum_{j=0}^{t} T(\theta)_{p,j}. \tag{4.3}$$

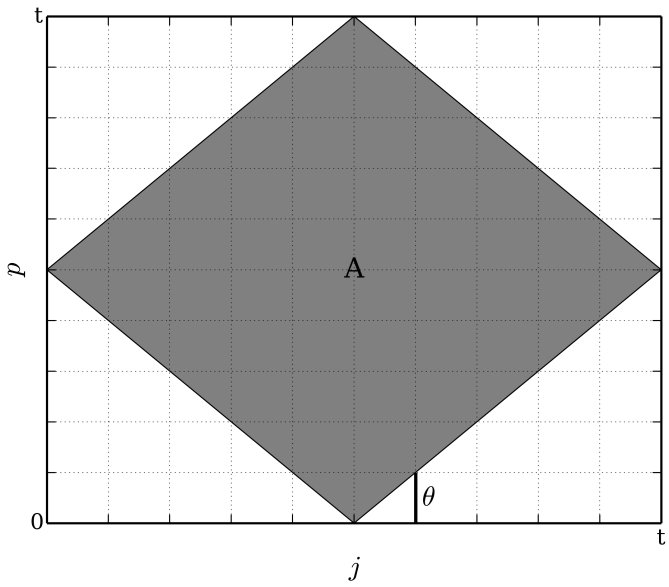

Figure 4.2. Schematic representation of image rotation for the matrix A by an angle $\theta = 45°$.

In the case of Gaia observations, we have the possibility of reconstructing the 2D image by the inverse Radon transform of the set of available directions observed since each observation along a great circle corresponds to a line in the Radon space (p, ϕ) where p represents the position along the CCD motion where the galaxy is observed and ϕ is the angle of the great circle with respect to a given reference system. However, as proven by Smith et al. (1977), any unambiguous reconstruction of a 2D signal requires an infinite number of projections. This means that any finite set of observed projections will translate into an approximation of the original image. The quality of this approximation is increasingly worse for a decreasing number of available projections as illustrated in figure 4.3.. This example takes the simple example of two Gaussian signals in ideal conditions (no noise, no CCD effects) and shows the 2D reconstruction using a set of linearly spaced N projections between 0 and π.

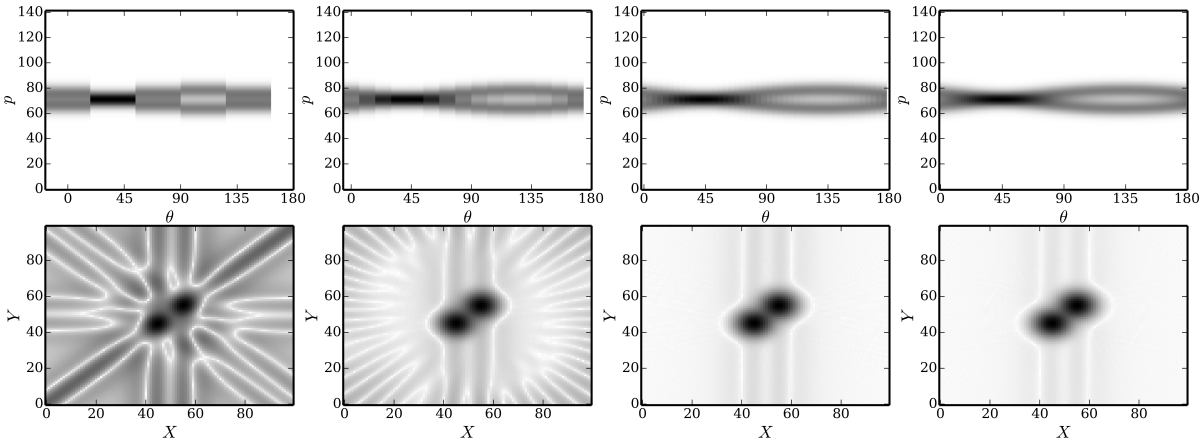

Figure 4.3. Image reconstruction as a function of the number of available projections for an image with two Gaussian peaks. The top panel is the senogram of the original image and the bottom panel is the reconstructed 2D image. From left to right the number of projection angles is 5, 15, 40 and 90 linearly spaced between 0 and π.

As there are already several reconstruction algorithms I will refer to them briefly in this next few lines. Harrison (2011) has implemented four methods to achieve the final goal of reconstruction of images in the context of the Gaia mission. The first, *QuickStack*, consists in simply computing the Radon transform of the observed windows and then stacking them together. This means, that, each pixel of the reconstructed image will be composed of a mean value of all the windows that have observed in that position. As an improvement to this method, the *ShuffleStack* gives the pixel with more observations a greater weight. This means that it starts by the pixel to which contribute the highest number of stacked observations, compute the mean observed value in that position, and then subtracts that means to all the windows values that contributed to that pixel. This process is repeated until all the image is reconstructed. The third method, *Drizzle*, evaluates the windows on a grid with a finer resolution. In this new grid, each pixel will have the value corresponding to a fraction of the observed value. This fraction is nothing more than the fraction of the area of the intersection between the grid and the window value. The last one described here is the *BinOutliers* method. This method is aimed to minimize the obfuscation of the brighter regions of the image which are observed more times and might affect the reconstruction of the outer regions. It is also a pixel by pixel reconstruction (without a preferred order) that takes the mean and the standard deviation of the 70% less bright values that contribute to one pixel to remove outliers that are k times departed from the mean value (k is a free parameter that can be adjusted to any particular problem) to contribute to that pixel reconstructed value. There are, of course, other methods, more complex in nature, but with better results that are not described here. I refer the reader to Krone-Martins (2011, chapter 2) to a more detailed description of all the mentioned above and for the reference of others.

However, there are several issues that greatly affect the reconstruction process. The first is related to the diverse window sizes and sampling factors that are used in the on-board processing of the Gaia satellite (see 1.1.). Therefore, the proposed algorithm should be able to process these different sizes and resolutions to combine all the observed data for a single source. The square shape of the mirrors will result on a PSF that is not circularly symmetric and position dependent. Noise from the CCD reading process and temporal variations of the instruments will further complicate the problem at hand. For that reason, image reconstruction might not be the best approach for the morphological analysis of galaxies which largely relies on how the light is distributed on the image. Krone-Martins (2011) proposes a forward modelling approach where one converts the model images (which are generated in perfect conditions) back into the Gaia observed frame to compare them directly to the data that were obtained (Krone-Martins et al., 2013). A *toy model* explaining this process is described carefully in the next section.

4.2. SETTING UP A *TOY MODEL*

Although possible, reconstruction of bi-dimensional images is not a simple process especially when considering all the inherent problems associated with the obtainment of astronomical images as stated in the previous section. In addition, trying to conduct morphological studies, such as running GALFIT for surface brightness profile decomposition, does not allow for an accurate estimation of the morphological parameters (see Krone-Martins, 2011; Krone-Martins et al., 2013). With that in mind, a forward modelling approach was developed to compare the data to the models in Radon space instead of the real space. The idea behind the method to derive the galaxy structural parameters from Gaia data is as follows (following the work of Krone-Martins 2011):

1. Create a model galaxy based on a set of parameters using GALFIT convolved with a Gaussian PSF with a given Full Width at Half Maximum (FWHM);
2. By choosing an appropriate window, simulate the observed Gaia data as extracted from the model galaxy via Radon transform of the model;

3. Compute the residuals (i.e. the difference between the galaxy model data and the real data) for this set of parameters;
4. Iterate over the galaxy parameters until a minimum of the residuals is found (this is done using a *Levenberg-Marquardt* algorithm implemented in the *leastsq* function of the python package *scipy.optimize* v0.12.0).

The first step to perform this method consists on creating a model galaxy based on the set of morphological parameters. This is performed via GALFIT which allows to create an image of a model galaxy based on a given set of parameters. For the purpose of this part of the report, only *exponential disc* profiles and *de Vaucouleurs* profiles are used in generating galactic models. All models are convolved within the software with a given PSF. Again, for the purpose of this work, a Gaussian model is previously generated through the same software with a given FWHM and then the resulting model is used as the PSF for the convolution of the galaxy model. An example can be seen in figure (4.4.). Since GALFIT works with total magnitudes it is required to know the conversion between these values and the intensity parameter from equation 3.8, I_e. First, we have to compute the total flux of the model, which is done via the inverse of equation 3.13)

$$F_{\text{tot}} = t_{exp} 10^{0.4\times(m_{\text{tot}} - m_{\text{ZP}})}, \tag{4.4}$$

where m_{ZP} is the magnitude zero point (defined as $m_{\text{ZP}} = 25.68$ as used in GIBIS simulations) and t_{exp} is the exposure time that is one second by default. Then, using the values of the bulge-to-total ratio (B/T) which is defined as the ratio between the light from the bulge to the light form the entire galaxy

$$\frac{B}{T} \equiv \frac{F_{\text{bulge}}}{F_{\text{tot}}} = \frac{F_{\text{bulge}}}{F_{\text{bulge}} + F_{\text{disc}}}, \tag{4.5}$$

we can then define the bulge and disc flux as

$$F_{\text{bulge}} = \left(\frac{B}{T}\right) F_{\text{tot}}, \quad F_{\text{disc}} = \left(1 - \frac{B}{T}\right) F_{\text{tot}}. \tag{4.6}$$

With these separate definitions of the flux of the two separate components we can now compute the disc and bulge intensities as follows:

$$I_d = \Sigma_0 = \frac{F_{\text{disc}}}{2\pi r_d^2 q} \tag{4.7}$$

is the disc intensity, where $q = b/a$ and r_d is the disc scale length sometimes represented by r_s (Peng et al., 2010, equation 9) and also adapted from Peng et al. (2010, equation 4)

$$I_b = \Sigma_e = \frac{F_{\text{bulge}}}{2\pi r_e^2 q K}, \text{ with } K = e^{\kappa} n \kappa^{-2n} \Gamma(2n), \tag{4.8}$$

is the bulge intensity, where n is the Sérsic index, κ is the exponential factor on the Sérsic law (which is $\kappa = 7.67$ for $n = 4$) and $\Gamma(2n)$ is the gamma function evaluated at $2n$. As we are interested in the *de Vaucouleurs* case, we get $K \approx 3.607$. We can also define the bulge and disc magnitudes, required to simulate a galaxy via GALFIT, from equation 3.13 applied to each of the components

$$m_{\text{disc}} = -2.5 \log_{10}\left(\frac{F_{\text{disc}}}{t_{exp}}\right) + m_{\text{ZP}} \quad \text{and} \quad m_{\text{bulge}} = -2.5 \log_{10}\left(\frac{F_{\text{bulge}}}{t_{exp}}\right) + m_{\text{ZP}} \tag{4.9}$$

which, for the case presented in figure 4.4. is: $m_{\text{disc}} \approx 14.75$ and $m_{\text{bulge}} \approx 16.75$.

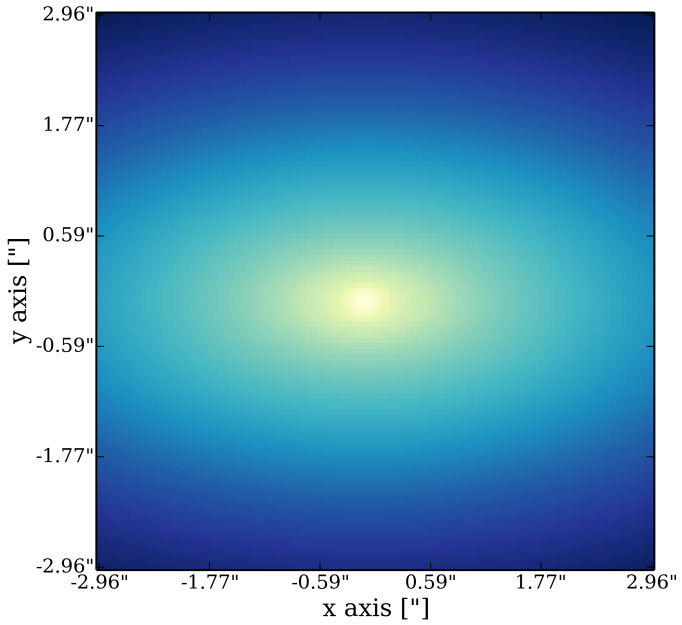

Figure 4.4. Galaxy model generated with GALFIT convolved with a Gaussian with $FWHM = 180$ mas with total magnitude, $m = 15$, $B/T = 0.5$, $r_d = 600$ mas, $r_b = 200$ mas and $b/a = 0.5$.

The next step requires the re-sampling of the observed image on a matrix of rectangular pixel to mimic the CCD conditions on-board Gaia telescopes. From the introduction section we saw that the pixel angular size is 59×177 mas which translates in a ratio of $177/59 = 3$. Thus, it is necessary to replace on a given direction every three consecutive pixel by the sum of those three pixels. This re-sampling is displayed on a two step base in figure 4.5. where it can be observed the loss of resolution in the vertical direction (top right panel) that will translate on an apparent change in the galaxy orientation when we re-sample the galaxy on a new square pixel matrix (bottom panel). This apparent change is just the consequence of the flattening of the image by a factor of three in the vertical direction.

After obtaining the re-sampled model it is necessary to perform a Radon transform of the image for a finite number of observed angles. To do so, it is performed a Radon transform for a given list of defined projections. The number of desired angles depends on the desired resolution in Radon space bearing in mind that the computing time increases with the number of defined projections. Once the senogram is built it is required to select the angles from which the actual galaxy was observed. It is important to note here that prior to the Radon transform of the model all values of the pixel with distances to the centre greater than the maximum size of the transmitted windows ($\approx 2''$) are set to zero since they are not taken into account during the actual observations.

After the Radon transform and posterior angle selection, the next step consists on extracting the senogram regions corresponding to the CCD columns that one wants to consider (this approximation is valid for galaxies smaller than the AC column width, Krone-Martins 2011). For instance, using as model the galaxy from figure 4.4. we have a transmitted window from the AF1 columns with 12×1 values for each projection which corresponds to selecting the central 12 pixel ($0.71''$), six from each side, from the senogram. In a similar way we can obtain the same regions for the other CCD columns considering their own specifications seen in table 1.1. and the magnitude of the object. Note that when the transmitted window is already bi-dimensional each transmitted line has its own senogram from which the information is extracted. In the special case of SM columns, it is also necessary to integrate along the CCD motion direction by a factor

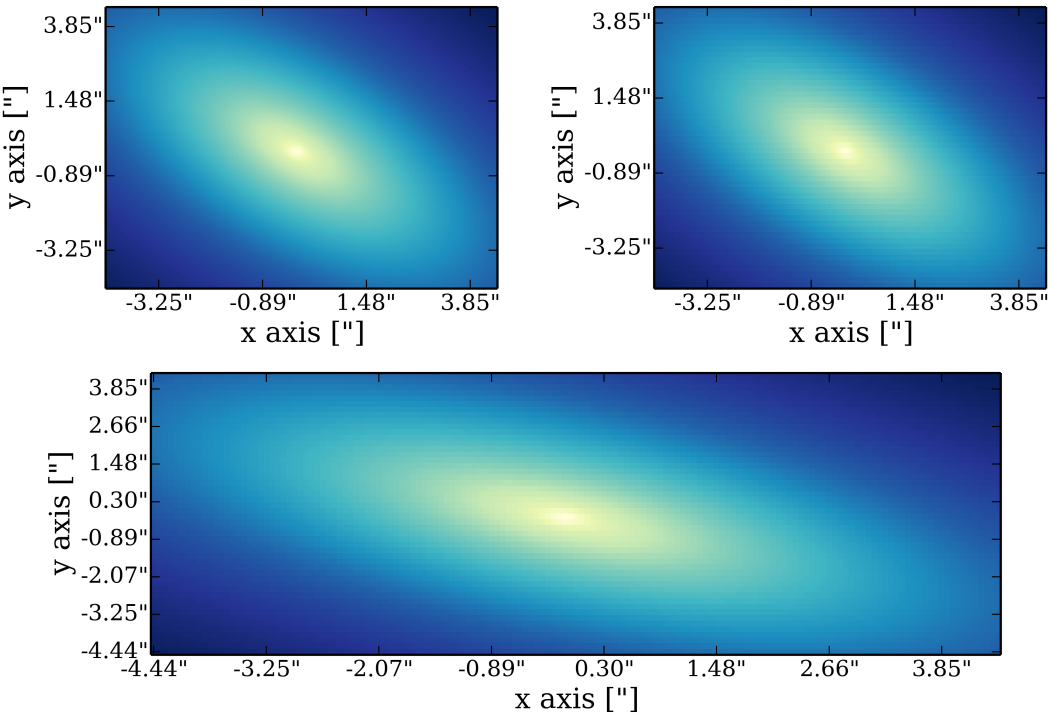

Figure 4.5. Top left: Same as figure 4.4. with a 45° rotation. Top right: Binning along the vertical direction to mimic the rectangular shape of Gaia CCDs pixel. Bottom: Re-sampling in square pixel of the same galaxy now binned in the vertical direction.

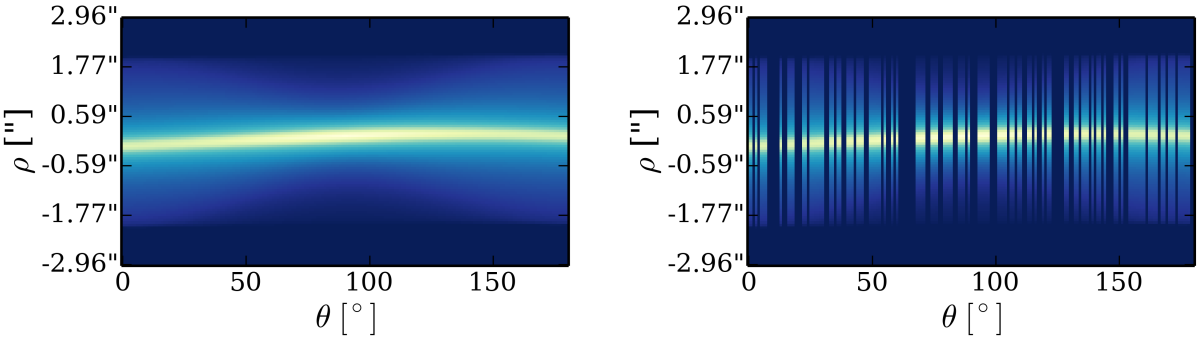

Figure 4.6. Left: senogram with 181 linearly spaced angles between zero e π of the galaxy of figure 4.4.. Right: the same image as the left panel, but with a mask applied to select the observed angles (for visualization purposes this corresponds to a random sub-sample of the 181 angles).

of two or four according to the object magnitude being brighter or fainter than 13 respectively. We can see an illustration of this step in figure 4.7. where one can see the different regions of interest for each of the simulated column for a given number of projections.

With these simulated images for each CCD column one is finally in conditions to compare with the actual observations of a given object. To do so, we compute the residual image, which is simply a pixel by pixel subtraction that will be used in the least square minimization *leastsq* function of the python package *scipy.optimize* v0.12.0. This minimization process can be conducted on single columns or using any combination of the existing columns one may want to simulate simultaneously. Depending on the science case it may be more useful to use the extended low resolution simulations of the SM columns or the more compact, but higher resolution data of the

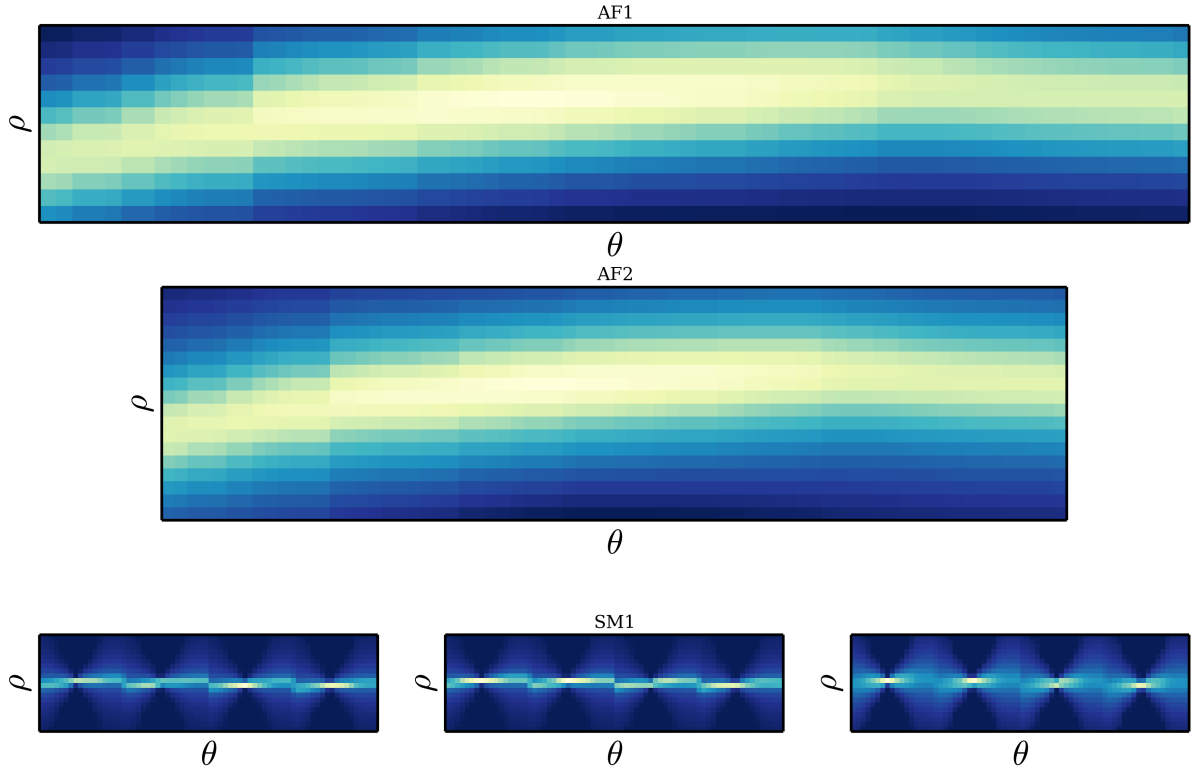

Figure 4.7. Simulated images of the galaxy from figure 4.4. for three CCD columns. There are 70 vertical lines, each of which represents a single extracted projection of 12, 18 and 20 samples (AF1, AF2 and SM1 respectively).

AF columns.

4.3. MORPHOLOGICAL PARAMETERS ESTIMATION

In order to test whether the proposed algorithm is able to retrieve reasonably the structural parameters of galaxies when observed through the simulated Gaia data it is necessary to establish a simulation protocol on a sample of ideal simulated galaxies for which we know the true set of parameters.

If one wants the simulations to be realistic it is necessary to take the images through a series of processing steps related to characteristics of the observations. So, in addition to all the steps mentioned in the previous section it is required to include additional image processing procedures. One of the fundamental mechanisms that take place whenever one wishes to obtain astronomical images is the fact that a CCD measures the number of photons that hit it from a given sky direction. Thus, an image is just a discrete matrix of integers which express the number of detected photons at each pixel position. In probabilistic terms there is a statistical distribution, the Poisson distribution (named after the French mathematician Siméon Denis Poisson), which describes the probability of detect a certain number of events during a given time interval and its functional form is (see for example section 3-9 Montgomery & Runger 2010)

$$P(X = k) = \frac{\lambda^k e^{\lambda}}{k!}, \tag{4.10}$$

that gives the probability of having k events during a certain time interval whose expected value to be observed is equal to λ. In this sense, for a realistic simulated image of the surface brightness profile of a galaxy it is necessary to re-sample the theoretical profile such that each matrix

entry is an integer value. To do so, one replaces each pixel value for a random value taken from a poissonian distribution where λ is the original pixel value. This process degrades the signal especially on the fainter regions of the profile where the probability of detecting one photon is very low. In figure 4.8. one may inspect the result of poissonian re-sampling for the same galaxy that has been taken as an example. Generally one gets the same brightness distribution although less smooth.

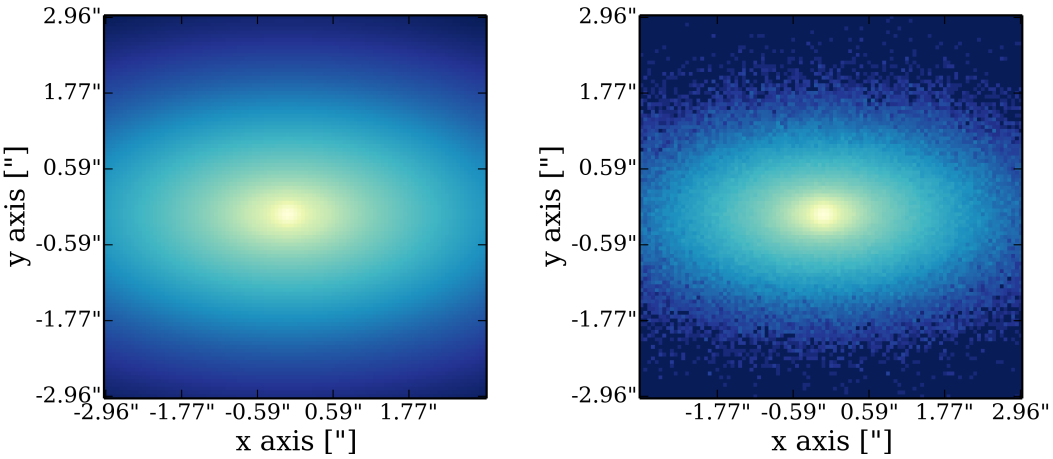

Figure 4.8. Analytical model of the same galaxy of figure 4.4. on a logarithmic scale (left) and one example of poissonian re-sampling (right).

It is on this re-sampled image that the whole process from real space to Radon space is applied. Yet, an additional source of noise is still required. This noise component is that related to the reading process of the CCD by the telescope instruments. This new noise image is added as an image of the same dimension of the column simulated data with every pixel value taken from a Gaussian/Normal distribution (see for example section 4-6 Montgomery & Runger 2010)

$$P(X = x) = \frac{e^{-x^2/2\sigma^2}}{\sigma\sqrt{2\pi}}, \tag{4.11}$$

centred in zero and with a given σ width. In the particular case of this simulation the value of σ is around 20% the mean value of a galaxy with magnitude $G = 20$. The final simulated galaxy is just the sum of this noise matrix with the column simulated image after the poissonian re-sampling.

After applying the noise modifications to the toy model process, one is ready to proceed to numerical simulations to test the retrievability of morphological structural parameters for which we know the answer *a priori*. The description of the simulation sets up and all the related results can be found in the next Chapter.

This page intentionally contains only this sentence.

CHAPTER 5

RESULTS

"I had this memory game when I was a kid. A bunch of cards, face down, in rows. Each card has a picture. You turn one over, look at it, then turn it back over. Then you have to try and remember where its matching card was. Sometimes you have no idea. And other times it shows us exactly what we need to see. The cards seem completely out of order and random. But you keep turning them over... and the more cards you see, you get a sense how everything fits together."

- Remember The Time; Grey's Anatomy

Contents

This chapter presents the main results of this project separated in three subsections. The first subsection contains the morphological study of the optical counterparts of ICRF2+ sources. The second reports on the morphological characterization of the optically passive elliptical radio galaxies sample. The third part concerns the test on the recuperation of these morphological information from Gaia simulated data and the results for a case study of simulated galaxies using GIBIS and posterior application of the developed method to retrieve the structural information.

Additional information pertaining to the sources of the scrutinized sample were retrieved from the SDSS database (source magnitudes in the r-band) and from the NED[1] database (source redshifts).

5.1. ICRF2+

Before proceeding with the analysis presented in chapter 3, a basic test was performed to assess the compactness of the sources. This test is based on a comparison between the flux on the wings of the object as compared to the central region of the profile. The resulting statistic, based on an inner circular aperture of 3" and an outer aperture of 8" is defined as:

$$F_{\rm gal} = \frac{F(< 3") - F(< 8")}{F(< 3")} \tag{5.1}$$

The results of this simple test may be found in figure 5.1.. For 183 sources ($\sim 92\%$) the light in the outer annulus is less than 50% of the central flux and there are 89 ($\sim 45\%$) for which the value of $F_{\rm gal} < 0.25$.

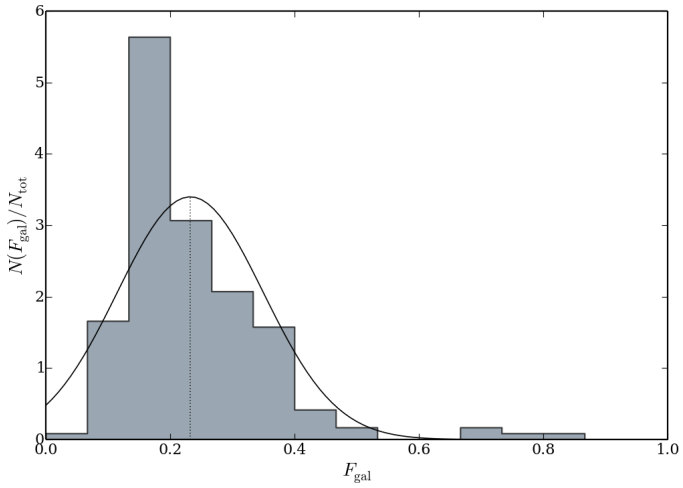

Figure 5.1. Flux ratios of the sources: wings in comparison to the central region.

While indicating that there are a great majority of sources with little flux in the outer wings, a more detailed analysis of their morphological structure must be performed to correctly assess the compactness of each object. Following the procedure presented in Chapter 3 I obtained the results for the 2D decomposition of surface brightness profiles which are summarized in table 7.3. of the Appendix.

After analysis of the residuals and of the best-fit parameters of the sources, and some refinement of the sample to exclude saturated sources or non-detections in the SDSS (16 sources), I arrived at a final classification scheme divided in three morphological classes: 134 sources were best modelled with a single PSF component; 32 sources were fitted using a single Sérsic component and 16 sources with a combination of those models (PSF+Sérsic profile) as can be seen in greater detail in table 5.1. where the real sample of the source is also discriminated.

One can see in figure 5.2. that the retrieved total model magnitudes are highly consistent with the reported r-band magnitudes from SDSS, which is a sign that GALFIT did perform very well

[1] `http://ned.ipac.caltech.edu/`

	ICRF2	Bourda et al. (2011)	Total
PSF	86	48	134
Sérsic	21	11	32
PSF+Sérsic	6	10	16

Table 5.1. Number summary of ICRF2+ sources per parent catalogue and per morphological class.

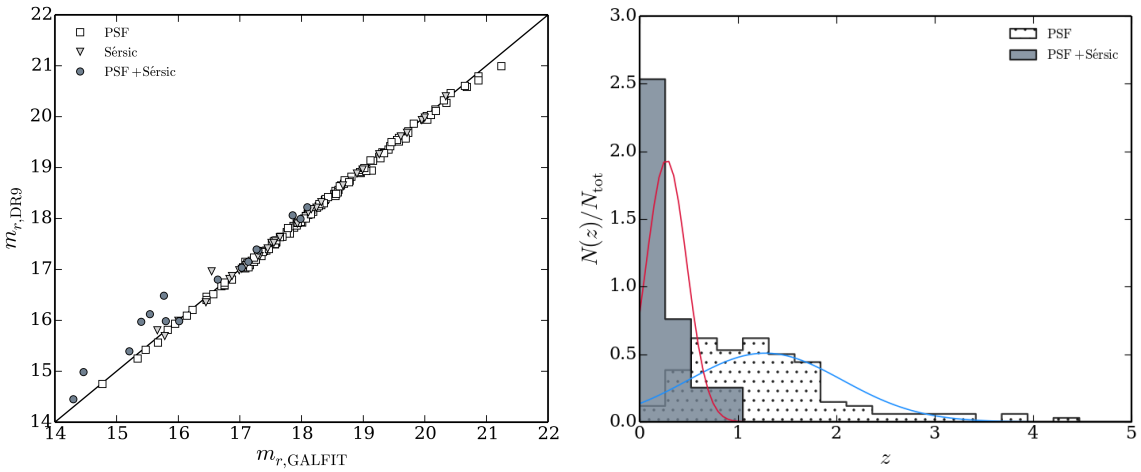

Figure 5.2. Magnitude results from GALFIT (left) and class number count normalized histogram as a function of redshift (right). The solid lines are the Gaussian fit to each histogram: PSF in blue and PSF+Sérsic in red.

on the magnitude parameter. There is, however, a slight discrepancy in the measured magnitudes in the bright end of the PSF+Extended sources in a sense that GALFIT reports brighter magnitudes than the SDSS. This might happen due to any unaccounted extended component by SDSS pipeline as it measures the flux (for point-like objects as it is the case for most of the observed quasars) considering a circular aperture centred on the object thus missing the flux from the extended wings of the host galaxy. This effect is greater when considering brighter sources ($m < 16$) as the AGN might be brighter than its host galaxy making, it is more difficult to detect any extended emission.

As for the number count of each class of objects it is obvious that the distinction between the point-like emission from the AGN and the extended emission from the host galaxy (the PSF+Extended models) decays rapidly with their distance to us. The highest redshift on which I have performed the decomposition happens for galaxy ICRF J102444.8+191220 with $z \sim 0.83$. The PSF modelled sources have a wider distribution extending greatly towards higher redshifts. Each morphological class is presented with greater detail in the following subsections.

To quantify the residuals I first defined a circular aperture based on the typical size of the sources as measured by SExtractor. The residual quantification is done using three separate quantities. The total flux of the object within that aperture compute as

$$G = \sum_{i,j} I_{i,j} \quad \text{where} \quad d_{i,j} < 2.5 \times r_{e,\mathrm{SEx}}. \tag{5.2}$$

The residual (excess or lack of) flux that is contained in the same aperture computed directly

from the image of residuals, R provided by GALFIT via

$$E = \sum_{i,j} |R_{i,j}| \quad \text{where} \quad d_{i,j} < 2.5 \times r_{e,\mathrm{SEx}}. \tag{5.3}$$

The modulus applied to the residual image is done to prevent the cancellation of an excess of light with a depression of light within the same aperture leading to a false value of $E \sim 0$. Finally, the mean sky flux for the entire stamp image is measured as the mean flux from all the pixels that are not flagged as detection in the segmentation image, S, provided by SExtractor.

$$\bar{N} = \frac{1}{n_{\mathrm{pix,s}}} \sum_{i,j} |I_{i,j}| \quad \text{where} \quad S_{i,j} = 0, \tag{5.4}$$

where $n_{\mathrm{pix,s}}$ is the number of pixels for which the segmentation image has the value zero. Since the values of G, E and N are not measured in the same apertures, there is one last step to compute the sky flux that can be related to that the measured aperture. To do so, one simply multiplies the value of the average sky flux by the number of pixels in the aperture so that $N = \bar{N} \times n_{\mathrm{pix,a}}$. Now we are in conditions to evaluate the amount of residuals present in the data by computing the ratio

$$F_{\mathrm{G}} = \frac{E - N}{G - N} \tag{5.5}$$

which relies on the global flux within the aperture. For a local measure of the residual in each pixel we can also perform a calculation of the median value of the individual pixel ratios between the galaxy and the residuals images. In that case

$$F_{\mathrm{L}} = \mathrm{median}\left(\frac{|R_{i,j}| - \bar{N}}{|I_{i,j}| - \bar{N}}\right) \tag{5.6}$$

and we can inspect the influence of local differences on the global fit.

The global results of this residual computation may be inspected closely in figure 5.3. and 5.4.. All 182 galaxies considered have residuals below 15%. Looking at the distribution one sees that the majority of sources have a very small amount of residual light after model subtraction. In fact, 177 (166) of the sources have residuals smaller than 5% and 141 (91) galaxies less than 2% of residual light. The fact that the local residuals are on average larger than the global ones is expected from the fact that pixel-to-pixel variations, which are influenced by noise, tend to raise this value whereas in the global calculation, the noise variations are averaged out in the region of interest.

In what concerns the different classes of objects (see figure 5.4.) there is not a big difference between that presented by point-like sources and compact sources. Despite for a slight tendency in the global regime that compact sources are slightly worse than point-like objects. The point-like+extended sources are all distributed at lower values than those previously mentioned. In particular, for the global residuals they are all below 2%. This is to be expected since they have one more component than the other classes making them more efficient in the subtraction of the light from the object.

5.1.1. POINT-LIKE SOURCES

The majority of the ICRF2+ sources (134 out of 198) are modelled as point-like. This means that for these objects no significant trace of the host galaxy was found underlying the AGN emission. Even when some residuals were found after the best-fit PSF subtraction those were not relevant/big enough to allow for the fitting of an additional Sérsic component which was tried

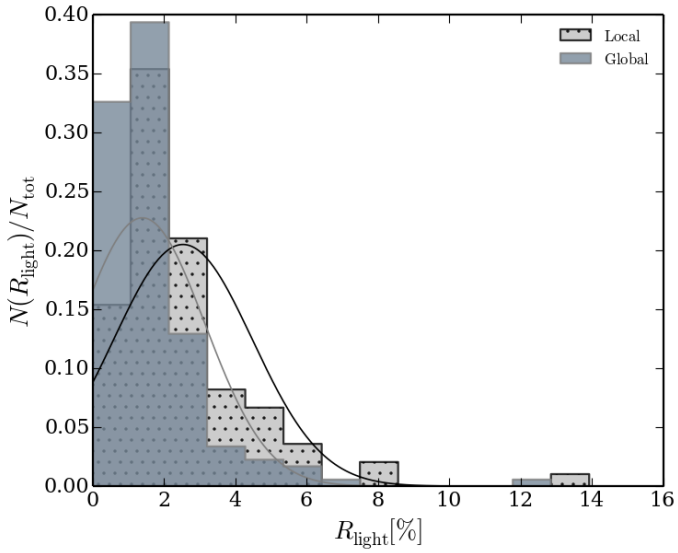

Figure 5.3. Distribution of residual light after model subtraction for two different methods. The solid lines are the Gaussian fit to each histogram: Global in grey and Local in black.

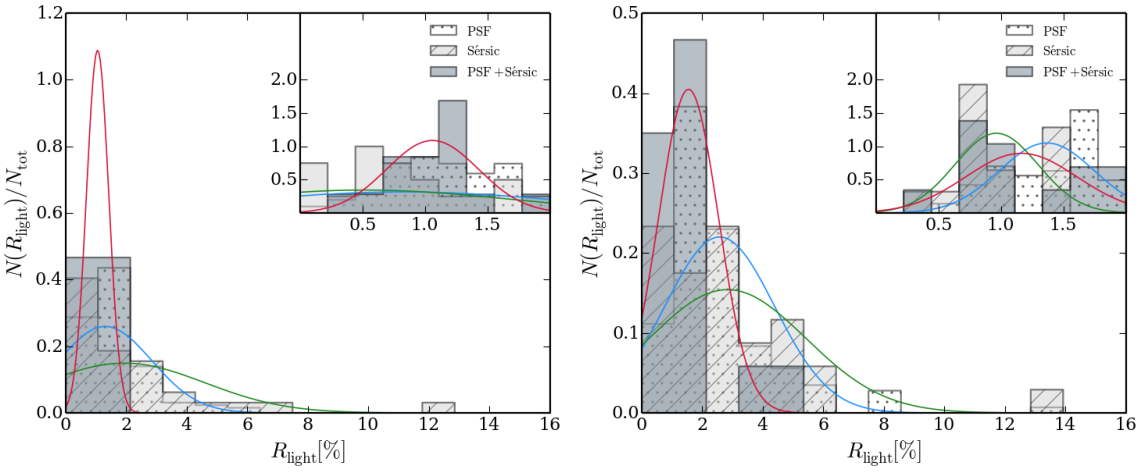

Figure 5.4. Same as figure 5.3. but with the discrimination of the morphological classes. Total (left) and local (right) residuals are displayed separately for viewing purposes. The solid lines are the Gaussian fit to each histogram: PSF in blue, Sérsic in green and PSF+Sérsic in red.

but GALFIT would always result on unreliable structural parameters (either too faint component or too small with effective radii smaller than the pixel size). An example of surface brightness profiles, GALFIT results and flux contours may be found in figure 5.5..

5.1.2. COMPACT SOURCES

For some cases (32 out of 198), the best fit model was achieved by fitting a single Sérsic profile. Among these objects there are no clear detection of an AGN component (PSF) plus an extended component (host galaxy) like in the following set of objects. This may be due to either the AGN emission being mild thus being partially diluted by the host galaxy, or alternatively, most of the observed emission is AGN related with the host emission being rather faint. In any case, further analysis (e.g. SED analysis) is required to distinguish between the proposed scenarios, but it is out of the ambit of this dissertation. Surface brightness profiles, GALFIT results and flux contours may be found in figure 5.7..

In figure 5.11. the overall properties of this sample as determined by GALFIT may be inspected. They have generally low Sérsic indexes ($n < 2$ for 30 out of the 32 objects), very small sizes ($r_e \lesssim 1$ for all cases, but one with $r_e \sim 2.9$ kpc) and an arrange of ellipticities.

5.1.3. POINT-LIKE + EXTENDED SOURCES

Finally, there are 16 out of 198 objects which are best fitted by a PSF+Sérsic model. These are the ones that have well detected emission from the host galaxy, whose light can be characterized by a Sérsic profile. Surface brightness profiles, GALFIT results and flux contours may be found in figure 5.9..

As for their structural parameters, their values and respective redshift dependence may be found in figure 5.11.. In these plots one may see that the large effective radii found (those with the largest errors) are certainly related to some ill-modelled diffuse component that increases the radius of the galaxy. Nonetheless, the large error bars still encompass the smaller radii values observed for sources where a better fit was achieved in this parameter. There is a hint for a size evolution detected for the host galaxies as higher redshift galaxies are smaller than their low redshift counterparts as expected from galaxy evolution (see for e.g. Poggianti et al., 2013, and references therein).

In what concerns the Sérsic index of these detected hosts, they show a wide distribution with no preferred number. Still, most sources (10 out of 16) have $n > 2.5$ leading to the idea that host galaxies of this sample are tendentiously more bulge-dominated than disc-dominated galaxies. As for their dependence in redshift, there is no hint for a correlation between these parameters.

Regarding the axis ratio of the galaxies, they are more round shaped in general as 14 out of 16 have values of $b/a > 0.5$. Furthermore, galaxies at lower redshifts ($z \lesssim 0.5$) appear to be more round-like ($b/a \gtrsim 0.5$) than the two galaxies found at higher redshifts ($z \gtrsim 0.5$) which appear to be more elliptical in shape ($b/a \lesssim 0.5$). Nonetheless, since there are only two objects at $z \gtrsim 0.5$, no clear evolution can be claimed to exist.

5.1.4. STRIPE 82 IMAGES ANALYSIS

The central region on the Southern Galactic Cap, the Stripe 82 (Annis et al., 2011) is a co-addition of SDSS ugriz imaging data covering 275 deg^2 centred on the celestial equator and with a declination range of $50° < \delta < 60°$. Each patch of this region has been imaged around 20 times under optimal seeing conditions allowing for detection of objects with magnitudes two times deeper than the rest of the SDSS single pass survey and reaching a 50% completeness limit for

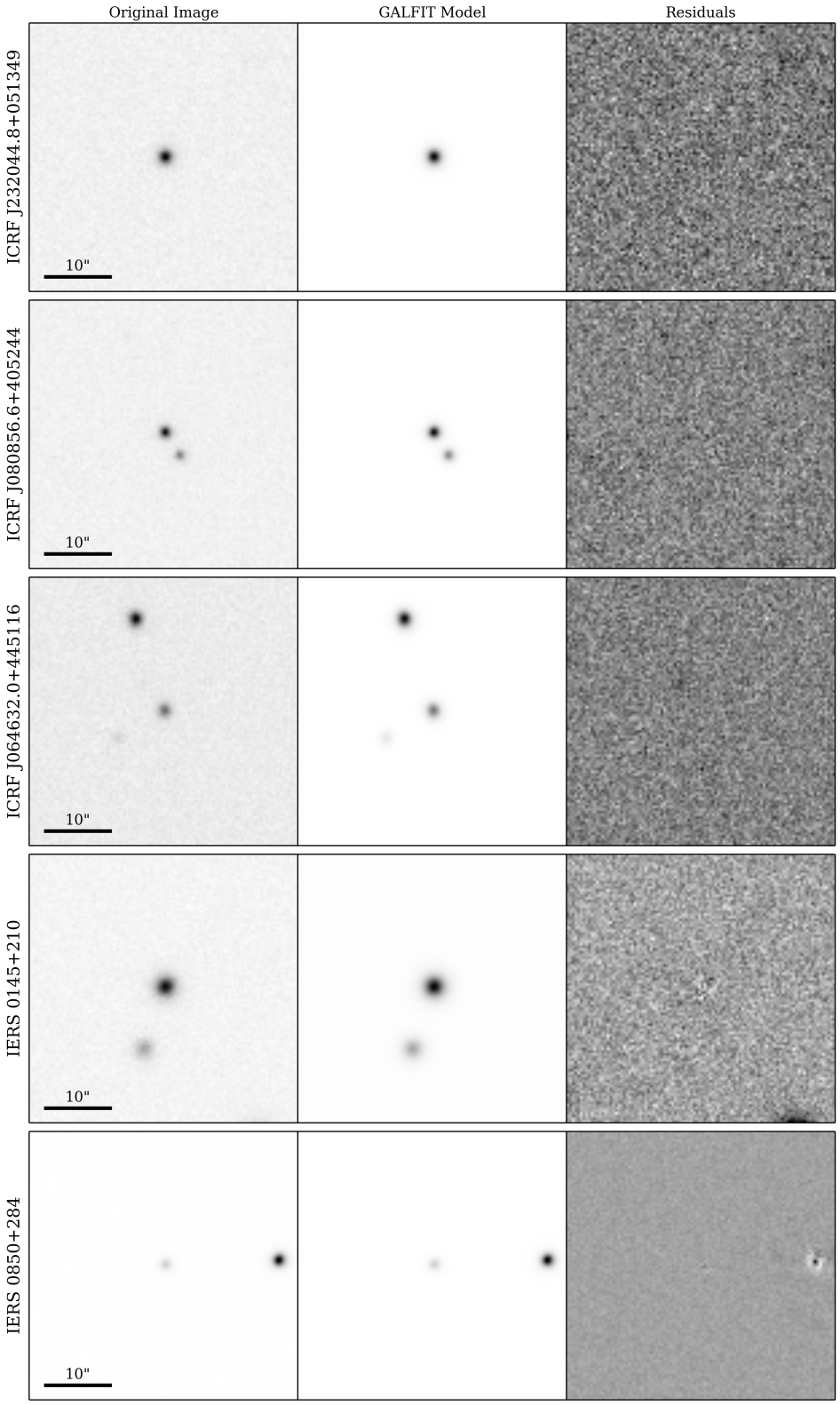

Figure 5.5. GALFIT results for ICRF2+ sources with PSF profiles. Each row represents a different source and each column represents, from left to right the input image, the best-fit model from GALFIT and the residual image (galaxy-model).

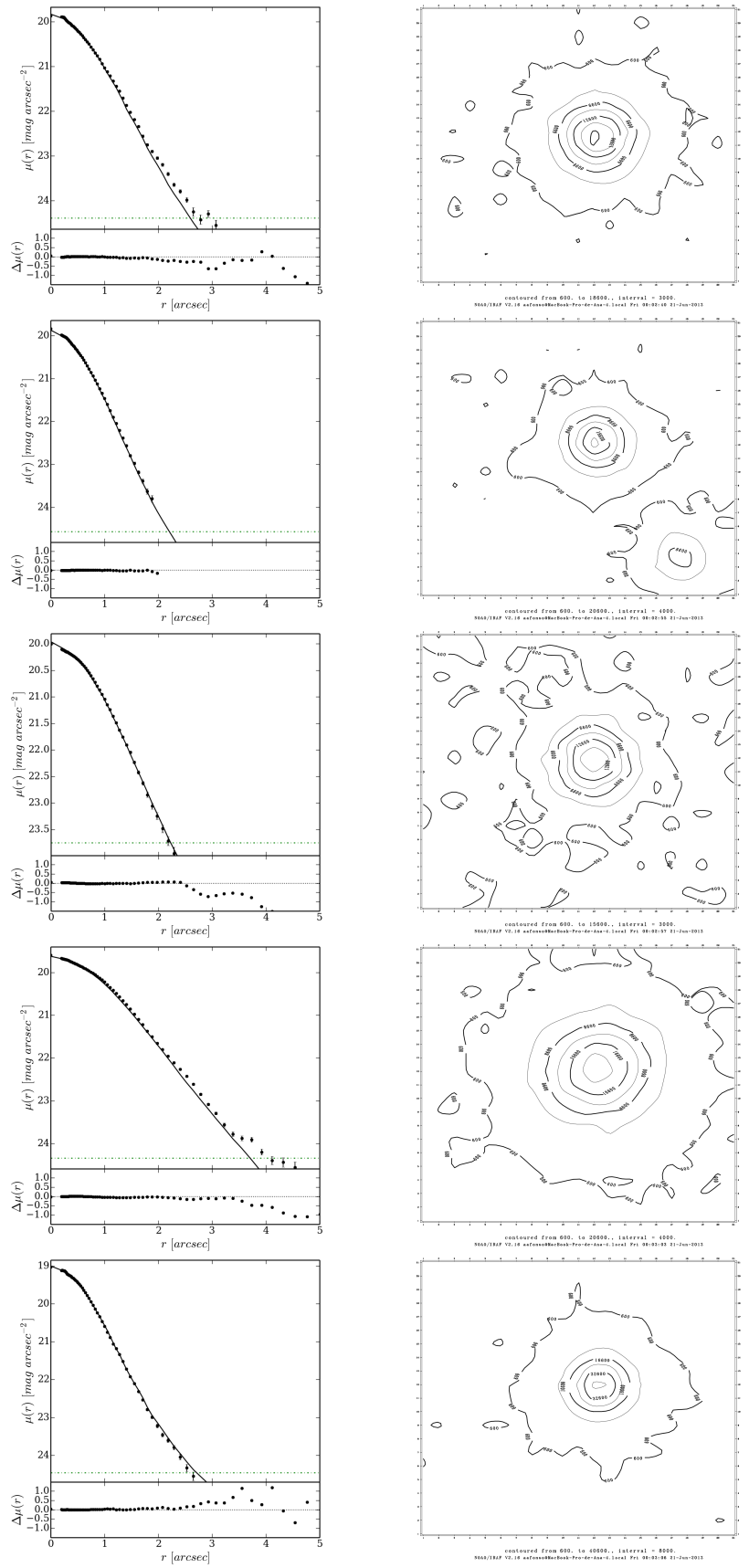

Figure 5.6. Surface brightness profiles and isophotal contours for the sources of figure 5.5.. The solid line represents the GALFIT model and the open circles with error bars the input image profile. The green dotted-dashed line represents the background noise at 1σ level. The bottom panel of each profile represents the difference between the data points and the GALFIT model.

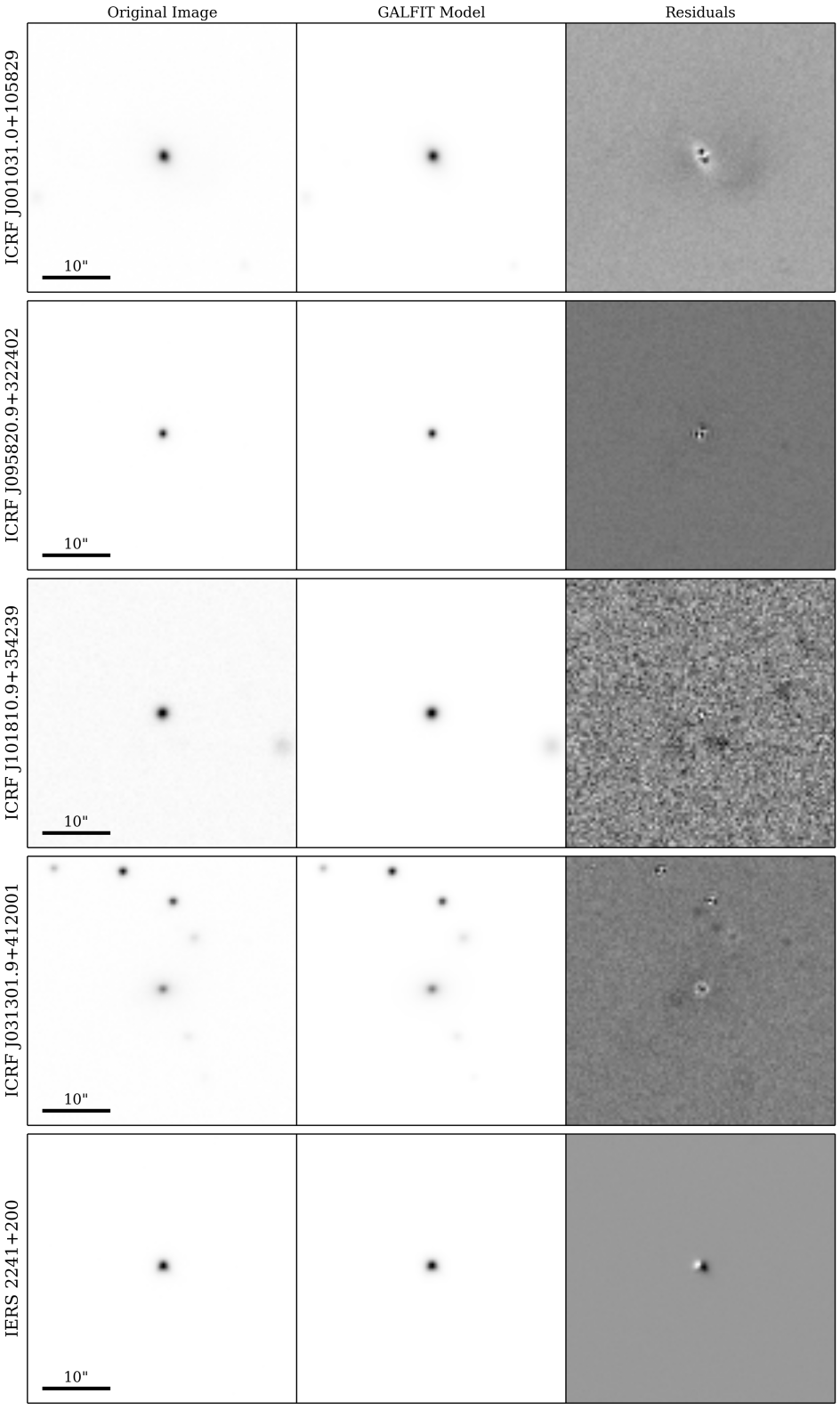

Figure 5.7. Same as figure 5.5. but for sources with Sérsic profiles.

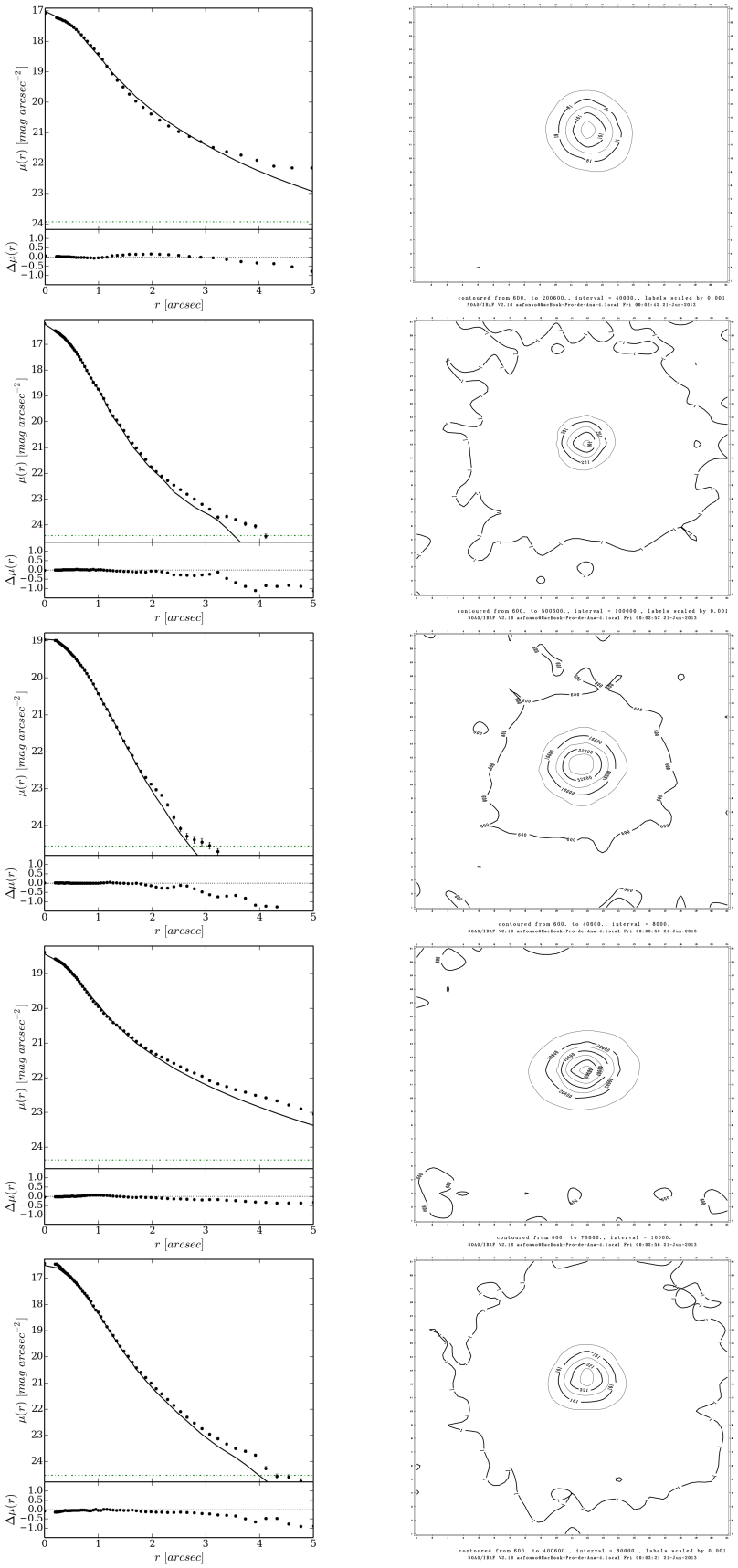

Figure 5.8. Same as figure 5.6. but for sources with Sérsic profiles.

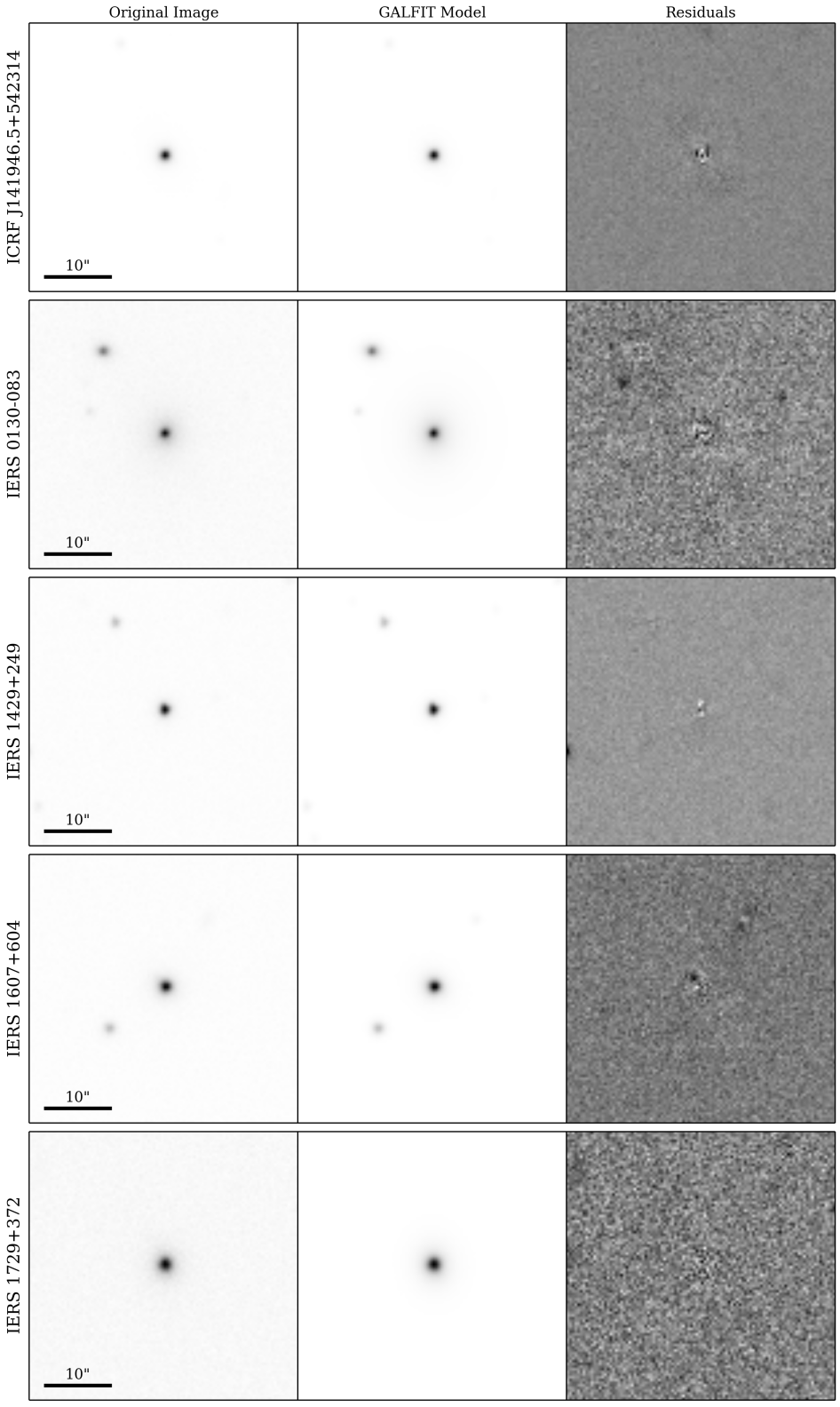

Figure 5.9. Same as figure 5.5. but for sources with PSF+Sérsic profiles.

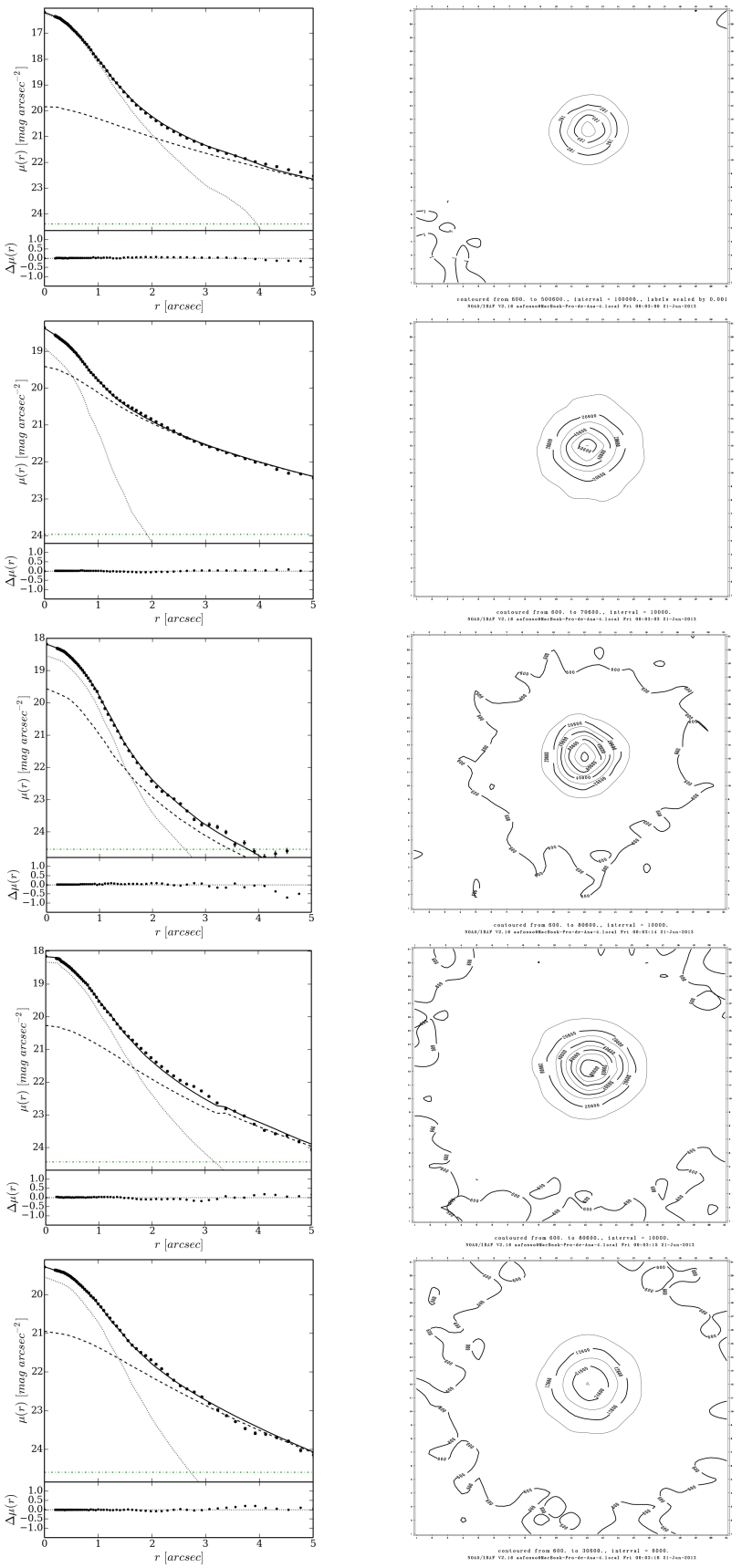

Figure 5.10. Same as figure 5.6. but for sources with PSF+Sérsic profiles.

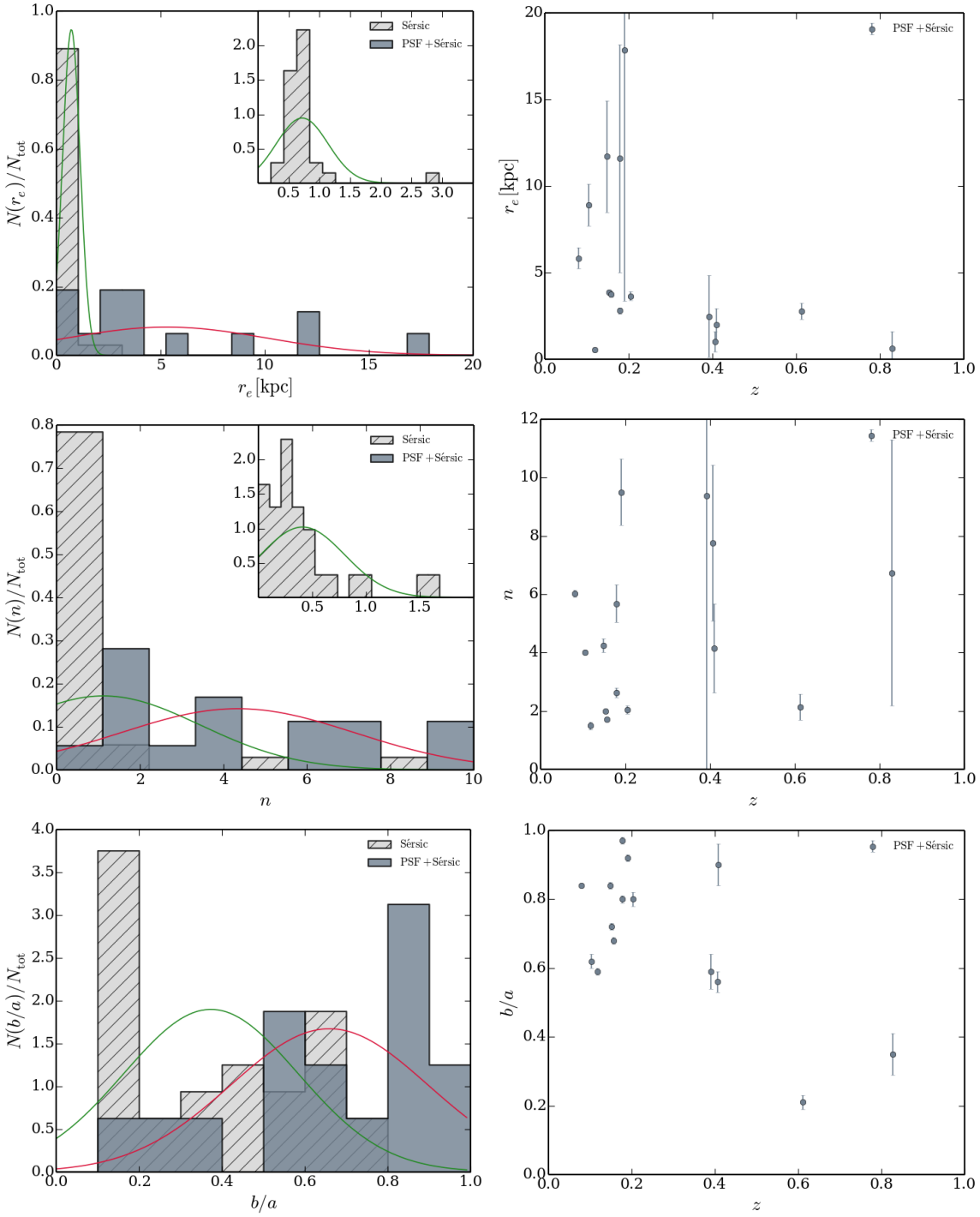

Figure 5.11. Left Column: Normalized histogram of the structural parameters of the Sérsic profiles of the compact and point-like+extended sources. The smaller panels refer to the distribution of the parameters of the compact sources fitted with a single Sérsic profile and whose distribution is badly seen in the bigger plots due to their high concentration at lower values. Right column: same parameters, but as a function of redshift for the Sérsic profiles of composite PSF+Extended sources. One object is absent of these plots on the right column due to the lack of a redshift measurement. The solid lines on the left panel are the Gaussian fit to each histogram: Sérsic in green and PSF+Sérsic in red.

point-sources of $r \sim 22.6$.

Applying the same methodology as in the case of SDSS DR9 images, I performed the morphological characterization of the two galaxies that have Stripe 82 data available: ICRF J001611.0-001512 and IERS 0049+003. The resulting analysis did not change the morphological class in which each object was classified based in the DR9 images. However, there are differences pertaining to the observed surface brightness profiles (see figure 5.12.). These differences may be connected with the different PSF that is characteristic of each image. Moreover, flux variations characteristic of the objects we are considering might be responsible for some of the observed difference. The total magnitude of both observations differs by ∼0.06 mag and ∼0.29 mag, respectively.

The deeper magnitude limit and the fact that the data points from figure 5.12. are best fitted in the case of Stripe 82 data make me choose as the final reported values for the structural parameters of these two sources in the table 7.3. in the appendix to be those derived from the Stripe 82 images.

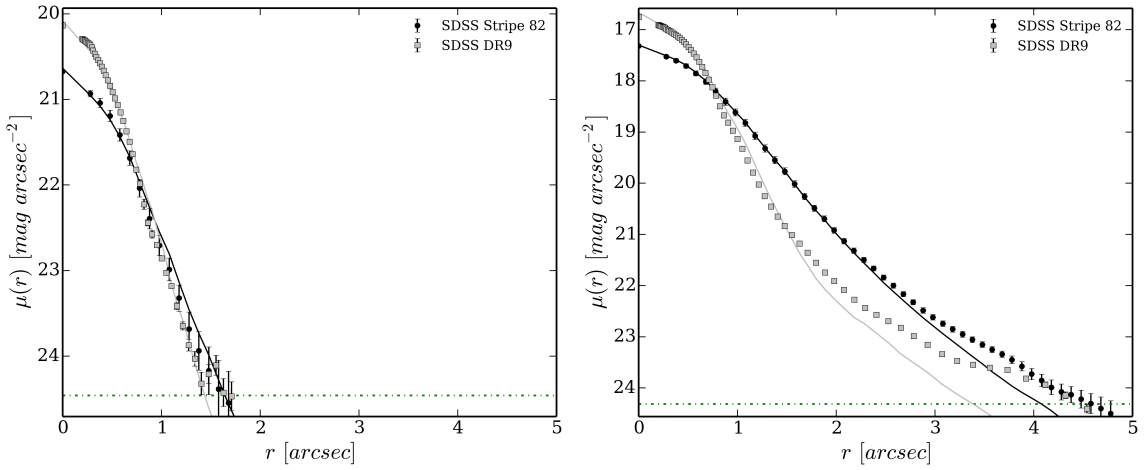

Figure 5.12. Comparison of surface brightness profiles between SDSS DR9 (in grey) and Stripe 82 (in black) data for the two sources imaged in the Stripe 82 region: ICRF J001611.0-001512 on the left and IERS 0049+003 on the right. The green dotted-dashed line represents the same as figure 5.6.

5.1.5. HST IMAGES ANALYSIS

The lack of stars surrounding the imaged area, due to their small size, limits the capability of constructing our one PSF. Thus, performing any morphological analysis on the available images is limited to the use of artificial PSFs such as those provided by the TinyTim software. After trying to reach reasonable results using this synthetic PSF, I found that the PSF profile could not model well ours objects. For example, in figure 5.13. I present the faintest source of the 25 with available HST imaging (ICRF J213410.3-015317, where the point-like component is not so prominent) and it is very clear how the models fail to properly fit the object. For brighter sources, the residuals got even worse.

This bad performance of GALFIT on HST images of ICRF2+ sources is mainly due to the fact that most of the obtained images are not dedicated to the observation of the targets of the ICRF2+ sample, rather observed by chance. Some are located at the edge of the CCD where the image quality is degraded, others in saturated CCDs or that bad observation configurations (such as an excess of exposure time that saturates the CCD) are present.

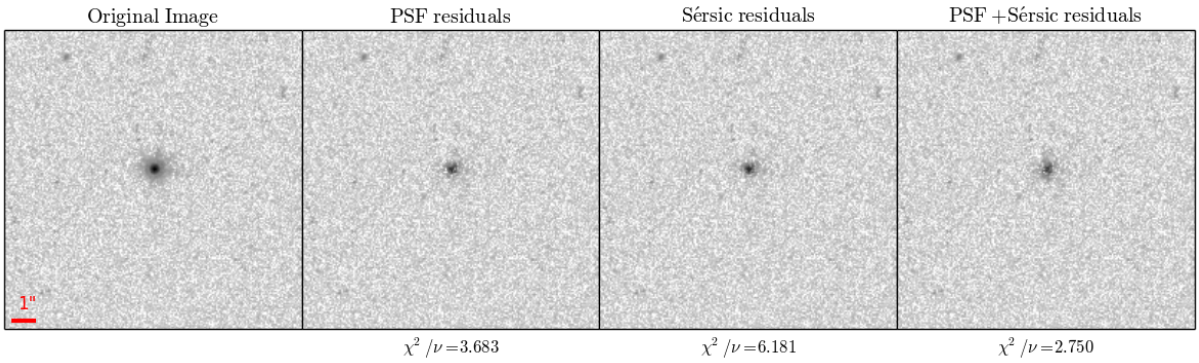

Figure 5.13. Example of HST modelling of ICRF J213410.3-015317 using three distinct approaches. As shown by the residual images none of the approaches can correctly model the object.

5.2. OPERGs

Having all the necessary files in place to run GALFIT, it is necessary to inspect the residuals after the first run. Whenever necessary, neighbouring objects were either masked out or simultaneously fitted according to their nature and relative position in the image. Saturated objects were always masked, objects in the image (galaxies and stars) at least five times brighter than the sky are also adjusted according to their type, i.e., stars fitted by a PSF and galaxies by a Sérsic profile and small faint objects distant from the centre were left unmasked and unfitted because they would not introduce any bias in the obtained parameters. If, after this first run, the residuals were not satisfactory, I added an additional Sérsic component to the object of interest until a reasonable result has been achieved. Following this recipe I got: 16 galaxies were best fitted using only one Sérsic component, 12 galaxies were best fitted using a two component model. The results are summarized in Tables 7.5. and 7.4..

In figure 5.14. one can inspect the distribution of the Sérsic indexes of the fitted components. For the one component sources, most of their values are above $n \sim 4$ (there is one galaxy with $n \sim 3.81$) which is expected from elliptical galaxies (see, for example Carroll & Ostlie, 2007, chapter 25). In what concerns the two component sources, the indexes of the inner component and of the outer one have distributions with lower values of n.

5.2.1. ONE COMPONENT SOURCES

Fifteen out of the sixteen galaxies were fitted by a single Sérsic profile. Exception made for object SDSS J155949.721+080517.65, a point-like object at $z \approx 2.2$ (see table 7.2.) that was fitted using a single PSF model. By checking the residuals, it is clear that simultaneous fitting of neighbouring galaxies works really well for getting rid of contamination (Chien Peng, priv. comm.). In three cases (SDSS J150721.87+101844.9, SDSS J160616.02+181459.8 and SDSS J170045.23+300812.8), masks were applied in order to check if nearby objects would affect the modelling of our galaxy of interest. I came to the conclusion that these objects are good enough to remain in the study sample. Concerning any remarks of unusual cases of this group of galaxies we have

- SDSS J170045.23+300812.8 has a faint one-sided optical jet (Capetti et al., 2000);
- SDSS J125433.26+185602.1 has a dust lane feature;
- SDSS J141028.05+143840.1 could not be modelled by GALFIT as the retrieved Sérsic index is not physically meaningful ($n > 10$).

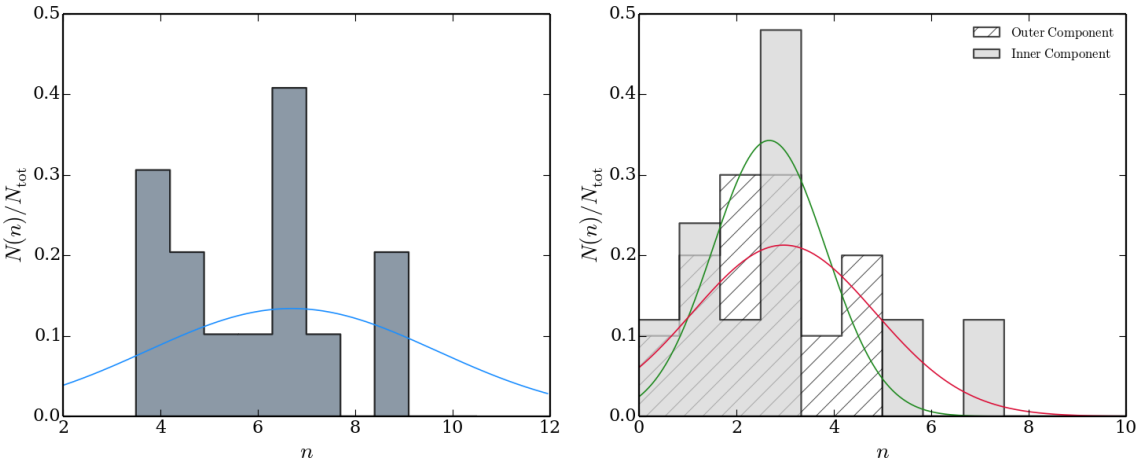

Figure 5.14. Distribution of Sérsic indexes of the optically passive elliptical radio galaxies for the one component objects (left) and for two component objects (right). In the two component case, the inner component refers to the smaller effective radii and the outer component refers to the larger one. The solid lines are the Gaussian fit to each histogram: One component Sérsic in blue on the left panel and outer component in green and inner component in red in the right panel.

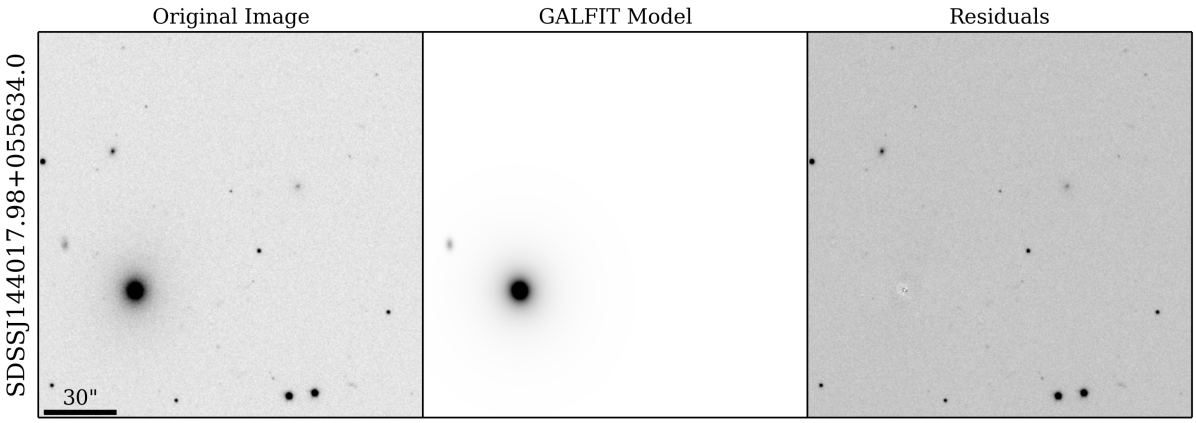

Figure 5.15. GALFIT results for a OPERG with one component. From left to right the input image, the best-fit model from GALFIT. The galaxy of interest is the brightest object in the image.

5.2.2. TWO COMPONENT SOURCES

The other twelve objects were fitted by two components and their neighbours were simultaneously fitted by a single Sérsic. Ten out the twelve were fitted by a set of two Sérsic profiles. Other two galaxies SDSS J160426.511+174431.19 and SDSS J164726.874+290949.54 are best fitted by a Sérsic profile plus a Gaussian-like source (Sérsic index $n \sim 0.5$). Regarding special features of special cases of these class of objects I have:

- SDSS J090937.446+192808.28 and SDSS J150656.417+125048.60 have a spiral structure that persists after a two component fit
- SDSS J113359.23+490343.4 has an intricate (shell-like) structure that may require a third component, but none was found to have reasonable parameters;
- A mask on its close neighbour was needed to fit galaxy SDSS J160426.51+174431.1 because it belongs to an interacting pair;
- SDSS J114505.025+193622.85 according to Baum et al. (1997) has an optical jet;

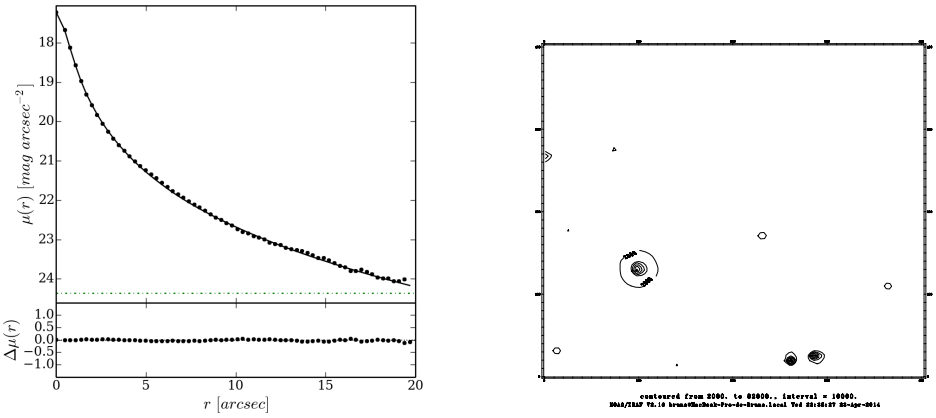

Figure 5.16. Same as 5.6. but for the galaxy of figure 5.15.. The contour image size is 158.4" × 158.4".

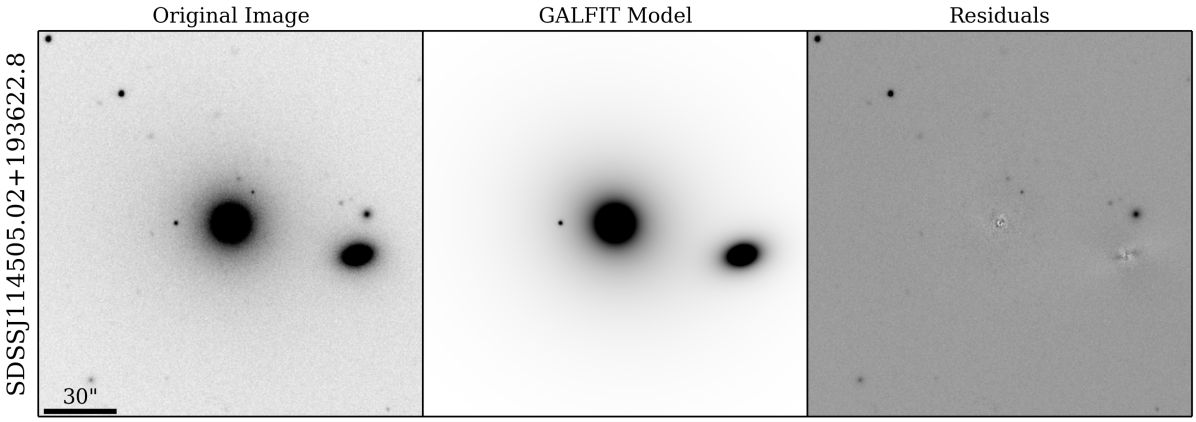

Figure 5.17. Same as 5.15. but for a galaxy fitted with two components. The galaxy of interest is at the image centre.

- Galaxies SDSS J121923.21+054929.7 and SDSS J141652.95+104826.7 are resulting in bad fits and, according with the literature, they have a nuclear/centred dust disc.

The last three objects may be seen with great detail in figure 5.19., where their structures are clearly noticed from HST imaging data.

5.2.3. LIGHT CENTROIDS

Regarding the determination of the optical centroid in the r-band images as measured by GALFIT we can check the results in table 7.5.. The centroid is computed as the first light moment of the model image representing the barycentric coordinates of the object compute as (see the section 10 of the SExtractor official manual [2])

$$\bar{x} = \frac{\sum_{i,j} I_{i,j} \times i}{\sum_{i,j} I_{i,j}} \quad \text{and} \quad \bar{y}\frac{\sum_{i,j} I_{i,j} \times j}{\sum_{i,j} I_{i,j}}, \tag{5.7}$$

where (i, j) represent the pixel coordinate positions in the x and y directions respectively. The results are converted back to a set of (ra,dec) coordinates by using the stored information on the image header and the *pywcs*[3]) package. Whenever the model requires two components the

[2]available at `http://www.astromatic.net/software/sextractor`
[3]`http://stsdas.stsci.edu/astrolib/pywcs/`

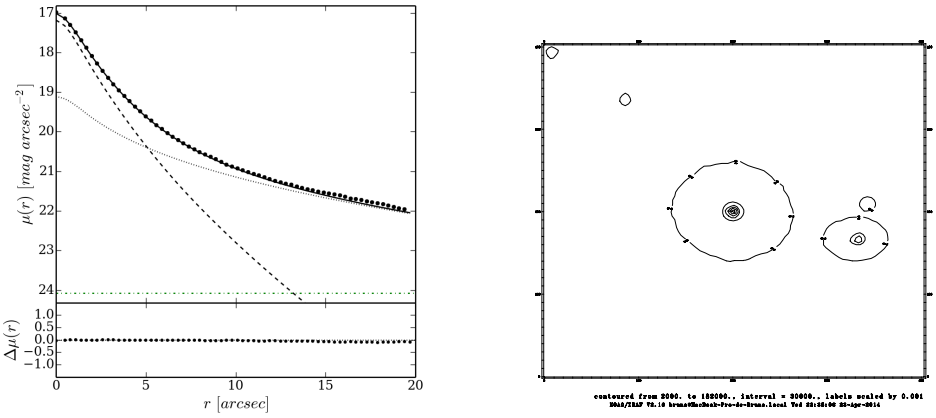

Figure 5.18. Same as 5.10. but for the galaxy of figure 5.17.. The contour image size is 158.4" × 158.4".

difference in the centroid positions of each model corresponds to a value Δ which is derived from the GALFIT positions x_c and y_c as follows

$$\Delta = s \times \sqrt{\Delta x^2 + \Delta y^2} \quad \text{where} \quad \Delta x = (x_{c,1} - x_{c,2}), \quad \text{and} \quad \Delta y = (y_{c,1} - y_{c,2}) \tag{5.8}$$

where s is the pixel scale of SDSS ($s = 0.396$"/pix). It is important to note that these errors correspond to the GALFIT formal uncertainties. For a better estimation of the actual error, numerical simulations exploring the parameter space have to be performed.

The displacement between the two components (whenever present) is always very small. In fact, it is smaller than one pixel (0.396") for 10 of the 12 galaxies.

5.2.4. STRIPE 82 IMAGES

Regarding the 28 galaxies of this sample, no sources were found to overlap the region of the Stripe 82 area.

5.2.5. HST IMAGE ANALYSIS

Considering the four sources with available HST imaging data, I was able to check the feasibility of determining the profiles of those galaxies to a greater detail. For three of the four sources there are clear sub-structures of the galaxies (dust discs, jets) around their central position. This may be inspected in more detail by looking at figure 5.19.. This also means that the determination of the centroid position has to be taken carefully when considering these objects which were already flagged as special when the analysis of the SDSS images was conducted.

For the remaining source, SDSS J170045.23+300812.8, we have available imaging from two filters around the r-band filter of the SDSS: F555W and F814W. On both filters the galaxy is best fitted with a single Sérsic profile. Here, the issue with the saturated star (impeding the best analysis from the SDSS image which was only achieved by masking the region with flux from the star) is minimized due to the better spatial resolution of the Hubble telescope leading to a greater separation between the OPERG source and the star. From figure 5.21. one can see that the derived profiles match well the data of the object. It is possible to see that the profiles derived from SDSS and HST images agree very well from ~ 1" scales up to ~ 8". The central regions of the profiles mismatch due to the broader PSF of the SDSS survey when compared to the HST one. The departure of the data points from the profile on the outermost regions ($r \gtrsim 6$") is due

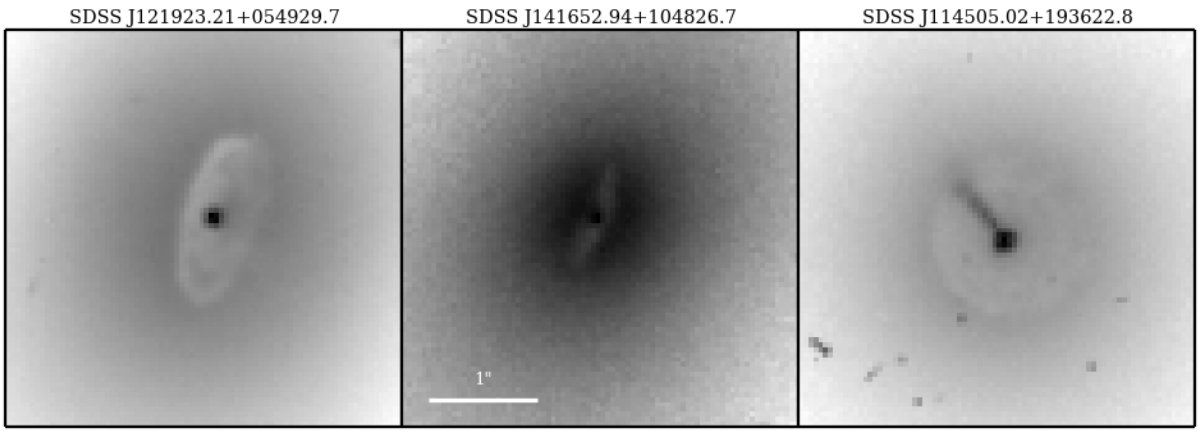

Figure 5.19. Central regions of perturbed galaxies from HST images for galaxies SDSS J121923.21+054929.7, SDSS J141652.94+104826.7, SDSS J114505.02+193622.8. On the two leftmost figures there is an evidence for a central dust disc. On the right figure there is a hint of a small dust disc and a strong jet of material linking the central bright region to the fainter dust ring edge.

to the contamination of the nearby saturated star.

As for its light centroid, it is the same down to the sub-arc second scale whether computing it on the SDSS image or on the HST image. The differences found are

$$\Delta\mathrm{RA} = \mathrm{RA}_{\mathrm{HST}} - \mathrm{RA}_{\mathrm{SDSS}} = \begin{cases} 0.1855” & \mathrm{F555W} \\ 0.1861” & \mathrm{F814W} \end{cases} \tag{5.9}$$

$$\Delta\mathrm{DEC} = \mathrm{DEC}_{\mathrm{HST}} - \mathrm{DEC}_{\mathrm{SDSS}} = \begin{cases} -0.2448” & \mathrm{F555W} \\ -0.2448” & \mathrm{F814W} \end{cases} \tag{5.10}$$

which indicates that the level of resolution of the HST may differ by a fraction of the SDSS pixel scale the SDSS centroid position of the source.

5.3. TESTING GAIA CAPABILITIES ON MORPHOLOGICAL CHARACTERIZATION OF GALAXIES

Considering that Gaia is designed to detect point-like sources, it is interesting to test the capability of retrieving the parameters from a set of bulge and disc dominated galaxies, and its dependence on the total contribution of the luminosity of the galaxy.

Parameter limits[4]	Units
$14 \leq m_{\mathrm{tot}} \leq 20$	mag
$0.05 \leq B/T \leq 0.95$	NA
$400 \leq r_d \leq 2000$	mas
$100 \leq r_b \leq r_d$	mas
$0.05 \leq b/a \leq 1.0$	NA

Table 5.2. Table with the defined intervals from which the galaxy parameters are taken.

[4]The position angle (θ) is fixed at zero for all simulated galaxies

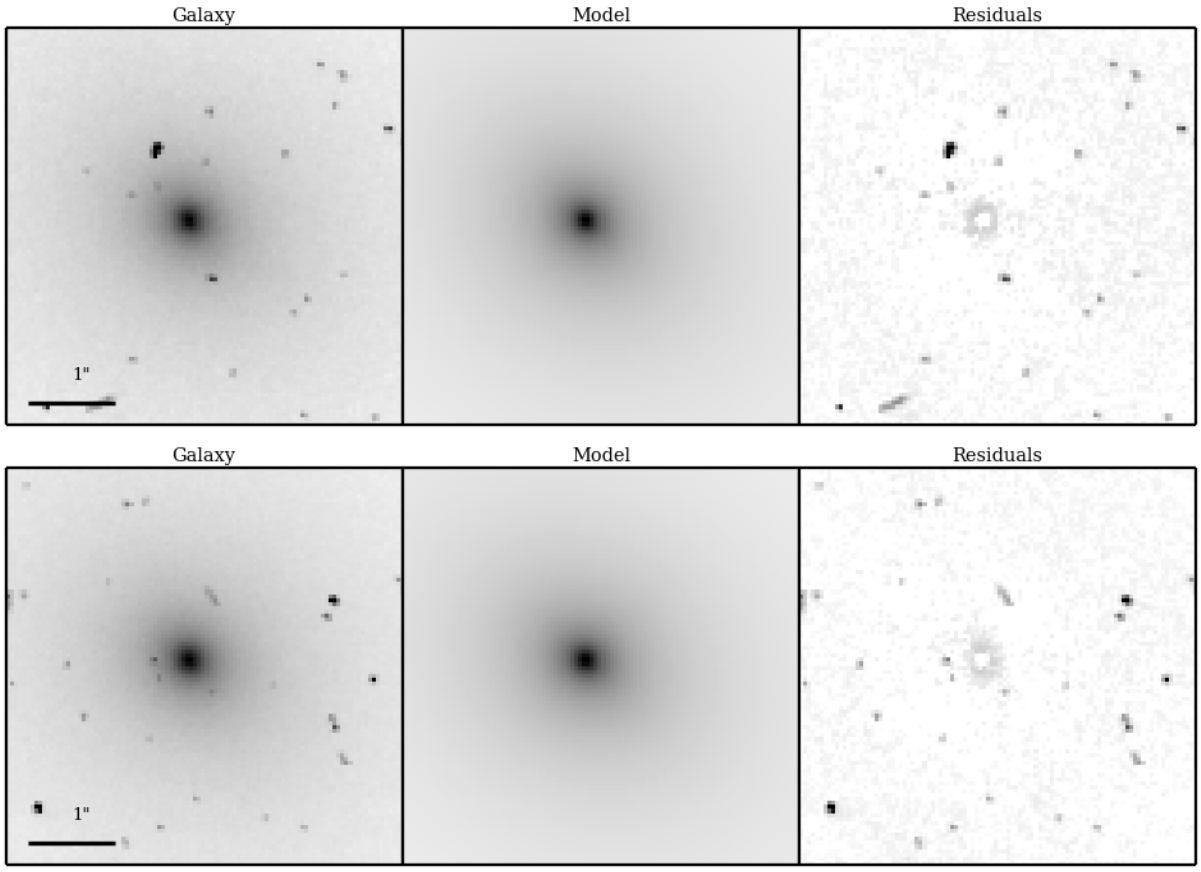

Figure 5.20. Same as 5.15. but for the galaxy with HST imaging available. On the top the one derived from the F555W filter and on the bottom the one derived from the F814W filter.

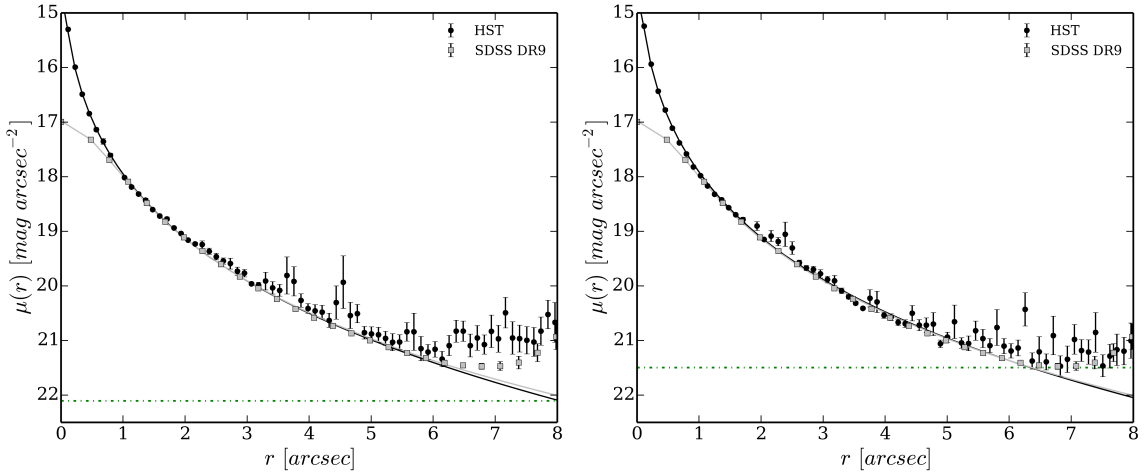

Figure 5.21. HST surface brightness profiles for galaxy SDSS J170045.23+300812.8 compared to their SDSS profile. On the left the one derived from the F555W filter and on the right the one derived from the F814W filter.

I performed a simulation to test it, based on 500 objects created from parameters taken from uniform distributions within certain limits. The later are presented in table 5.2., where there is a summary of the general configuration of this simulation over which the retrieval of the parameters will be tested. For all the simulations it was used columns AF2 and SM1 and AF2+SM1 simultaneously. The AF2 column has a smaller window, but a better resolution than the SM1

column that measures the flux in a more extended region but with less spatial resolution. That is the reason why I chose to perform the image simulations using the complementary configuration of both columns. Note that the SM1 and SM2 columns have the same configuration as they are used separately for each of the Gaia telescopes, and the AF2 column is that, from the astrometric field columns, with the greater window extent, along with AF5 and AF8 (see table 1.1.). Such simulations will allow for comparisons between the performance of each column separately to that obtained by combining data from both columns.

In figures 5.22. to 5.26. are presented the final results of the simulation. The intensity parameters are those that are better retrieved from the simulations. They show the expected trend that brighter galaxies are recovered more successfully than the fainter ones. As for the radii parameters, smaller components are retrieved with better accuracy that is also to be expected as in such cases most of their light falls within the Gaia windows thus allowing for a better constraint on the derived profiles. When comparing disc to bulge parameters, there is a clear better behaviour on the bulge component. Being the most concentrated profile with smaller radii from construction it is not to surprising to see that outcome as it is the dominant component in the regions that are better sampled by the Gaia windows.

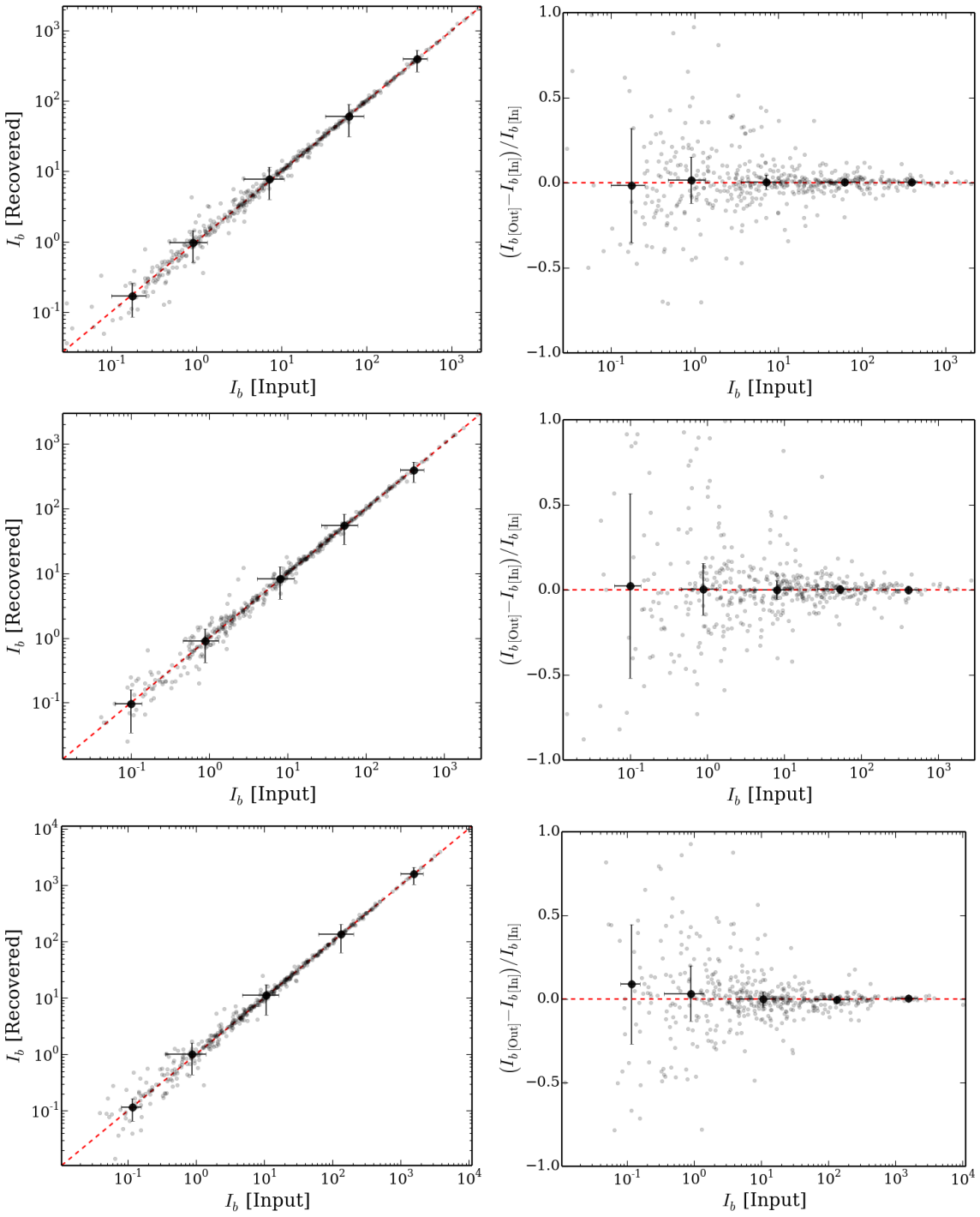

Figure 5.22. Comparison of the recovered values with the expected ones from the simulated objects. The red solid line indicates the one-to-one equality. The top panel corresponds to the case of AF2 only simulations. The middle panel to the SM1 only simulations and the bottom panel to the AF2+SM1 simulations. The right column shows the relative errors obtained on the parameters. In all panels the bigger filled circles represent the median value in equally spaced bins defined from the shown interval. The bars are the measure of the dispersion in each bin. For better visualization of the region of null fractional error, some points were left out of the plots on the right column.

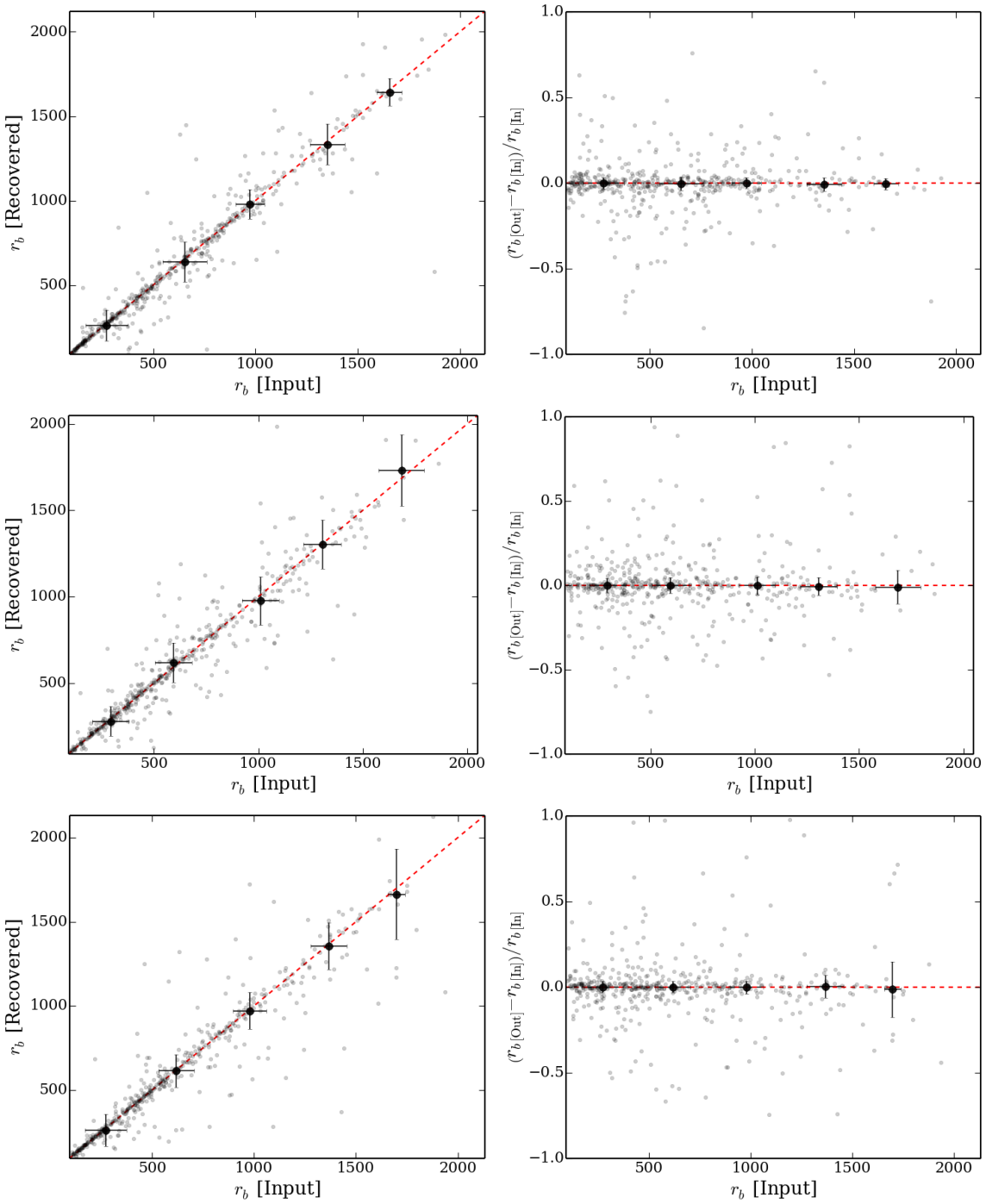

Figure 5.23. Same as 5.22. but for the bulge radius.

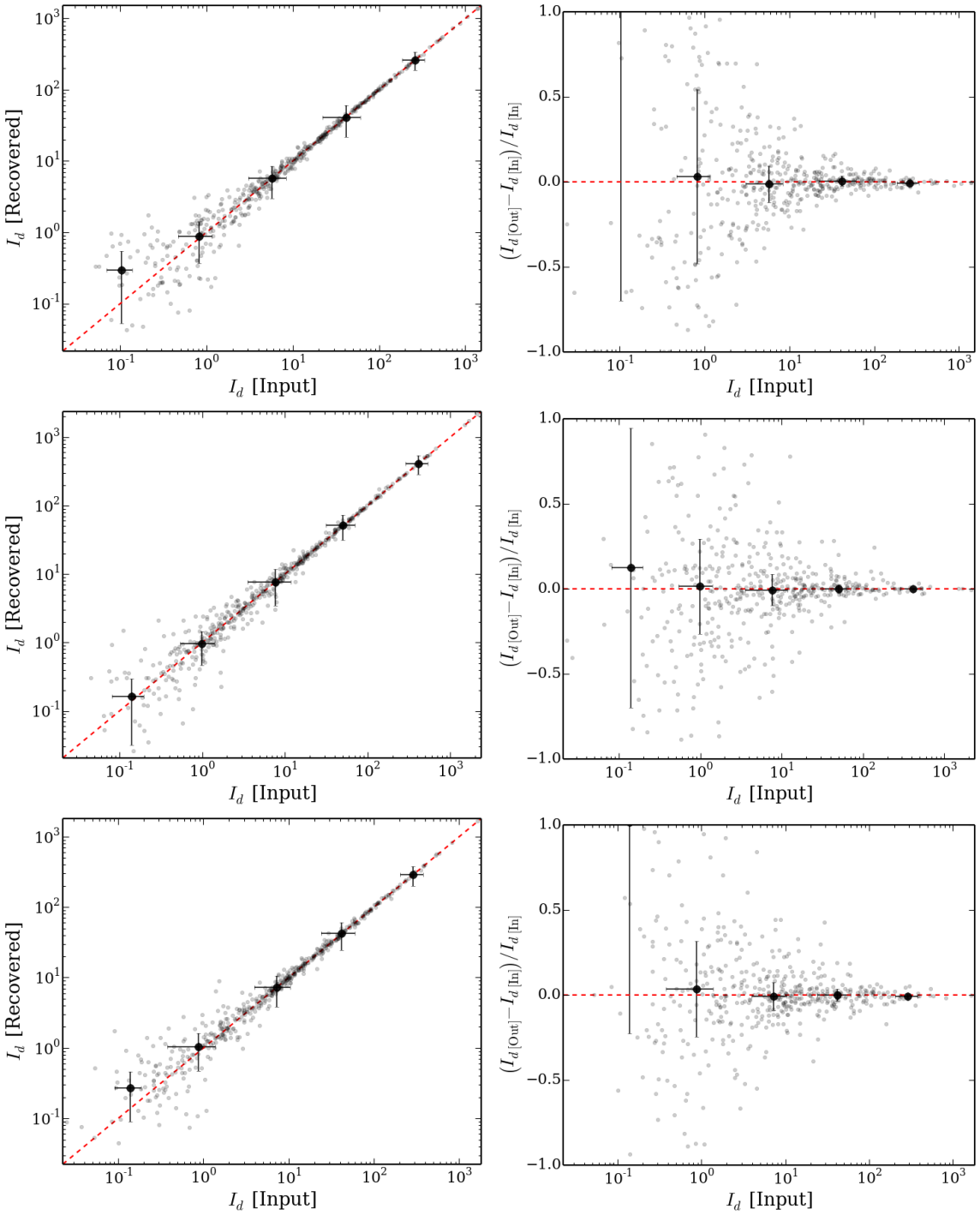

Figure 5.24. Same as 5.22. but for the disc intensity parameter.

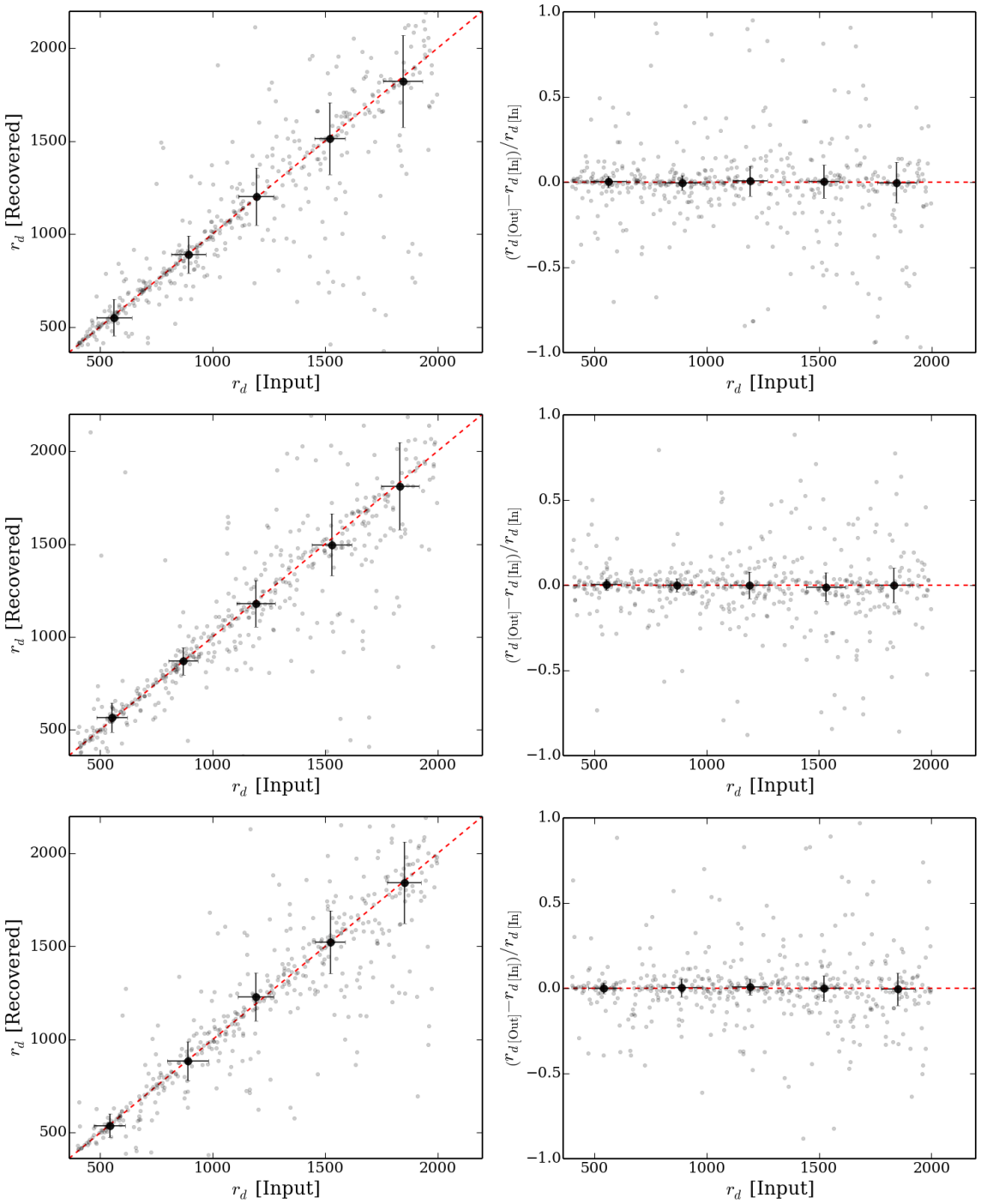

Figure 5.25. Same as 5.22. but for the disc radius.

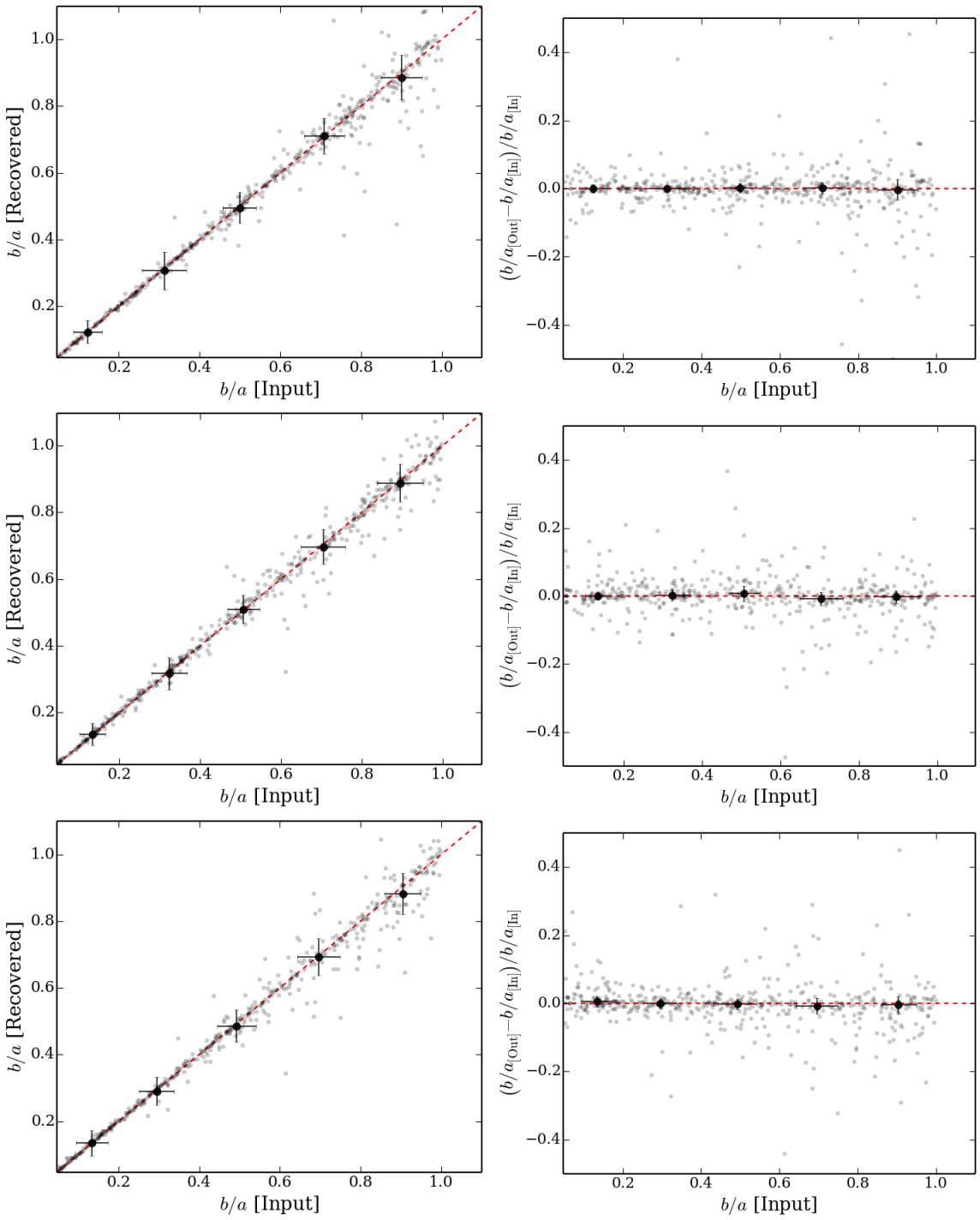

Figure 5.26. Same as 5.22. but for the axis ratio.

5.3.1. THE PARAMETER RETRIEVAL DEPENDENCE ON THE SIMULATED COLUMNS

As seen from the previous figures 5.22. to 5.26. there is not a clear difference between the results from different simulated columns. In that sense, I computed the mean relative error in each of the parameters to assess their overall performance with respect to the simulated windows. This is done in absolute terms as one aims to find which case has the minimum absolute error. The quantity

$$|\langle \Delta X/X \rangle| = \left| \text{mean} \left(\frac{X_{\text{out}} - X_{\text{in}}}{X_{\text{in}}} \right) \right|, \tag{5.11}$$

where X is one of the following parameters: I_d, r_d, I_b or r_b. The results for the simulations of this dissertation are shown in table 5.3. and summarized in figure 5.27.. Note that the dispersion around the reported values is still large (~ 0.05 for each point) which accounts for the dispersion observed in figures 5.22. to 5.26..

	$\lvert\langle \Delta X/X \rangle\rvert$		
X	AF2	SM1	AF2+SM1
I_d	0.183	0.127	0.203
r_d	0.134	0.114	0.108
I_b	0.049	0.035	0.060
r_b	0.008	0.084	0.024

Table 5.3. Median errors as a function of simulated column.

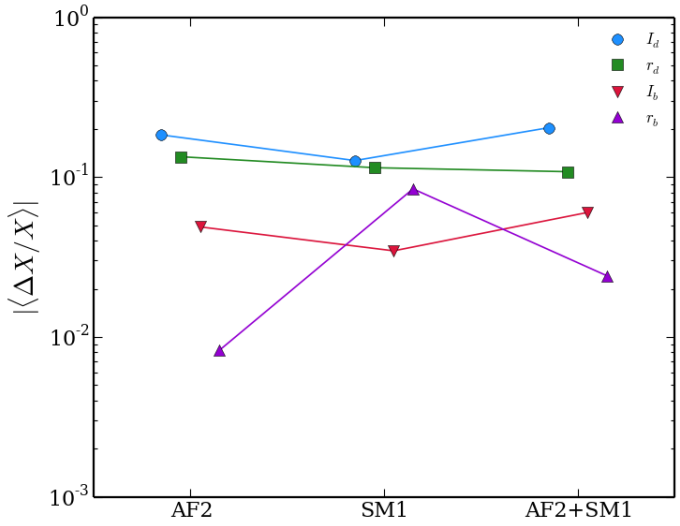

Figure 5.27. Mean errors as a function of simulated column for each of the bulge and disc parameters. The offset on the x-axis for each point was done purposely for facilitating the visualization of the data.

The first thing that comes out of the figure 5.27. is that, on average, bulge parameters are better retrieved that disc parameters. It is also seen that there is a slight improvement on using the SM1 column when compared to the AF2 column for all but the bulge radii which performs the worst in the single SM1 data. Considering the combination of AF2 and SM1 data the mean errors increase slightly for the intensity parameters and decrease for the radii parameters (with respect to the SM1 column alone). In the end, there is no preferred configuration seen from this plot that allows for the best estimation of structural parameters. Instead, one should consider

which parameters are most important and adjust the code accordingly. These results may be due to the small statistics of our sample that allow the influence of the outliers to mask the true behaviour of this quantity.

5.3.2. DETECTABILITY OF EXTENDED SOURCES WITH GIBIS

To assess the detectability of the extended sources with Gaia one can use the available image simulator GIBIS to check whether the galaxies will be seen and in what conditions. Considering the size of the transmitted windows and the size of the extended sources and respective magnitudes from the analysis of section 5.2, I concluded that nine out of the 28 objects could be detected and simulated with GIBIS. Because the simulator only takes as input combinations of bulge and disc galaxies (the Sérsic profile implementation has not yet been done), that corresponds to a Sérsic profile of $n = 1$, $n = 4$ or a combination of both, I ran GALFIT for these candidates assuming these fixed profiles. In this sense it is useful to get the relation between disc scale length and disc effective radius that is

$$r_d = \frac{r_e}{\kappa(1)} \approx \frac{r_e}{1.679}, \tag{5.12}$$

where $\kappa(1)$ is the value of the parameter in equation 3.8 when $n = 1$ and it was taken from Table 1 of Ciotti & Bertin (1999). GIBIS input also requires magnitude information of the V band and the V-I colour. To perform such computations I used Lupton (2005)[5] transformation equations as recommended for galaxies without strong emission lines. This means that, using SDSS gri magnitudes, one can get the value of V and I from

$$V = g - 0.5784(g - r) - 0.0038 \tag{5.13}$$

and

$$I = r - 1.2444(r - i) - 0.3820. \tag{5.14}$$

The value of the bulge to total ratio is computed as the ratio between the flux of the bulge model compared to the total flux of the model as seen in equation 4.5. Finally, the coordinates of each simulated object are set such that no overlap between sources happens. The other parameters come straight out of the GALFIT results. The table with the compilation of the information for each of the simulated galaxies is displayed in table 5.4..

To test the recuperation of the parameters, it was used the same process described in the previous section, but now with two completely independent components for which we have different position angles and axis ratios. The simulation used four CCD columns (AF2, AF5, AF8 and SM1 that have the better compromise between spatial resolution and window size) and eighty three transit angles following the nominal scanning law of the Gaia satellite for galactic coordinates $(l, b) = (125°, 25°)$. The G band magnitudes used in the fitting process to constrain the intensity parameters are also obtained from the GIBIS simulations output. The overall picture is that the retrieval of structural parameters is not very successful for this sample. In some cases we can retrieve the intensity parameters of the disc (2 galaxies) and of the bulge (4 galaxies), but for the remaining that quantity is underestimated. As for the radii, the values tend to be overestimated. Note that the bulge radius is more successfully retrieved for the medium sized galaxies. As for the axis ratio it is generally underestimated for both components (with one exception for the disc component). Again, the bulge value seems to be more in agreement with what was expected. As for the position angle of the galaxy, there is a mix of underestimation and overestimation of the values in both components. These results might due:

[5] http://www.sdss3.org/dr9/algorithms/sdssUBVRITransform.php#Lupton2005

ID	Code	η	ζ	V	V-I	B/T	r_b	$(b/a)_b$	θ_b	r_d	$(b/a)_d$	θ_d
1	202-1	-60	75	16.52	1.46	0.89	2.51	0.64	-5.6	4.03	0.69	-21.77
3	202-2	0	75	17.44	1.28	0.56	0.76	0.44	87.17	4.2	0.67	72.21
5	202-3	60	75	14.15	1.31	0.88	3.65	0.78	-75.7	3.74	0.86	-60.08
9	202-4	30	45	15.42	1.35	0.84	1.83	0.75	8.18	3.34	0.73	28.85
10	202-5	60	45	16.67	1.5	0.48	0.42	0.47	61.21	1.79	0.59	-47.08
20	202-6	60	-15	15.62	1.4	1	4.08	0.79	79.49	-	-	-
22	202-7	-30	-45	16.54	1.38	1	2.79	0.92	-74.9	-	-	-
23	202-8	0	-45	17.42	0.55	1	0.09	0.69	82.53	-	-	-
28	202-9	0	-75	14.71	1.36	1	3.8	0.86	89.36	-	-	-

Table 5.4. Table with the input parameters required by GIBIS. (1) ASPA identification number; (2) Code of the object to be simulated, 202 means galaxy; (3) and (4) image coordinates of the simulated object; (5) V band magnitude; (6) V-I colour; (7) Bulge to total ratio; (8) effective radius of the bulge in arc seconds; (9) axis ration of the bulge; (10) position angle of the bulge; (11) disc scale length in arc seconds; (12) and (13) same as (8) and (9) but for the disc component.

- either to the large size of the simulated galaxies (most components have $r \gtrsim 2"$), as we have seen from the simulations that the results are worse;
- and/or it is because we are in the presence of bulge-dominated galaxies (all nine of them have $B/T \gtrsim 0.5$) for which retrieving the disc parameters is more difficult.

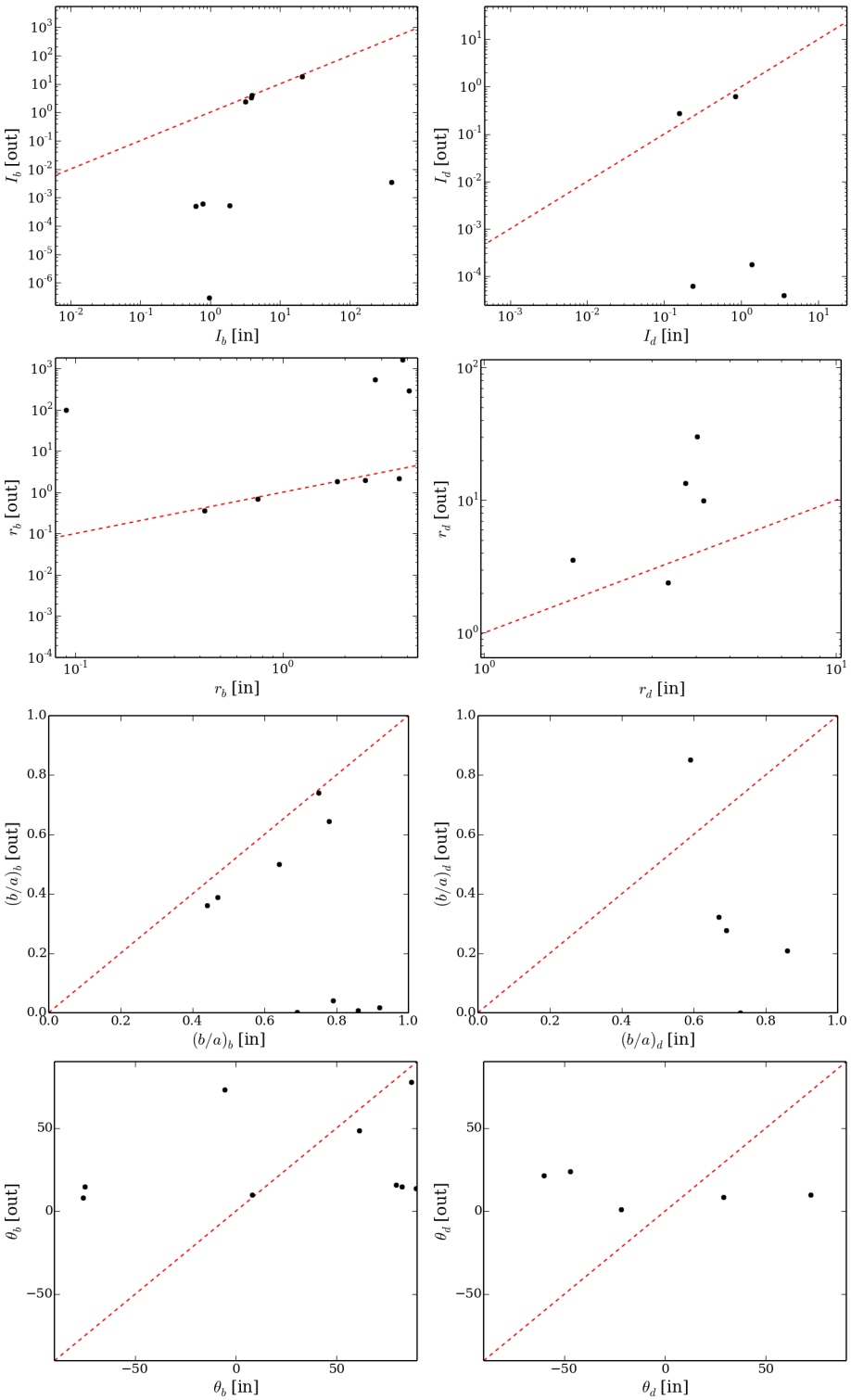

Figure 5.28. Comparison between input and output values for the nine galaxies simulated with GIBIS with 83 transits. The red dashed line indicates the one-to-one equality. The left column is related to the bulge parameters and the right column to the disc parameters. There are only five points in the right column since only five of the nine simulated galaxies have a disc component.

CHAPTER 6

DISCUSSION

"Failure is inevitable, unavoidable but failure should never get the last word. You have to hold on to what you want. You have to not take no for an answer and take what is coming to you. Never give in, never give up. Stand up. Stand up and take it."

- Get Up, Stand Up; Grey's Anatomy

Contents

In light of the methods and results presented in the previous chapter there are some remarks to be highlighted. These will be discussed separately following the same structure of the Results chapter. In the first section, I summarize the results concerning the ICRF2+ sample and then contextualize them in the framework of the current research on the topic. Next, I point out some of the key features that came out from the analysis of the passive and elliptical radio galaxies stressing the limitations and strong points of doing a two-dimensional surface brightness decomposition. Lastly, I consider the aspects related to the retrieval of structural information from Gaia data as inspected by the simulations performed for this dissertation and compared with other similar studies.

6.1. ASTROMETRIC SUITABILITY OF ICRF2+ SOURCES

I would like to start this discussion by referring that the work presented in this dissertation regarding the morphological characterization of ICRF2+ sources in the optical is unique in its methodology. In what concerns the compactness/detection of host galaxies of the defining radio sources the results of 16 objects out of the 198 ($\sim$ 9% of the objects) show clear evidence for the presence of an extended component, a number that might be larger (reaching 18%) as in 32 objects there is a hint for the presence of an extended component. But, in the majority of the cases ($\sim$ 74%) the objects are well described as a point source, with no indication of any extended component as seen in SDSS DR9 images. Furthermore, all the images show residuals of the order of less than 15% of the original flux from the object after model subtraction.

Such findings are in agreement with other studies regarding the compactness of quasar galaxies to be targeted by Gaia, as for example Andrei et al. (2012a,b) and Taris et al. (2013) that have conducted independent studies using *Digital Sky Survey* (DSS) data in conjunction with data

from dedicated observations to probe the object's morphology.

Thus, great part of the defining sources of ICRF2 and of the Bourda et al. (2011) sample are suitable for alignment between reference systems as they are point-like objects. The particular case of the compact sources that are modelled with a single extended profile might also be considered for alignment purposes. As seen in the previous chapter, they are quite small in nature, with low Sérsic indexes, comparable to that of a Gaussian profile ($n = 0.5$) and the extended light just marginally detected. This means that the AGN component still dominates the flux of the object, but there is a faint extended light component that is included in the model leading GALFIT to result in a slightly broader profile with respect to that of a point-like source.

The remaining sources may be useful to investigate the influence of the host emission on the determination of the light centroid. Their physical size (r_e) is computed from

$$r_e = d_A \theta, \tag{6.1}$$

where d_A is the angular diameter distance from the standard cosmological model and θ is the angular size computed from the images. This quantity shows a hint of correlation with redshift. The size evolution is expected from the hierarchical growth picture of the cosmological model currently accepted (Wuyts et al., 2010; Poggianti et al., 2013; Stringer et al., 2013; Morishita et al., 2014). The possible increase of the axis ratio with redshift might also be just a consequence of galaxy evolution since in the past, galaxies were more irregularly shaped (Delgado-Serrano et al., 2010, and references therein).

As for galaxies that are included in the Stripe 82 Data release, which is ∼2 magnitudes deeper and thus the detection of the host galaxy is more likely, two sources, ICRF J001611.0-001512 and IERS 0049+003, have available imaging data. Comparing Stripe 82 analysis with DR9 data the conclusion is that morphological classification is consistent, but differences in the surface brightness profile distributions of the two galaxies were detected. The later may be caused by intrinsic flux variations of the objects along the 20 different periods (Annis et al., 2011) that composed the Stripe 82 data, as blazars are known to be variable sources. Additionally, the PSFs of each dataset are not the same, thus some differences are expected. Despite the discrepancies, the total magnitude differs by less than 0.3 mag.

6.2. OPTICALLY PASSIVE ELLIPTICAL RADIO GALAXIES

In what concerns these extended sources it is obvious that the accurate centroid determination is not an easy task since one has to deal with many effects that come into play. For instance, even in the case of passive elliptical galaxies that are characteristically devoid of gas (see, for example Sparke & Gallagher, 2007) and thus only their smooth stellar light is visible, the quantification of their surface brightness is a complicated issue. Neighbour contamination, presence of dust, multiple light components and asymmetrical light distributions all contribute to the uncertainties of the centroid determination. In addition, one is limited to the current pixel scale when considering the precision of our measurements. Nevertheless, GALFIT is a strong tool that allows the user to tackle most of this issues and provide the best estimates of the light centroid of these objects.

Regarding the morphological parameters of the sample, the elliptical nature of their profiles is confirmed. In all one component sources, all indexes are $n \gtrsim 4$ and in the composite profiles, most of the inner components are steeper than an exponential disc with only 5 out of 12 two component galaxies having $n < 2.5$. These lower Sérsic index inner components might indicate that the complex modelling of the two component sources, using two profiles in between

those of classical bulges and exponential discs hint that a more dedicated profile fitting is necessary. For instance, one may use models such as a core-Sérsic elliptical profile as that reported in Dullo & Graham (2013, and references therein) that might be more appropriate for these cases.

In this sample, sixteen (13 one component sources and 3 two component sources) out of 28 show light distributions with no reported problems in fitting their light distribution as seen in the previous chapter. The comparison of the light centroid of each of the two component objects showed that the differences are almost always smaller than the pixel size of the images. The two cases for which that did not happened are SDSS J150656.41+125048.6 with a persistent spiral pattern after model subtraction and SDSS J160426.51+174431.1 which has a close interacting companion masked during the fit that have centroid differences of 0.57" and 0.72" respectively. It is interesting to note that even in the cases where the galaxy features would not allow for an excellent model subtraction the differences between the two light centroids remain quite small, of the order of the pixel size of the images. This aspect might indicate that the centroid determination can be performed accurately at sub-arcsecond level even when perturbed morphologies affect slightly the two dimensional fit.

With respect to the HST images available I could perform a morphological quantification of the profile of SDSS J170045.23+300812.8 in two filters. Similarly to the results obtained with Stripe 82 data, there is no change in morphological class between the analysis performed with SDSS and HST data. But there are small differences concerning the light centroid, with deviations of the order of a tenth of an arc second. These differences are certainly related to the limited pixel size of the SDSS images that is of 0.396"/pix.

As for the feasibility of using Gaia observations to determine the central peak of their light profiles it is encouraging to note that the bulge components are those that have better structural determination of the parameters since they are the dominant component in the centre of galaxies and are smaller than the disc counterparts that all contribute to the favourable case of a better astrometric determination of the galaxy central position.

6.3. INFERRING MORPHOLOGICAL PARAMETERS FROM GAIA DATA

From the image simulations point of view, all parameters seem to be well recovered within certain limits. Brighter galaxies, smaller galaxies and more elliptical than round seem to be better characterized from Gaia data in all of the simulated columns. Nevertheless, when comparing with the results of Krone-Martins (2011); Krone-Martins et al. (2013) my results are not consistent in the sense that in their case they find the disc parameters to be better retrieved from SM1 simulated data when compared to the bulge parameters. However, de Souza et al. (2014) found that the disc galaxies will likely not be detected by Gaia on-board processing unit due to their extended profiles. Thus, the better capability of retrieving bulge parameters when compared to the disc parameters in combination with the high probability of detection of these objects will likely boost the chances of studying the structure of extra-galactic objects from the data obtained with Gaia.

With respect to the three different simulation runs (concerning three different instrument configurations) I have not found any striking improvement by using a single AF2 or SM1 configuration or using both simultaneously. However, a closer look at the overall performance of each column does indicate that each configuration has its specific advantages. The SM1 column is the best for retrieving intensity parameters, the AF2 is the best for recovering the bulge radii and the combination of SM1 and AF2 works best for the radii parameter. The fact that the bulge radius is better retrieved in the AF2 data is expected since it probes with greater spatial resolution the

region where this component is dominant. As for the disc radius the larger window extent of the SM1 column effectively improves the recovery of this parameter and is slightly more effective when considering it together with the AF2 column. The intensities parameters show similar behaviours and the fact that it works better for single SM1 data could be to the consideration of the full extent of the galaxy important to measure the total brightness of the object. The rise observed in the AF2+SM1 combination could be related to some trade-off between the improvement in the radii recovery and the lower accuracy of the total brightness. Although it is important to bear in mind that the relatively small number of simulated galaxies might induce deviations in the behaviour of each parameter due to the existence of large outliers that affect more effectively the mean fractional error.

For the case of the nine objects simulated with 83 transits through GIBIS, the structural parameters do not seem to be retrieved with the same level of confidence as seen from the image simulations. For instance, there are cases where the bulge component is recovered with overestimated radii or underestimated brightness and the same happens for the disc component. As for the axis ratio, the later is systematically underestimated. The position angle presents the worst results of all retrieved structural parameters. It is possible that the large extent of the simulated galaxies prevents one from successfully constrain the structure of these sources. Krone-Martins et al. (2013) and de Souza et al. (2014) have only simulated small galaxies with radii smaller than the SM1 window (2 arcseconds) as it was done in the image simulations in the section 5.3. In order to analyse this further, I have performed similar simulations for all 28 galaxies using my own code as presented in Chapter 4 and combining AF2+AF5+AF8+SM1 data. The results are presented in 6.1. and indicate that the problem might indeed be related with the size of these objects as they are somehow consistent with those of figure 5.28..

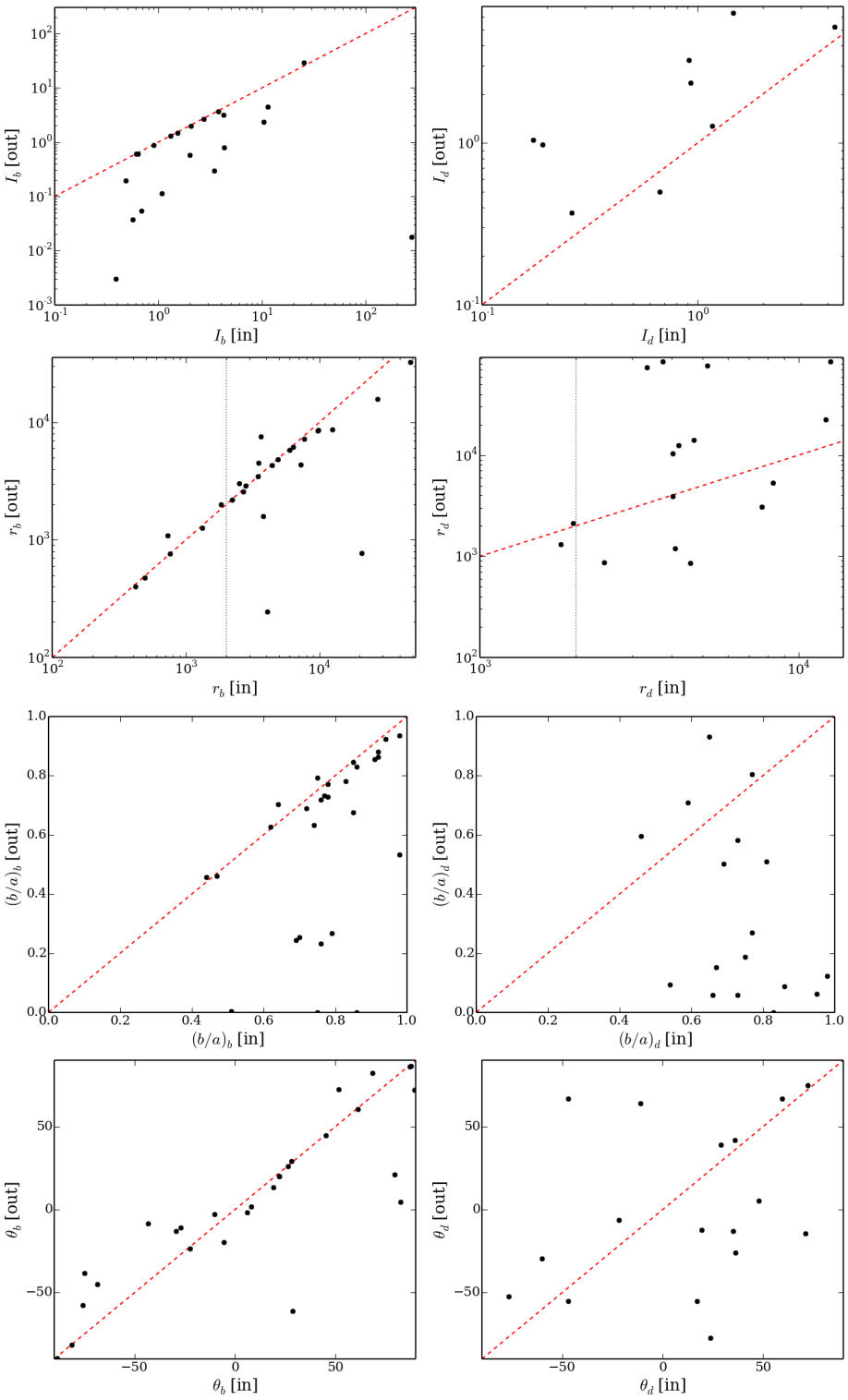

Figure 6.1. Comparison between input and output values for the 28 OPERGs simulated with my code. The red dashed line indicates the one-to-one equality. The left column is related to the bulge parameters and the right column to the disc parameters. There is less points in the right column since only some galaxies have a disc component. The vertical dotted line on the radii plots marks the 2" limit of the Gaia windows.

This page intentionally contains only this sentence.

CHAPTER 7

CONCLUSIONS & FUTURE WORK

"The early bird catches the worm. A stitch in time saves nine. He who hesitates is lost. We cannot pretend we have not been told. We have all heard the proverbs, heard the philosophers, heard our grandparents warning us about wasted time, heard the damn poets urging us to seize the day. Still, sometimes, we have to see for ourselves. We have to make our own mistakes. We have to learn our own lessons. We have to sweep today's possibility under tomorrow's rug, until we cannot anymore, until we finally understand for ourselves, what Benjamin Franklin meant: [t]hat knowing, is better than wondering. That waking, is better than sleeping. And that even the biggest failure, even the worst, most intractable mistake, beats the hell out of never trying."

- If Tomorrow Never Comes; Grey's Anatomy

Contents

7.1. CONCLUSIONS

As seen throughout this dissertation, there are a number of different ways to characterize and/or quantify the shape of galaxies that we observe in the Universe. The use of analytical profiles that adjust the data are paramount in the capability of consistently analyse a large number of objects in the same conditions to better establish comparisons with other works. This is particularly important considering the number of sources/images that one has to process and analyse correctly.

Taking advantage of the computer capabilities and software that enabled me to complete this project, I am now in a position to derive some conclusions about the results that were obtained. As this project was subdivided into three different, interconnected, major results sections, I will briefly conclude on each of the topics in the three separate paragraphs that follow.

The main conclusion to take from the work carried out in the context of the ICRF2+ sample project is that a great portion (around 3/4 of the studied sample) of ICRF2+ sources are suitable candidates (as seen from SDSS r-band imaging data) for being used as the defining sources of the

GCRF. This is reinforced by the detailed morphological study of each candidate and confirmed by the small amount of residual light left ($< 15\%$) in all the modelled sources.

Optical determination of the light centroid of extended galaxies is not a simple task when considering all the possible effects that need to be taken into account and for which GALFIT is not yet prepared to deal with. Nonetheless, among the sample of elliptical galaxies there are 16 (out of the 28) objects that show simple light distributions that can be modelled with excellent results divided into 13+3 one and two component sources, respectively. Furthermore, differences between the light centroid from available HST imaging and SDSS DR9 data may be justified by the limiting spatial resolution of the latter. As a last remark, differences between the two light centroid on the two component galaxies are very small, comparable to the pixel size of the images they were computed on, even when some issues prevent a perfect modelling of the source.

The retrieval of structural parameters from Gaia simulated works better for the bulge related parameters. Nonetheless it still performs reasonably well for the disc related parameters. In general, brighter, smaller and flatter galaxies are better retrieved that their counterparts. There also does not appear to be a single combination where the recovery works best for all the considered parameters. For the disc and bulge intensities the SM1 data perform better. For the bulge radius it is the single AF2 data that yields the best results. For the disc radii, the AF2+SM1 data work the best.

However, when applied to the OPERG sample, such behaviour is no longer found and problems in retrieving the structural parameters arise. In particular, there is a systematic underestimation of the intensities and overestimation of the radii for some objects. This issue seems to be related to the size of the galaxies, being too large when compared to the Gaia window sizes.

7.2. FUTURE WORK

As it is common in science, progress never stops. With that in mind, this project can still be improved in many ways being it the acquire of new data or the implementation of a new software to analyse the currently available. Nonetheless, I believe that this dissertation represents a solid basis for future follow-up of ICRF2 and future samples of defining sources of reference frames; for the search of optical-radio offsets in AGNs and of the retrieval of structural parameters from Gaia data.

Several tasks can certainly take advantage of the work published in this dissertation, like the ones described in the following subsections.

7.2.1. ICRF2+ SOURCES

To use the available HST imaging of the ICRF2+ sources (see table 7.1.) in order to check if the improvement in resolution and sensitivity allows the detection and characterization of the underlying extended emission from the galaxy that hosts the AGN. Especially consider the PSF model to be used for the subtraction of the light coming from the AGN as it seems that the synthetic PSF computed with TinyTim does not perform well for this task.

To extend the analysis to the rest of the ICRF2 sample which comprises a total of 3414 sources (of which 295 are the defining sources) and to other extensions proposed by the scientific community (Charlot & Bourda, 2012). On other note, it would also be interesting to have dedicated surveys in the optical for these kind of objects that aim at good spatial resolution and deep imaging. In that way, one would be more certain of the compactness of the sources and it would

be possible to detect fainter and smaller host galaxies.

Testing the 2D modelling of these sources using a different software, AIDA, developed by Uslenghi & Falomo (2011) that is more oriented to the cases where very bright nuclear components exist, such as quasars, to check the robustness of the results obtained with GALFIT. This shall be possible to the grateful assistance of M. Uslenghi which kindly provides the source code upon request albeit it being still in beta state.

7.2.2. DETECTABILITY OF GALAXIES WITH GAIA

Gaia is an all sky survey that will observe millions of uncharted extragalactic objects and many of those sources will have an extended component in their light distribution. It is, therefore, important to understand if Gaia data will permit to retrieve the properties of these objects in detail. One of the basic quantities that can be derived from the observations is the morphological information and, in that sense, I have found that there is a problem when considering galaxies with a large extended component, which might be due to the window size limits of Gaia. If so, then this limitation will affect the results, namely those related with the retrieval of galaxy's structural parameters.

Concerning the image simulations with GIBIS, additional tests could be carried out to discern the nature of the errors on the recovery of morphological information from model fitting. In particular, one should aim to assess the impact of the window size on the retrieved parameters that would enlighten the issue at hand. This could be done by extending my simulations to larger radii values and run them with different window sizes. Such tests would allow for a proper characterization of a broad range of galaxy types, from pure disc to pure bulges, and their behaviour when considering windows of larger sizes. If such tests indicate that the problem with fitting galaxy profiles is related to the small window extent of Gaia, then new methods and algorithms could be developed in order to maximize the science output from Gaia data for the extragalactic field.

In addition, one could test the impact of the bulge-to-total light ratio on each of the derived parameters and adjust the image simulations to a more general description of galactic profiles such as the inclusion of Sérsic profiles with variable indexes in the fitting procedure. Further tests and optimization on the fitting code should also be pursued to minimize the source of errors in the determination of morphological quantities.

There is also another topic that could be the focus of future projects: to test the detection of ICRF2+ host galaxies, for which the main task is to extend the Gaia simulations to the ICRF2+ sample whenever the decomposition of the source with an extended profile is possible. This would be done to assess the detectability of the host galaxy by Gaia, and to inspect on how it may affect the determination of the light centroid in order to provide the best alignment possible with the ICRF.

This page intentionally contains only this sentence.

APPENDIX

In this appendix one may find tables with some of the results mentioned throughout the dissertation that did not fit well inside the text.

Name	RA	DEC	HST filter	SDSS image
ICRF J014125.8-092843	25.357634	-9.478798	F702W	Yes
ICRF J053850.3-440508	84.70984	-44.085816	F702W	-
ICRF J072153.4+712036	110.472702	71.343434	F702W	-
ICRF J081815.9+422245	124.566665	42.379282	F606W	Yes
ICRF J082550.3+030924	126.459743	3.156811	F702W	Yes
ICRF J085448.8+200630	133.703646	20.108511	F606W	Yes
ICRF J095820.9+322402	149.58729	32.400614	F555W	Yes
ICRF J095847.2+653354	149.696855	65.565227	F702W	-
ICRF J103334.0+071126	158.391768	7.190597	F555W & F814W	Yes
ICRF J104146.7+523328	160.444923	52.557842	F606W	Yes
ICRF J110427.3+381231	166.113808	38.208833	F702W	Yes
ICRF J114701.3-381211	176.755711	-38.203062	F702W	-
ICRF J115019.2+241753	177.580051	24.298288	F702W	Yes
ICRF J141946.5+542314	214.944156	54.387441	F702W	Yes
ICRF J152237.6-273010	230.656983	-27.502996	F702W	-
ICRF J173957.1+473758	264.988038	47.632878	F702W	Yes
ICRF J175132.8+093900	267.886744	9.650202	F702W	-
ICRF J180045.6+782804	270.19035	78.467783	F702W	Yes
ICRF J182407.0+565101	276.029452	56.850414	F606W	-
ICRF J213410.3-015317	323.542957	-1.888122	F702W	Yes
ICRF J215224.8+173437	328.103414	17.577165	F702W	Yes
ICRF J222547.2-045701	336.446914	-4.950386	F702W	Yes
ICRF J225717.3+074312	344.322096	7.720084	F606W	Yes
IERS 0109+200	18.042446	20.339386	F702W	Yes
IERS 1722+119	261.268101	11.870963	F702W	-

Table 7.1. ICRF2+ sources with HST imaging available. (1) Original catalogue name; (2) and (3) Sky coordinates in degrees and J2000 system; (4) Filter closer to the SDSS r-band for which imaging data is available. (5) Whether the source has SDSS image or not.

SDSS name	RA	DEC	r	z	USNO	ROSAT	HST filter
SDSS J083139.79+460800.8	127.9158	46.1336	16.03 ± 0.005	0.131	T	F	-
SDSS J083915.82+285038.8	129.8159	28.8441	14.28 ± 0.005	0.079	T	F	-
SDSS J084112.79+322455.1	130.3033	32.4153	16.92 ± 0.010	0.070	F	F	-
SDSS J084359.13+510524.9	130.9964	51.0903	15.69 ± 0.005	0.126	T	F	-
SDSS J090937.44+192808.2	137.4060	19.4690	13.88 ± 0.005	0.028	T	F	-
SDSS J113359.23+490343.4	173.4968	49.0621	13.13 ± 0.005	0.032	T	F	-
SDSS J114505.02+193622.8	176.2709	19.6063	12.68 ± 0.005	0.022	T	F	F606W
SDSS J121923.21+054929.7	184.8467	5.8249	10.66 ± 0.005	0.007	T	T	F675W
SDSS J124135.94+162033.6	190.3998	16.3427	15.04 ± 0.005	0.070	T	F	-
SDSS J125433.26+185602.1	193.6386	18.9339	16.18 ± 0.005	0.115	T	F	-
SDSS J130619.24+111339.7	196.5802	11.2277	14.93 ± 0.005	0.086	T	F	-
SDSS J131424.67+621945.8	198.6028	62.3294	15.77 ± 0.005	0.131	T	F	-
SDSS J131739.19+411545.5	199.4133	41.2627	14.66 ± 0.005	0.066	T	F	-
SDSS J141028.05+143840.1	212.6169	14.6445	16.68 ± 0.005	0.144	T	T	-
SDSS J141149.43+524900.1	212.9560	52.8167	14.68 ± 0.005	0.076	T	T	-
SDSS J141652.94+104826.7	214.2206	10.8074	12.06 ± 0.005	0.025	T	F	F702W
SDSS J144017.98+055634.0	220.0749	5.9428	14.55 ± 0.005	0.061	T	F	-
SDSS J150330.91+193908.4	225.8788	19.6523	16.59 ± 0.005	0.151	T	F	-
SDSS J150656.41+125048.6	226.7351	12.8468	13.13 ± 0.005	0.022	T	F	-
SDSS J150721.87+101844.9	226.8412	10.3125	15.27 ± 0.005	0.078	F	F	-
SDSS J152122.54+042030.1	230.3439	4.3417	13.94 ± 0.005	0.052	T	F	-
SDSS J153901.66+353046.0	234.7569	35.5128	16.10 ± 0.005	0.078	T	F	-
SDSS J155949.71+080517.6	239.9572	8.0882	17.36 ± 0.010	2.178	T	T	-
SDSS J160246.39+524358.3	240.6933	52.7329	15.70 ± 0.005	0.106	T	F	-
SDSS J160426.51+174431.1	241.1105	17.7420	15.42 ± 0.005	0.041	T	F	-
SDSS J160616.02+181459.8	241.5668	18.2500	13.51 ± 0.005	0.037	T	F	-
SDSS J164726.87+290949.5	251.8620	29.1638	16.10 ± 0.005	0.132	T	T	-
SDSS J170045.23+300812.8	255.1885	30.1369	14.48 ± 0.005	0.034	F	T	F555W & F814W

Table 7.2. Summary table with information for the 28 OPERGs. (1) SDSS identification name; (2) and (3) the coordinates of the objects in degrees and system J2000; (4) r band magnitude from SDSS and respective error; (5) is the redshift of the source as reported in the SDSS database; (6) and (7) are the corresponding detections (T) or non-detections (F) in the Instruments stated in the table header. (8) HST filter (closest to F606W) with available imaging data.

Table 7.3. Table with morphological information for ICRF2+ sources. (1) ID used in this project; (2) Original object name; (3) and (4) Sky coordinates in degrees and J2000 system; (5) Magnitude of the model PSF; (6) Magnitude of the model Sérsic Profile; (7) Effective radius of the model Sérsic Profile in kpc; (8) Sérsic index of the model Sérsic Profile; (9) Axis ratio of the model Sérsic Profile; (10) Reduced chi^2 of the fit.

ASPA ID	Name	RA	DEC	mag_{PSF}	$\text{mag}_{\text{Sérsic}}$	r_e [kpc]	n	b/a	χ^2/ν
001	ICRF J011857.2-214130	19.7386	-21.6917	17.55 ± 0.005	-	-	-	-	1.129
002	ICRF J073019.1-114112	112.5796	-11.6868	19.58 ± 0.040	-	-	-	-	3.852
003	ICRF J151344.8-101200	228.4371	-10.2001	-	17.94 ± 0.005	0.23 ± 0.005	0.28 ± 0.005	0.43 ± 0.005	1.169
004	ICRF J235810.8-102008	359.5453	-10.3357	18.69 ± 0.010	-	-	-	-	1.134
005	ICRF J005041.3-092905	12.6722	-9.4848	15.83 ± 0.005	-	-	-	-	1.952
006	ICRF J014125.8-092843	25.3576	-9.4788	17.19 ± 0.005	-	-	-	-	1.184
007	ICRF J222940.0-083254	337.4170	-8.5485	17.13 ± 0.005	-	-	-	-	1.195
008	ICRF J124604.2-073046	191.5176	-7.5129	19.65 ± 0.010	-	-	-	-	1.202
009	ICRF J222547.2-045701	336.4469	-4.9504	-	17.57 ± 0.170	0.20 ± 41.700	0.36 ± 161.710	0.41 ± 33.670	1.117
010	ICRF J113624.5-033029	174.1024	-3.5082	19.73 ± 0.010	-	-	-	-	1.221
011	ICRF J023945.4-023440	39.9395	-2.5780	20.17 ± 0.020	-	-	-	-	1.147
012	ICRF J135406.8-020603	208.5287	-2.1009	19.31 ± 0.010	-	-	-	-	1.146
013	ICRF J213410.3-015317	323.5430	-1.8881	17.66 ± 0.005	-	-	-	-	1.158
014	ICRF J001611.0-001512	4.0462	-0.2535	-	20.00 ± 0.020	0.30 ± 56.880	0.05 ± 18.140	0.51 ± 1.650	1.131
015	ICRF J074554.0-004417	116.4753	-0.7382	17.09 ± 0.005	-	-	-	-	1.453
016	ICRF J155751.4-000150	239.4643	-0.0307	-	20.00 ± 117.220	0.31 ± 128.670	0.25 ± 85.030	0.12 ± 523.220	1.133
019	ICRF J021748.9+014449	34.4540	1.7471	16.23 ± 0.005	-	-	-	-	1.487
020	ICRF J081126.7+014652	122.8613	1.7812	19.26 ± 0.010	-	-	-	-	1.128
021	ICRF J105829.6+013358	164.6234	1.5663	17.87 ± 0.005	-	-	-	-	1.120
022	ICRF J091437.9+024559	138.6580	2.7665	19.41 ± 0.010	-	-	-	-	1.108
023	ICRF J154929.4+023701	237.3727	2.6170	-	17.32 ± 21.480	0.20 ± 63.530	0.08 ± 804.010	0.21 ± 650.860	1.670
024	ICRF J052732.7+033131	81.8863	3.5254	17.91 ± 0.005	17.87 ± 0.005	0.44 ± 0.020	0.05 ± 0.010	0.15 ± 0.005	1.983
025	ICRF J082550.3+030924	126.4597	3.1568	18.35 ± 0.005	-	-	-	-	1.170
026	ICRF J150506.4+032630	226.2770	3.4419	18.69 ± 0.060	19.03 ± 0.150	0.93 ± 0.430	4.15 ± 1.520	0.90 ± 0.060	1.111
027	ICRF J155930.9+030448	239.8790	3.0801	20.03 ± 0.020	-	-	-	-	1.169
028	ICRF J210138.8+034131	315.4118	3.6920	17.76 ± 0.005	-	-	-	-	1.194
029	ICRF J080757.5+043234	121.9897	4.5429	-	18.24 ± 0.005	0.22 ± 0.070	0.59 ± 0.470	0.63 ± 0.050	1.164

Table 7.3. (continued)

ASPA ID	Name	RA	DEC	$\mathrm{mag_{PSF}}$	$\mathrm{mag_{Sérsic}}$	r_e [kpc]	n	b/a	χ^2/ν
030	ICRF J122222.5+041315	185.5940	4.2210	-	16.83 ± 4.430	0.20 ± 33.760	0.38 ± 138.230	0.17 ± 21.190	1.104
031	ICRF J145859.3+041613	224.7473	4.2705	18.58 ± 0.210	18.64 ± 0.500	1.18 ± 1.120	9.37 ± 9.710	0.59 ± 0.050	1.166
032	ICRF J161637.5+045932	244.1565	4.9924	-	19.26 ± 0.090	0.20 ± 0.430	1.03 ± 1.260	0.14 ± 4.280	1.149
033	ICRF J101603.1+051302	154.0131	5.2173	18.96 ± 0.010	-	-	-	-	1.168
034	ICRF J155035.2+052710	237.6470	5.4529	18.32 ± 0.005	-	-	-	-	2.523
035	ICRF J232044.8+051349	350.1869	5.2305	18.53 ± 0.010	-	-	-	-	1.134
036	ICRF J002232.4+060804	5.6352	6.1345	18.55 ± 0.005	-	-	-	-	1.154
037	ICRF J022428.4+065923	36.1185	6.9898	19.14 ± 0.010	-	-	-	-	1.157
038	ICRF J104455.9+065538	161.2330	6.9273	19.05 ± 0.010	-	-	-	-	1.150
040	ICRF J123924.5+073017	189.8524	7.5048	18.04 ± 0.005	-	-	-	-	1.212
041	ICRF J225717.3+074312	344.3221	7.7201	16.42 ± 0.005	16.18 ± 0.150	14.23 ± 11.550	9.50 ± 1.140	0.92 ± 0.010	1.125
042	ICRF J065917.9+081330	104.8250	8.2253	17.88 ± 0.005	-	-	-	-	1.405
043	ICRF J001031.0+105829	2.6292	10.9749	-	15.66 ± 0.010	0.60 ± 0.180	10.02 ± 0.320	0.51 ± 0.140	1.676
044	ICRF J150424.9+102939	226.1041	10.4942	18.25 ± 0.005	-	-	-	-	1.152
045	ICRF J160846.2+102907	242.1925	10.4855	18.10 ± 0.005	-	-	-	-	1.180
046	ICRF J012141.5+114950	20.4233	11.8307	19.28 ± 0.010	-	-	-	-	1.118
047	ICRF J044907.6+112128	72.2820	11.3579	19.99 ± 0.010	-	-	-	-	1.172
048	ICRF J125438.2+114105	193.6594	11.6850	16.75 ± 0.005	-	-	-	-	1.190
049	ICRF J075052.0+123104	117.7169	12.5180	17.33 ± 0.005	-	-	-	-	1.239
051	ICRF J034506.4+145349	56.2767	14.8971	20.87 ± 0.030	-	-	-	-	1.679
052	ICRF J072516.8+142513	111.3200	14.4205	-	18.11 ± 0.005	0.20 ± 0.005	0.05 ± 0.005	0.19 ± 0.005	1.192
053	ICRF J111358.6+144226	168.4946	14.7075	17.59 ± 0.005	-	-	-	-	1.147
054	ICRF J142549.0+142456	216.4542	14.4158	17.92 ± 0.005	-	-	-	-	1.113
055	ICRF J174535.2+172001	266.3967	17.3337	20.42 ± 0.020	-	-	-	-	1.385
056	ICRF J215224.8+173437	328.1034	17.5772	19.03 ± 0.010	-	-	-	-	1.127
057	ICRF J080248.0+180949	120.7001	18.1637	20.68 ± 0.020	-	-	-	-	1.188
058	ICRF J102444.8+191220	156.1867	19.2057	18.51 ± 0.110	19.02 ± 0.240	0.20 ± 0.330	6.73 ± 4.560	0.35 ± 0.060	1.160
059	ICRF J143439.7+195200	218.6658	19.8669	-	19.71 ± 0.010	0.33 ± 0.040	0.72 ± 0.370	0.65 ± 0.070	1.081
060	ICRF J151656.7+193212	229.2366	19.5369	18.38 ± 0.005	-	-	-	-	1.130

Table 7.3. (continued)

ASPA ID	Name	RA	DEC	mag_{PSF}	$\text{mag}_{\text{Sérsic}}$	r_e [kpc]	n	b/a	χ^2/ν
061	ICRF J225307.3+194234	343.2807	19.7096	16.46 ± 0.005	-	-	-	-	1.278
062	ICRF J085448.8+200630	133.7036	20.1085	15.47 ± 0.005	-	-	-	-	2.162
063	ICRF J105148.7+211952	162.9533	21.3312	18.39 ± 0.005	-	-	-	-	1.102
064	ICRF J011205.8+224438	18.0243	22.7441	14.77 ± 0.005	-	-	-	-	7.937
065	ICRF J132700.8+221050	201.7536	22.1806	-	18.67 ± 0.005	0.20 ± 0.170	0.92 ± 1.180	0.19 ± 0.070	1.220
066	ICRF J161914.8+224747	244.8118	22.7966	20.04 ± 0.010	-	-	-	-	1.146
067	ICRF J164125.2+225704	250.3551	22.9511	18.95 ± 0.010	-	-	-	-	1.228
069	ICRF J101447.0+230116	153.6961	23.0213	-	17.51 ± 0.870	0.20 ± 11.730	0.05 ± 13.600	0.62 ± 1640.480	1.238
070	ICRF J221205.9+235540	333.0249	23.9279	-	19.61 ± 0.140	0.20 ± 147.750	0.05 ± 63.390	0.74 ± 119.090	1.111
071	ICRF J074836.1+240024	117.1505	24.0067	18.60 ± 0.005	-	-	-	-	1.143
072	ICRF J083052.0+241059	127.7170	24.1833	17.12 ± 0.005	-	-	-	-	1.215
073	ICRF J115019.2+241753	177.5800	24.2983	16.14 ± 0.005	-	-	-	-	2.024
074	ICRF J074625.8+254902	116.6078	25.8173	19.58 ± 0.010	-	-	-	-	2.401
075	ICRF J112553.7+261019	171.4738	26.1722	18.28 ± 0.005	-	-	-	-	1.153
076	ICRF J023752.4+284808	39.4684	28.8025	18.07 ± 0.005	-	-	-	-	1.152
077	ICRF J115931.8+291443	179.8826	29.2455	18.13 ± 0.005	-	-	-	-	1.165
078	ICRF J121752.0+300700	184.4670	30.1168	15.34 ± 0.005	-	-	-	-	6.485
079	ICRF J013708.7+312235	24.2864	31.3766	21.24 ± 0.060	-	-	-	-	1.117
080	ICRF J020504.9+321230	31.2705	32.2084	17.92 ± 0.005	-	-	-	-	2.460
081	ICRF J095820.9+322402	149.5873	32.4006	-	16.00 ± 0.005	0.20 ± 0.005	0.16 ± 0.005	0.19 ± 0.005	1.686
082	ICRF J131059.4+323334	197.7475	32.5596	18.81 ± 0.005	-	-	-	-	1.144
083	ICRF J095232.0+351252	148.1334	35.2146	19.44 ± 0.010	-	-	-	-	1.100
084	ICRF J101810.9+354239	154.5458	35.7110	-	17.93 ± 0.005	0.20 ± 0.005	0.33 ± 0.005	0.38 ± 0.005	1.181
085	ICRF J081525.9+363515	123.8581	36.5875	18.55 ± 0.005	-	-	-	-	1.163
086	ICRF J122847.4+370612	187.1976	37.1034	18.19 ± 0.005	-	-	-	-	1.178
087	ICRF J124251.3+375100	190.7140	37.8500	18.36 ± 0.005	-	-	-	-	1.194
089	ICRF J031049.8+381453	47.7078	38.2483	18.43 ± 0.005	-	-	-	-	1.168
092	ICRF J113053.2+381518	172.7220	38.2551	18.78 ± 0.010	-	-	-	-	1.110
093	ICRF J141946.6+382148	214.9442	38.3635	19.34 ± 0.010	-	-	-	-	1.162

Table 7.3. (continued)

ASPA ID	Name	RA	DEC	$\mathrm{mag_{PSF}}$	$\mathrm{mag_{Sérsic}}$	r_e [kpc]	n	b/a	χ^2/ν
094	ICRF J180024.7+384830	270.1032	38.8085	-	17.55 ± 0.005	0.21 ± 1.860	0.27 ± 7.880	0.62 ± 1.950	1.120
095	ICRF J114658.2+395834	176.7429	39.9762	18.36 ± 0.005	-	-	-	-	1.247
096	ICRF J164029.6+394646	250.1235	39.7794	19.55 ± 0.010	-	-	-	-	1.123
097	ICRF J080856.6+405244	122.2361	40.8791	18.99 ± 0.010	-	-	-	-	1.117
098	ICRF J003824.8+413706	9.6035	41.6183	20.35 ± 0.020	-	-	-	-	1.313
099	ICRF J031301.9+412001	48.2582	41.3337	-	16.54 ± 0.020	3.08 ± 0.440	8.62 ± 0.260	0.67 ± 0.010	1.119
100	ICRF J103303.7+411606	158.2655	41.2684	19.16 ± 0.010	-	-	-	-	1.126
101	ICRF J081815.9+422245	124.5667	42.3793	18.11 ± 0.005	-	-	-	-	1.570
102	ICRF J152149.6+433639	230.4567	43.6109	-	18.90 ± 3.010	0.22 ± 20.100	0.46 ± 98.110	0.14 ± 10.880	1.142
103	ICRF J064632.0+445116	101.6334	44.8546	18.64 ± 0.010	-	-	-	-	1.119
105	ICRF J172727.6+453039	261.8652	45.5110	18.59 ± 0.005	-	-	-	-	1.214
106	ICRF J013658.5+475129	24.2442	47.8581	18.19 ± 0.005	-	-	-	-	2.743
107	ICRF J095819.6+472507	149.5820	47.4188	18.56 ± 0.005	-	-	-	-	1.150
108	ICRF J150048.6+475115	225.2027	47.8543	20.10 ± 0.020	-	-	-	-	1.140
109	ICRF J173957.1+473758	264.9880	47.6329	18.70 ± 0.010	-	-	-	-	1.103
111	ICRF J080839.6+495036	122.1653	49.8435	18.62 ± 0.010	-	-	-	-	1.236
112	ICRF J173927.3+495503	264.8641	49.9176	18.16 ± 0.005	-	-	-	-	1.130
113	ICRF J104146.7+523328	160.4449	52.5578	16.70 ± 0.005	-	-	-	-	1.237
114	ICRF J141946.5+542314	214.9442	54.3874	15.58 ± 0.005	16.55 ± 0.010	3.67 ± 0.140	1.99 ± 0.040	0.72 ± 0.010	1.224
115	ICRF J130252.4+574837	195.7186	57.8105	19.46 ± 0.010	-	-	-	-	1.120
116	ICRF J151002.9+570243	227.5122	57.0454	20.31 ± 0.020	-	-	-	-	1.103
117	ICRF J101725.8+611627	154.3579	61.2743	18.11 ± 0.005	-	-	-	-	1.112
118	ICRF J174614.0+622654	266.5585	62.4485	-	18.99 ± 0.010	0.20 ± 0.190	1.49 ± 1.530	0.44 ± 0.160	1.144
119	ICRF J134345.9+660225	205.9415	66.0405	19.73 ± 0.010	-	-	-	-	1.234
120	ICRF J134408.6+660611	206.0362	66.1032	20.18 ± 0.020	-	-	-	-	1.137
121	ICRF J223036.4+694628	337.6519	69.7745	-	20.34 ± 0.030	0.20 ± 0.320	1.61 ± 2.940	0.16 ± 0.690	1.887
122	ICRF J180045.6+782804	270.1903	78.4678	17.16 ± 0.005	-	-	-	-	1.148
123	ICRF J104423.0+805439	161.0961	80.9110	18.01 ± 0.005	-	-	-	-	1.280
124	IERS 0003+123	1.5960	12.5981	16.57 ± 0.005	-	-	-	-	1.222

Table 7.3. (continued)

ASPA ID	Name	RA	DEC	mag_{PSF}	$\text{mag}_{\text{Sérsic}}$	r_e [kpc]	n	b/a	χ^2/ν
125	IERS 0049+003	13.0232	0.5939	-	16.16 ± 0.005	1.06 ± 0.1	0.05 ± 0.005	0.68 ± 0.005	1.140
126	IERS 0107-025	17.5548	-2.3313	17.57 ± 0.005	-	-	-	-	1.184
127	IERS 0109+200	18.0424	20.3394	17.25 ± 0.005	-	-	-	-	1.366
128	IERS 0130-083	23.1714	-8.0680	18.53 ± 0.010	15.46 ± 0.080	11.40 ± 3.130	4.24 ± 0.230	0.84 ± 0.010	0.783
129	IERS 0145+210	26.9743	21.2610	17.58 ± 0.005	-	-	-	-	1.131
130	IERS 0150+015	28.1650	1.7881	17.25 ± 0.010	14.55 ± 0.020	9.76 ± 1.030	6.02 ± 0.120	0.84 ± 0.005	0.742
131	IERS 0741+294	116.2140	29.3350	16.75 ± 0.005	-	-	-	-	2.413
132	IERS 0751+306	118.7035	30.5653	17.43 ± 0.005	-	-	-	-	1.158
133	IERS 0757+477	120.3832	47.6044	16.26 ± 0.005	16.95 ± 0.020	3.50 ± 0.160	1.71 ± 0.050	0.68 ± 0.010	1.119
135	IERS 0807+083	122.6723	8.1667	19.69 ± 0.010	-	-	-	-	1.167
136	IERS 0818+312	125.2817	31.1309	17.09 ± 0.005	-	-	-	-	1.187
137	IERS 0821+411	126.1625	40.9521	17.20 ± 0.010	19.12 ± 0.060	1.04 ± 0.180	2.13 ± 0.450	0.21 ± 0.020	1.181
138	IERS 0838+235	130.4752	23.3319	17.52 ± 0.005	-	-	-	-	1.136
139	IERS 0838+456	130.5640	45.4289	17.30 ± 0.005	-	-	-	-	1.184
140	IERS 0850+284	133.3243	28.2306	18.07 ± 0.005	-	-	-	-	1.303
141	IERS 0854+334	134.3623	33.2214	-	18.16 ± 0.010	0.20 ± 0.020	5.40 ± 0.600	0.12 ± 0.040	1.252
144	IERS 0950+326	148.3665	32.4310	17.38 ± 0.005	-	-	-	-	1.176
145	IERS 0952+338	148.9080	33.5844	17.39 ± 0.005	-	-	-	-	1.108
146	IERS 1009+334	153.0477	33.1573	17.99 ± 0.005	-	-	-	-	1.188
147	IERS 1009+067	153.0556	6.5159	17.35 ± 0.005	-	-	-	-	1.193
148	IERS 1010+356	153.2595	35.4349	17.94 ± 0.005	-	-	-	-	1.140
149	IERS 1020+292	155.8502	28.9475	20.87 ± 0.040	-	-	-	-	1.144
150	IERS 1028+313	157.7462	31.0488	16.94 ± 0.010	16.22 ± 0.130	9.73 ± 5.520	5.68 ± 0.640	0.97 ± 0.010	0.990
151	IERS 1032+354	158.7957	35.1721	18.07 ± 0.005	-	-	-	-	1.170
152	IERS 1034+574	159.4346	57.1987	16.46 ± 0.005	-	-	-	-	1.228
153	IERS 1101+077	166.1003	7.5148	17.09 ± 0.005	-	-	-	-	1.189
154	IERS 1126+237	172.2154	23.4381	-	18.32 ± 0.280	0.21 ± 40.680	0.35 ± 159.770	0.19 ± 14.130	1.123
155	IERS 1127+078	172.5724	7.5369	-	17.29 ± 0.005	0.20 ± 0.005	0.44 ± 0.005	0.34 ± 0.005	1.118
156	IERS 1128+517	172.8562	51.4826	17.57 ± 0.005	-	-	-	-	1.275

Table 7.3. (continued)

ASPA ID	Name	RA	DEC	mag_{PSF}	$\text{mag}_{\text{Sérsic}}$	r_e [kpc]	n	b/a	χ^2/ν
157	IERS 1140+190	175.7751	18.7286	-	16.87 ± 1.910	0.20 ± 15.740	0.47 ± 70.550	0.15 ± 8.960	1.266
158	IERS 1141+235	175.9079	23.2507	17.81 ± 0.005	-	-	-	-	1.378
159	IERS 1145+321	177.0787	31.9028	17.37 ± 0.005	-	-	-	-	1.186
160	IERS 1148+592	177.8527	58.9882	16.38 ± 0.010	17.38 ± 0.030	0.67 ± 0.060	1.49 ± 0.130	0.59 ± 0.010	1.284
161	IERS 1201+454	180.8975	45.1804	17.47 ± 0.005	-	-	-	-	1.153
162	IERS 1212+467	183.7914	46.4542	-	17.45 ± 0.005	0.20 ± 2.010	0.21 ± 6.070	0.71 ± 3.450	1.181
163	IERS 1228+077	187.8357	7.4313	18.15 ± 0.005	-	-	-	-	1.248
164	IERS 1240+367	190.8030	36.4622	15.95 ± 0.005	-	-	-	-	2.474
165	IERS 1242+574	191.2917	57.1651	17.14 ± 0.005	-	-	-	-	1.591
166	IERS 1307+433	197.3563	43.0849	-	16.99 ± 0.005	0.20 ± 1.750	0.21 ± 5.300	0.69 ± 2.940	1.141
167	IERS 1310+484	198.0464	48.1570	17.23 ± 0.005	-	-	-	-	1.168
168	IERS 1310+314	198.2033	31.2168	17.94 ± 0.005	-	-	-	-	1.118
169	IERS 1312+240	198.6825	23.8074	16.87 ± 0.005	-	-	-	-	1.254
170	IERS 1319+006	200.4148	0.3993	-	17.65 ± 0.250	0.20 ± 38.850	0.22 ± 116.850	0.34 ± 32.770	1.166
171	IERS 1338+303	205.1749	30.1430	20.65 ± 0.030	-	-	-	-	1.155
172	IERS 1340+289	205.7507	28.7354	-	17.03 ± 5.800	0.20 ± 6.900	0.11 ± 15.250	0.44 ± 11.370	1.213
173	IERS 1420+044	215.6770	4.2442	17.26 ± 0.005	-	-	-	-	1.142
174	IERS 1429+249	217.8578	24.7057	17.87 ± 0.110	18.28 ± 0.170	0.47 ± 0.270	7.76 ± 2.680	0.56 ± 0.030	1.270
175	IERS 1518+162	230.1544	16.0241	17.59 ± 0.005	-	-	-	-	1.184
176	IERS 1522+669	230.7455	66.7519	18.77 ± 0.010	-	-	-	-	1.158
177	IERS 1535+231	234.3104	23.0112	19.05 ± 0.010	-	-	-	-	1.185
178	IERS 1556+335	239.7299	33.3885	17.23 ± 0.005	-	-	-	-	1.257
179	IERS 1607+604	242.0856	60.3078	17.32 ± 0.010	17.47 ± 0.030	2.35 ± 0.140	2.63 ± 0.160	0.80 ± 0.010	1.044
180	IERS 1607+183	242.5220	18.1954	18.29 ± 0.005	-	-	-	-	1.137
181	IERS 1612+378	243.6956	37.7687	16.75 ± 0.005	-	-	-	-	1.201
182	IERS 1618+530	244.9266	52.9371	16.75 ± 0.005	-	-	-	-	1.884
183	IERS 1648+417	252.5228	41.6757	17.76 ± 0.005	-	-	-	-	1.132
184	IERS 1653+198	253.9315	19.8131	19.82 ± 0.010	-	-	-	-	1.202
185	IERS 1714+231	259.2236	23.0981	17.69 ± 0.005	-	-	-	-	1.208

Table 7.3. (continued)

ASPA ID	Name	RA	DEC	$\mathrm{mag_{PSF}}$	$\mathrm{mag_{Sérsic}}$	r_e [kpc]	n	b/a	χ^2/ν
187	IERS 1721+343	260.8366	34.2994	15.67 ± 0.005	-	-	-	-	2.765
188	IERS 1729+372	262.6960	37.2486	18.32 ± 0.020	17.79 ± 0.030	2.75 ± 0.200	2.05 ± 0.140	0.80 ± 0.020	1.059
189	IERS 1730+604	262.7196	60.4213	17.65 ± 0.005	-	-	-	-	1.101
190	IERS 1741+597	265.6333	59.7519	17.05 ± 0.005	-	-	-	-	1.312
192	IERS 2043+749	310.6555	75.1340	14.49 ± 0.005	16.27 ± 0.050	11.78 ± 1.590	4.00 ± 0.005	0.62 ± 0.020	2.727
194	IERS 2057+235	315.0201	23.7843	19.12 ± 0.010	-	-	-	-	1.281
195	IERS 2116+203	319.6447	20.5672	17.78 ± 0.005	-	-	-	-	1.273
196	IERS 2241+200	340.9781	20.3511	-	15.78 ± 0.005	0.20 ± 0.005	0.29 ± 0.010	0.21 ± 0.005	27.271
197	IERS 2314+160	349.1654	16.3019	-	17.10 ± 0.190	0.20 ± 47.650	0.23 ± 151.980	0.52 ± 53.690	1.237
198	IERS 2316+238	349.6415	24.0777	19.02 ± 0.005	-	-	-	-	1.130

Table 7.4. Table with morphological information for OPERGs. (1) ID used in this project; (2) Original object name; (3) and (4) Sky coordinates in degrees and J2000 system; (5) Magnitude of the model Sérsic Profile; (6) Effective radius of the model Sérsic Profile in pixel units (in the case where a Gaussian was used, the value corresponds to the FWHM of the model); (7) Sérsic index of the model Sérsic Profile; (8) Axis ratio of the model Sérsic Profile; (9) Reduced chi^2 of the fit.

ASPA ID	Name	RA	DEC	$\mathrm{mag_{Sérsic}}$	r_e [pix]	n	b/a	χ^2/ν
1	SDSS J083139.79+460800.8	127.9158	46.1336	15.539 ± 0.015	26.031 ± 0.771	6.899 ± 0.083	0.653 ± 0.004	1.114
2	SDSS J083915.82+285038.8	129.8159	28.8441	14.259 ± 0.003	22.146 ± 0.104	3.818 ± 0.010	0.822 ± 0.002	1.251
3	SDSS J084112.79+322455.1	130.3033	32.4153	17.381 ± 0.014	2.229 ± 0.053	4.420 ± 0.212	0.446 ± 0.009	1.175
4	SDSS J084359.13+510524.9	130.9964	51.0903	14.852 ± 0.039	72.514 ± 6.103	9.047 ± 0.243	0.690 ± 0.005	1.142
5	SDSS J090937.44+192808.2	137.4060	19.4690	13.916 ± 0.009	25.404 ± 0.225	2.718 ± 0.028	0.827 ± 0.001	1.164
""	""	""	""	15.735 ± 0.048	2.908 ± 0.125	3.314 ± 0.060	0.702 ± 0.003	-
6	SDSS J113359.23+490343.4	173.4968	49.0621	12.627 ± 0.019	80.106 ± 1.746	4.172 ± 0.101	0.830 ± 0.001	0.736
""	""	""	""	15.002 ± 0.029	5.890 ± 0.074	2.854 ± 0.019	0.588 ± 0.004	-
7	SDSS J114505.02+193622.8	176.2709	19.6063	12.075 ± 0.030	122.369 ± 4.087	2.945 ± 0.090	0.904 ± 0.001	0.516
""	""	""	""	13.949 ± 0.011	6.922 ± 0.019	1.686 ± 0.004	0.953 ± 0.001	-
8	SDSS J121923.21+054929.7	184.8467	5.8249	10.524 ± 0.002	61.133 ± 0.087	2.021 ± 0.005	0.784 ± 0.000	0.180
""	""	""	""	13.360 ± 0.004	7.811 ± 0.007	0.719 ± 0.002	0.694 ± 0.000	-
9	SDSS J124135.94+162033.6	190.3998	16.3427	14.236 ± 0.011	41.207 ± 0.946	8.685 ± 0.064	0.754 ± 0.002	1.194
10	SDSS J125433.26+185602.1	193.6386	18.9339	15.709 ± 0.027	29.858 ± 1.605	6.783 ± 0.143	0.727 ± 0.006	1.258
11	SDSS J130619.24+111339.7	196.5802	11.2277	14.918 ± 0.006	17.746 ± 0.197	4.529 ± 0.028	0.757 ± 0.002	1.153
12	SDSS J131424.67+621945.8	198.6028	62.3294	15.180 ± 0.018	32.769 ± 1.153	6.846 ± 0.091	0.819 ± 0.004	1.125
13	SDSS J131739.19+411545.5	199.4133	41.2627	15.877 ± 0.043	15.066 ± 0.090	1.551 ± 0.024	0.290 ± 0.005	1.132
""	""	""	""	14.825 ± 0.010	27.905 ± 1.441	5.306 ± 0.168	0.784 ± 0.010	-
14	SDSS J141028.05+143840.1	212.6169	14.6445	15.533 ± 0.077	92.043 ± 19.526	16.151 ± 0.814	0.779 ± 0.009	1.184
15	SDSS J141149.43+524900.1	212.9560	52.8167	14.954 ± 0.142	30.603 ± 0.481	2.966 ± 0.150	0.801 ± 0.026	1.102
""	""	""	""	15.345 ± 0.221	9.353 ± 2.795	7.276 ± 0.469	0.771 ± 0.010	-
16	SDSS J141652.94+104826.7	214.2206	10.8074	11.810 ± 0.009	65.058 ± 0.302	2.334 ± 0.031	0.835 ± 0.001	1.102
""	""	""	""	13.820 ± 0.016	9.066 ± 0.023	1.470 ± 0.005	0.670 ± 0.002	-
17	SDSS J144017.98+055634.0	220.0749	5.9428	14.070 ± 0.005	28.845 ± 0.277	6.724 ± 0.024	0.915 ± 0.002	1.054
18	SDSS J150330.91+193908.4	225.8788	19.6523	16.161 ± 0.016	13.373 ± 0.451	7.191 ± 0.109	0.979 ± 0.007	1.176
19	SDSS J150656.41+125048.6	226.7351	12.8468	13.605 ± 0.005	50.884 ± 0.210	0.762 ± 0.006	0.609 ± 0.001	1.354

Table 7.4. (continued)

ASPA ID	Name	RA	DEC	$\mathrm{mag}_{\mathrm{Sérsic}}$	r_e [pix]	n	b/a	χ^2/ν
""	""	""	""	14.093 ± 0.008	9.718 ± 0.063	1.600 ± 0.006	0.732 ± 0.001	-
20	SDSS J150721.87+101844.9	226.8412	10.3125	14.663 ± 0.018	19.776 ± 0.693	5.736 ± 0.094	0.730 ± 0.006	13.066
21	SDSS J152122.54+042030.1	230.3439	4.3417	13.723 ± 0.016	50.632 ± 0.554	2.480 ± 0.053	0.905 ± 0.002	0.990
""	""	""	""	15.905 ± 0.038	4.896 ± 0.118	2.547 ± 0.024	0.809 ± 0.004	-
22	SDSS J153901.66+353046.0	234.7569	35.5128	15.946 ± 0.007	7.370 ± 0.096	4.160 ± 0.037	0.922 ± 0.004	1.221
23	SDSS J155949.71+080517.6	239.9572	8.0882	17.482 ± 0.002	–	–	–	1.292
24	SDSS J160246.39+524358.3	240.6933	52.7329	15.322 ± 0.055	22.668 ± 2.135	4.096 ± 0.216	0.919 ± 0.022	32.772
""	""	""	""	17.971 ± 0.083	6.989 ± 0.511	–	0.401 ± 0.036	-
25	SDSS J160426.51+174431.1	241.1105	17.7420	14.301 ± 0.021	54.176 ± 0.654	1.308 ± 0.035	0.900 ± 0.004	1.277
""	""	""	""	14.696 ± 0.017	7.149 ± 0.132	2.983 ± 0.025	0.952 ± 0.001	-
26	SDSS J160616.02+181459.8	241.5668	18.2500	13.557 ± 0.003	17.754 ± 0.083	4.139 ± 0.010	0.953 ± 0.001	2.049
27	SDSS J164726.87+290949.5	251.8620	29.1638	15.768 ± 0.019	20.425 ± 0.592	4.785 ± 0.130	0.641 ± 0.004	1.207
""	""	""	""	18.461 ± 0.043	0.946 ± 0.037	–	0.161 ± 0.308	-
28	SDSS J170045.23+300812.8	255.1885	30.1369	14.017 ± 0.003	15.385 ± 0.080	5.398 ± 0.014	0.853 ± 0.001	1.116

SDSS name	RA	DEC	Δ ["]
SDSSJ083139.79+460800.8	127.91564	46.13355	-
SDSSJ083915.82+285038.8	129.81595	28.84412	-
SDSSJ084112.79+322455.1	130.28600	32.41739	-
SDSSJ084359.13+510524.9	130.99641	51.09026	-
SDSSJ090937.44+192808.2	137.40598	19.46900	0.3400
SDSSJ113359.23+490343.4	173.49687	49.06199	0.0455
SDSSJ114505.02+193622.8	176.27083	19.60633	0.3670
SDSSJ121923.21+054929.7	184.84674	5.82490	0.0445
SDSSJ124135.94+162033.6	190.41088	16.33258	-
SDSSJ125433.26+185602.1	193.63861	18.93393	-
SDSSJ130619.24+111339.7	196.58020	11.22772	-
SDSSJ131424.67+621945.8	198.60277	62.32942	-
SDSSJ131739.19+411545.5	199.41337	41.26261	0.3535
SDSSJ141028.05+143840.1	212.61692	14.64444	-
SDSSJ141149.43+524900.1	212.94594	52.83076	0.0735
SDSSJ141652.94+104826.7	214.22066	10.80738	0.0228
SDSSJ144017.98+055634.0	220.07255	5.94688	-
SDSSJ150330.91+193908.4	225.87839	19.65306	-
SDSSJ150656.41+125048.6	226.73504	12.84681	0.5748
SDSSJ150721.87+101844.9	226.85268	10.29689	-
SDSSJ152122.54+042030.1	230.35447	4.33004	0.1137
SDSSJ153901.66+353046.0	234.75693	35.51273	-
SDSSJ155949.71+080517.6	239.95710	8.08830	-
SDSSJ160246.39+524358.3	240.69616	52.75735	0.2869
SDSSJ160426.51+174431.1	241.11048	17.74189	0.7231
SDSSJ160616.02+181459.8	241.56681	18.24989	-
SDSSJ164726.87+290949.5	251.86075	29.14357	0.0404
SDSSJ170045.23+300812.8	255.18847	30.13699	-

Table 7.5. Centroid position of optical light distribution the OPERGs. Whenever two components are necessary the displacement between the two centroids is displayed in the last column.

ACKNOWLEDGEMENTS

This dissertation would not have been possible to write without the acceptance and supervision of Doctor Sonia Antón Castillo and Professor António Joaquim Rosa Amorim Barbosa. I would like to thank them for everything, but especially for giving me the opportunity to do research at SIM-FCUL.

The project PTDC/CTE-SPA/118692/2010 was the basis for my financial support so, I would give an acknowledgement to Fundação para a Ciência e Tecnologia (FCT).

Funding for SDSS-III has been provided by the Alfred P. Sloan Foundation, the Participating Institutions, the National Science Foundation, and the U.S. Department of Energy Office of Science. The SDSS-III web site is `http://www.sdss3.org/`.

SDSS-III is managed by the Astrophysical Research Consortium for the Participating Institutions of the SDSS-III Collaboration including the University of Arizona, the Brazilian Participation Group, Brookhaven National Laboratory, Carnegie Mellon University, University of Florida, the French Participation Group, the German Participation Group, Harvard University, the Instituto de Astrofisica de Canarias, the Michigan State/Notre Dame/JINA Participation Group, Johns Hopkins University, Lawrence Berkeley National Laboratory, Max Planck Institute for Astrophysics, Max Planck Institute for Extraterrestrial Physics, New Mexico State University, New York University, Ohio State University, Pennsylvania State University, University of Portsmouth, Princeton University, the Spanish Participation Group, University of Tokyo, University of Utah, Vanderbilt University, University of Virginia, University of Washington, and Yale University.

This dissertation also makes use of data products based on observations made with the NASA/ESA Hubble Space Telescope, obtained from the Hubble Legacy Archive, which is a collaboration between the Space Telescope Science Institute (STScI/NASA), the Space Telescope European Coordinating Facility (ST-ECF/ESA) and the Canadian Astronomy Data Centre (CADC/NRC/CSA).

In order to improve my knowledge, this research has made use of NASA's Astrophysics Data System Bibliographic Services and the NASA/IPAC Extragalactic Database (NED) which is operated by the Jet Propulsion Laboratory, California Institute of Technology, under contract with the National Aeronautics and Space Administration.

I acknowledge with thanks to Emmanuel Bertin & Stéphane Arnouts for providing to the astronomical community the SExtractor software, and to Chien Peng for making GALFIT publicly available and for the many enlightening discussions. STSDAS is a product of the Space Telescope Science Institute, which is operated by AURA for NASA and I would like to thank all the staff to make public this analysis package. I also thank the French CNES for providing computational resources and the Gaia Data Processing and Analysis Consortium Coordination Unit2 - Simulations for the Gaia Instrument and Basic Image Simulator.

Matplotlib is a 2D graphics package used for Python for application development, interactive scripting, and publication-quality image generation across user interfaces and operating systems. It contributes to the figures displayed in this dissertation and because of that, I would like to acknowledge John Hunter and the active development community.

I am sincerely grateful to Doctor Alberto Krone-Martins and Doctor Mercedes Filho for the interesting discussions, advices and being a wonderful source of support over these last two years.

It is a pleasure to thank the many well-informed Professors who helped me to understand a little bit more about the Universe, since I am greatly indebted to them. An honourable mention goes to my office-mates, especially to Tiago Frederico, for the good working atmosphere that they provide me.

I would like to give a special thanks to Doctor Lidia Tasca for providing me guidance and knowledge without which this dissertation would not have had a "*happy ending*".

Not only for the past two years, but since the very first moment, I appreciate my parents for all that they have done for me. I also appreciate my family, in special my aunt and her husband, and my best friend José Braga (and his parents) for the great efforts done on helping me to finish this dissertation.

More than I can express, I would like to give thanks to my amazing boyfriend Bruno for discuss the work with me on a daily basis and for his encouragement, help, patience and love. Without him I would not be able to admire the struggle it takes simply to be human...

Esposende, September 2014 Ana Paulino-Afonso

BIBLIOGRAPHY

Ahn, C. P. et al. 2012, ApJS, 203, 21, 1207.7137

Andrei, A. H. et al. 2012a, MmSAI, 83, 930

Andrei, A. H. et al. 2012b, in IAU Joint Discussion, Vol. 7, IAU Joint Discussion

Andrew, B. H., & Kraus, J. D. 1970, ApJL, 159, L45

Annis, J. et al. 2011, ArXiv e-prints, 1111.6619

Antón, S., & Browne, I. W. A. 2005, MNRAS, 356, 225, astro-ph/0409643

Antón, S., Browne, I. W. A., & Marchã, M. J. 2008, A&A, 490, 583, 0907.2400

Antón, S., Browne, I. W. A., Marchã, M. J. M., Bondi, M., & Polatidis, A. 2004, MNRAS, 352, 673

Antonucci, R. 1993, ARA&A, 31, 473

Arago, F. 1854, Astronomie Populaire, ouvre posthume edn. (Paris : Gide et J. Boudry)

Babusiaux, C. 2005, in ESA Special Publication, Vol. 576, The Three-Dimensional Universe with Gaia, ed. C. Turon, K. S. O'Flaherty, & M. A. C. Perryman, 417

Babusiaux, C., Sartoretti, P., Leclerc, N., & Chéreau, F. 2011, GIBIS: Gaia Instrument and Basic Image Simulator, 1107.002, astrophysics Source Code Library

Bahcall, J. N., Kirhakos, S., Saxe, D. H., & Schneider, D. P. 1997, ApJ, 479, 642, astro-ph/9611163

Baum, S. A. et al. 1997, ApJ, 483, 178

Beckmann, V., & Shrader, C. 2012, Active Galactic Nuclei, Physics textbook (Wiley)

Bertin, E., & Arnouts, S. 1996, A&AS, 117, 393

Binney, J., May, A., & Ostriker, J. P. 1987, MNRAS, 226, 149

Blanton, M. R. et al. 2001, AJ, 121, 2358, astro-ph/0012085

Bondi, M., Marchã, M. J. M., Polatidis, A., Dallacasa, D., Stanghellini, C., & Antón, S. 2004, MNRAS, 352, 112

Bourda, G., Charlot, P., & Le Campion, J.-F. 2008, A&A, 490, 403, 0809.1369

Bourda, G., Charlot, P., Porcas, R. W., & Garrington, S. T. 2010, A&A, 520, A113

Bourda, G., Collioud, A., Charlot, P., Porcas, R., & Garrington, S. 2011, A&A, 526, A102

Brown, R. H., & Hazard, C. 1959, MNRAS, 119, 297

Busko, I. C. 1996, in Astronomical Society of the Pacific Conference Series, Vol. 101, Astronomical Data Analysis Software and Systems V, ed. G. H. Jacoby & J. Barnes, 139

Capetti, A., de Ruiter, H. R., Fanti, R., Morganti, R., Parma, P., & Ulrich, M.-H. 2000, A&A, 362, 871, astro-ph/0009056

Carroll, B., & Ostlie, D. 2007, An Introduction to Modern Astrophysics (Pearson Addison-Wesley)

Cattaneo, A. et al. 2009, Nature, 460, 213, 0907.1608

Charlot, P., & Bourda, G. 2012, MmSAI, 83, 959

Ciotti, L., & Bertin, G. 1999, A&A, 352, 447, arXiv:astro-ph/9911078

Curtis, H. D. 1920, JRASC, 14, 317

de Souza, R. E., Krone-Martins, A., dos Anjos, S., Ducourant, C., & Teixeira, R. 2014, ArXiv e-prints, 1404.4521

Delgado-Serrano, R., Hammer, F., Yang, Y. B., Puech, M., Flores, H., & Rodrigues, M. 2010, A&A, 509, A78, 0906.2805

Dollet, C., Bijaoui, A., & Mignard, F. 2005, in ESA Special Publication, Vol. 576, The Three-Dimensional Universe with Gaia, ed. C. Turon, K. S. O'Flaherty, & M. A. C. Perryman, 429

Dullo, B. T., & Graham, A. W. 2013, ArXiv e-prints, 1310.5867

Edge, D. O., Shakeshaft, J. R., McAdam, W. B., Baldwin, J. E., & Archer, S. 1959, MmRAS, 68, 37

Elson, R. A. W. 1999, in Globular Clusters, ed. C. Martínez Roger, I. Perez Fournón, & F. Sánchez, 209–248

Fabian, A. C. 2010, in IAU Symposium, Vol. 267, IAU Symposium, ed. B. M. Peterson, R. S. Somerville, & T. Storchi-Bergmann, 341–349, 0912.0880

Falomo, R., Bettoni, D., Karhunen, K., Kotilainen, J. K., & Uslenghi, M. 2014, MNRAS, 440, 476, 1402.4300

Fanaroff, B. L., & Riley, J. M. 1974, MNRAS, 167, 31P

Fey, A., Gordon, D., & Jacobs, C. S. 2009, Verlag des Bundesamts für Kartographie und Geodäsie, IERS Technical Note 35

Fey, A. L. et al. 2004, AJ, 127, 3587

Fukugita, M., Ichikawa, T., Gunn, J. E., Doi, M., Shimasaku, K., & Schneider, D. P. 1996, AJ, 111, 1748

Gebhardt, K. et al. 2000, ApJL, 539, L13, astro-ph/0006289

George, I. M., & Fabian, A. C. 1991, MNRAS, 249, 352

Häring, N., & Rix, H.-W. 2004, ApJL, 604, L89, astro-ph/0402376

Harrison, D. L. 2011, Experimental Astronomy, 31, 157, 1107.0210

Hoyle, F., & Fowler, W. A. 1963, MNRAS, 125, 169

Hubble, E. 1926, Contributions from the Mount Wilson Observatory / Carnegie Institution of Washington, 324, 1

——. 1929, Proceedings of the National Academy of Science, 15, 168

Jedrzejewski, R. I. 1987, MNRAS, 226, 747

Kelvin, L. S. et al. 2012, MNRAS, 421, 1007, 1112.1956

Khachikian, E. Y., & Weedman, D. W. 1974, ApJ, 192, 581

Kim, M., Ho, L. C., Peng, C. Y., Barth, A. J., & Im, M. 2008, ApJS, 179, 283, 0807.1334

Kormendy, J., & Ho, L. C. 2013, ARA&A, 51, 511, 1304.7762

Krist, J. E., Hook, R. N., & Stoehr, F. 2011, in Society of Photo-Optical Instrumentation Engineers (SPIE) Conference Series, Vol. 8127, Society of Photo-Optical Instrumentation Engineers (SPIE) Conference Series

Krolik, J. 1999, Active Galactic Nuclei: From the Central Black Hole to the Galactic Environment, Princeton series in astrophysics (Princeton University Press)

Krone-Martins, A. 2011, PhD thesis

Krone-Martins, A. et al. 2013, A&A, 556, A102, 1307.5732

Lauer, T. R. et al. 1995, AJ, 110, 2622

Ledlow, M. J., & Owen, F. N. 1995, AJ, 109, 853

Lupton, R., Gunn, J. E., Ivezić, Z., Knapp, G. R., & Kent, S. 2001, in Astronomical Society of the Pacific Conference Series, Vol. 238, Astronomical Data Analysis Software and Systems X, ed. F. R. Harnden, Jr., F. A. Primini, & H. E. Payne, 269, astro-ph/0101420

Lupton, R. H., Ivezic, Z., Gunn, J. E., Knapp, G., Strauss, M. A., & Yasuda, N. 2002, in Society of Photo-Optical Instrumentation Engineers (SPIE) Conference Series, Vol. 4836, Survey and Other Telescope Technologies and Discoveries, ed. J. A. Tyson & S. Wolff, 350–356

Lynden-Bell, D. 1969, Nature, 223, 690

Lynden-Bell, D., & Rees, M. J. 1971, MNRAS, 152, 461

Ma, C., Arias, E. F., Eubanks, T. M., Fey, A. L., Gontier, A.-M., Jacobs, C. S., & Sovers, O. J. 1997, in IAU Joint Discussion, Vol. 7, IAU Joint Discussion

Ma, C., & Feissel, M. 1998, VizieR Online Data Catalog, 1251, 0

Maia, M. A. G., Machado, R. S., & Willmer, C. N. A. 2003, AJ, 126, 1750, astro-ph/0307180

Maiolino, R., & Rieke, G. H. 1995, ApJ, 454, 95

McGimsey, B. Q., Smith, A. G., Scott, R. L., Leacock, R. J., Edwards, P. L., Hackney, R. L., & Hackney, K. R. 1975, AJ, 80, 895

Messier, C. 1784, Connossaince des Temps, 227

Mignard, F. 2010, in ADA 6 - Sixth Conference on Astronomical Data Analysis

Mignard, F. 2012, MmSAI, 83, 918

Moffat, A. F. J. 1969, A&A, 3, 455

Montgomery, D., & Runger, G. 2010, Applied Statistics and Probability for Engineers (John Wiley & Sons)

Morishita, T., Ichikawa, T., & Kajisawa, M. 2014, ApJ, 785, 18, 1402.5752

Öpik, E. 1922, ApJ, 55, 406

Orosz, G., & Frey, S. 2013, A&A, 553, A13, 1303.6763

Osterbrock, D., & Ferland, G. 2006, Astrophysics of Gaseous Nebulae and Active Galactic Nuclei (University Science Books)

Peng, C. Y., Ho, L. C., Impey, C. D., & Rix, H.-W. 2002, AJ, 124, 266, arXiv:astro-ph/0204182

——. 2010, AJ, 139, 2097, 0912.0731

Perryman, M. A. C. et al. 2001, A&A, 369, 339, astro-ph/0101235

Peterson, B. 1997, An Introduction to Active Galactic Nuclei (Cambridge University Press)

Pier, J. R., Munn, J. A., Hindsley, R. B., Hennessy, G. S., Kent, S. M., Lupton, R. H., & Ivezić, Ž. 2003, AJ, 125, 1559, astro-ph/0211375

Poggianti, B. M. et al. 2013, in IAU Symposium, Vol. 295, IAU Symposium, ed. D. Thomas, A. Pasquali, & I. Ferreras, 151–154, 1212.3207

Press, W. H., Teukolsky, S. A., Vetterling, W. T., & Flannery, B. P. 1992, Numerical recipes in FORTRAN. The art of scientific computing

Radon, J. 1917, Akad. Wiss., 69, 262

Robin, A. C. et al. 2012, A&A, 543, A100, 1202.0132

Robin, A. C., & Reylé, C. 2011, in SF2A-2011: Proceedings of the Annual meeting of the French Society of Astronomy and Astrophysics, ed. G. Alecian, K. Belkacem, R. Samadi, & D. Valls-Gabaud, 345–348

Robson, I. 1996, Active galactic nuclei, Wiley-Praxis series in astronomy and astrophysics (Wiley)

Salpeter, E. E. 1964, ApJ, 140, 796

Santini, P. et al. 2012, A&A, 540, A109, 1201.4394

Schmidt, M. 1963, Nature, 197, 1040

Schmitt, J. L. 1968, Nature, 218, 663

Sérsic, J. L. 1968, Atlas de galaxias australes

Seyfert, C. K. 1943, ApJ, 97, 28

Slipher, V. M. 1913, Lowell Observatory Bulletin

Smith, K. T., Solmon, D. C., & Wagner, S. L. 1977, Bulletin of the American Mathematical Society, 83, 1227

Sparke, L., & Gallagher, J. 2007, Galaxies in the Universe: An Introduction (Cambridge University Press)

Stringer, M. J., Shankar, F., Novak, G. S., Huertas-Company, M., Combes, F., & Moster, B. P. 2013, ArXiv e-prints, 1310.3823

Taris, F. et al. 2013, A&A, 552, A98

Taylor, G. L., Dunlop, J. S., Hughes, D. H., & Robson, E. I. 1996, MNRAS, 283, 930

Tody, D. 1986, in Society of Photo-Optical Instrumentation Engineers (SPIE) Conference Series, Vol. 627, Instrumentation in astronomy VI, ed. D. L. Crawford, 733

Tody, D. 1993, in Astronomical Society of the Pacific Conference Series, Vol. 52, Astronomical Data Analysis Software and Systems II, ed. R. J. Hanisch, R. J. V. Brissenden, & J. Barnes, 173

Urry, C. M., & Padovani, P. 1995, PASP, 107, 803, astro-ph/9506063

Uslenghi, M., & Falomo, R. 2011, in Society of Photo-Optical Instrumentation Engineers (SPIE) Conference Series, Vol. 8135

Veilleux, S. 2008, NewAR, 52, 289, 0807.3904

Walter, H., & Sovers, O. 2000, Astrometry of Fundamental Catalogues: The Evolution from Optical to Radio Reference Frames, Astronomy and Astrophysics Library (Springer Berlin Heidelberg)

Woltjer, L. 1959, ApJ, 130, 38

Wuyts, S., Cox, T. J., Hayward, C. C., Franx, M., Hernquist, L., Hopkins, P. F., Jonsson, P., & van Dokkum, P. G. 2010, ApJ, 722, 1666, 1008.4127

Yasuda, N. et al. 2001, AJ, 122, 1104, astro-ph/0105545

York, D. G. et al. 2000, AJ, 120, 1579, astro-ph/0006396

Zel'dovich, Y. B., & Novikov, I. D. 1964, Soviet Physics Doklady, 9, 246